Universität Bonn

Physikalisches Institut

Search for Trilepton Events in the ATLAS experiment at the LHC with 2 fb^{-1} at $\sqrt{s} = 7$ TeV

Ralph Schäfer

In order to observe new physics phenomena like Supersymmetry (SUSY), one needs clean decay channels to distinguish them from the background. A promising channel are three isolated leptons in the final state. Therefore a search for trilepton events is performed with 2 fb^{-1} of data at $\sqrt{s} = 7$ TeV provided by the ATLAS experiment.
No specific SUSY model is considered in the analysis, but a phenomenologic model using masses of gluinos and squark to build a two-dimensional grid. No excess in data has been observed and confidence level been set to the grid points. To validate the modelling of fake and secondary leptons in Monte Carlo samples, a data-driven method - the so called matrix method - is used to determine the event yield of processes without three leptons from the hard scattering. Within the uncertainties, the event yields from Monte Carlo and the matrix method agree.

Physikalisches Institut der
Universität Bonn
Nußallee 12
D-53115 Bonn

BONN-IB-2012-04
February 2012

Universität Bonn

Physikalisches Institut

Search for Trilepton Events in the ATLAS experiment at the LHC with 2 fb^{-1} at $\sqrt{s} = 7$ TeV

Ralph Schäfer

Dieser Forschungsbericht wurde als Masterarbeit von der Mathematisch-Naturwissenschaftlichen Fakultät der Universität Bonn angenommen.

Angenommen am:	12.12.2011
Referent:	Prof. Dr. Norbert Wermes
Koreferent:	Prof. Dr. Ian Brock

Contents

Chapter 1

Introduction

Elementary particle physics is a chapter of physics that started with the discovery of the electron more than hunded years ago. It is the first particle that, up to our knowledge today, cannot be divided into another "subparticle" and is therefore elementary. In the 30's of the 20th century there followed the antiparticle of the electron, the so called positron, which shows the same properties of the electron but having the opposite charge and the muon that has exactly the same charge as the electron, but a mass that is roughly 200 times larger than the electron's one. Soon, the number of elementary particles increased and in the case of the spin-$\frac{1}{2}$ particles (leptons) they were arranged in three different families. Unfortunately, it took until the mid 60's to develop a theory that was consistent with the measurements that were made until that time [1]. This theory is called the standard model of elementary particle physics or short SM. It could describe the coupling strengths of the leptons to the gauge bosons like the photon, which are the mediators of the four different forces that can occur between the elementary particles. Furthermore, the SM could predict the existence and masses of the W and Z boson, which are the mediators of the weak force and could be found at the LEP collider in 1983 [2][3]. The last great successes were the discoveries of the top quark in 1995 [4][5] and the tau neutrino in 2000 [6] that were both found at the Fermilab and also predicted by the SM. The only missing piece in the standard model is the Higgs boson that could not be discovered until today (Dec. 2011). This is one of the reasons that the Large Hadron Collider (LHC) has been built at CERN near Geneva. With an intended center of mass energy of 14 TeV it should discover the Higgs boson in the near future according to the predictions made by the SM. But even if it has been found, that's actually not the end of the story. There are many theories beyond the standard model (BSM) that predict new particles or even a unification of the different coupling strengths above a certain energy scale. This is the other field of particle physics which is searched for at the LHC.

Many BSM theories predict final states with three leptons. One of these theories is the so called theory of supersymmetry (SUSY). It provides many decay possibilities to get three leptons. The decay channel with three leptons is also often called golden-plated channel, because it has very few SM contamination when one looks into kintematical regions which are typical for SUSY events. Hence, it has already been studied at the Tevatron in the CDF [7] and the D0 [8] experiments. No excess in data has been observed so far, but it's still one of the promising channels to observe new physics.

This thesis takes the trilepton channel and analyses it in terms of a phenomenological model that targets the typical decay mode, where two gluinos or squarks are produced. The leptons used for the analyses are only electrons and muons and will be referred to as leptons throughout the thesis. The reason for this is, that tau-leptons have a short lifetime and decay before they can reach the detector. The corresponding neutrinos leave the detector without any interaction and are therefore "invisible" to the detector.

An important background to trilepton events are processes with less than three leptons from the hard scattering, but that can end up in the trilepton final state by secondary decays. These processes can usually not be modelled well enough in a detector simulation. Therefore one tries to estimate them from data. This thesis uses the so called matrix method to get a cross check for the contribution of these

processes to the trilepton background. Based on the observed number of events measured from data, limits will be set to the input parameters of the signal model.

Chapter 2

The LHC and the ATLAS Experiment

2.1 The LHC

The Large Hadron Collider is a proton-proton collider which was built in the tunnel of the LEP collider [1] at CERN near Geneva. Its main purpose is to test the standard model at high energies and search for new physics. The protons are injected at an energy of 450 GeV and then accelerated up to an energy of 7 TeV leading to a center of mass energy of 14 TeV [2] for the collision. At the peak luminosity of $1 \times 10^{34} \frac{1}{\text{cm}^2\text{s}}$, 2808 bunches, each of them carrying 1.15×10^{11} protons, circulate in the ring [9]. The bunches collide at four interaction points where the different experiments are located (see fig. 2.1), where due to the high amount of bunches at the peak luminosity, collisions take place at a rate of roughly 40 MHz.

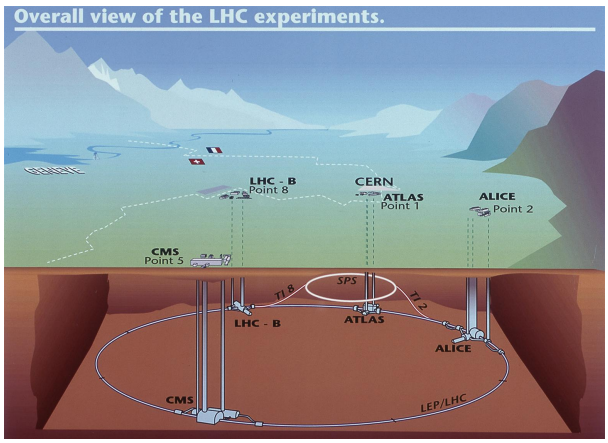

Figure 2.1: The four LHC experiments [10]

2.1.1 The ATLAS detector

ATLAS (**A** **T**oroidal **L**HC **A**pparatu**S**) is one of the four experiments at the LHC (fig. 2.1). With a weight of 7000 tons, a length of 44 m and a diameter of 25 m it is a huge detector, that covers almost 4π of solid angle. The detector consists of three different subparts which are arranged in a cylindrical shape.
The following descriptions are based on and pictures are taken from sources [11], [12] and [13].

[1] 27 km circumference and 100 m under ground on average to reduce influence of cosmic rays to the experiment.
[2] The center of mass energy of the 2011 data, which is analysed in this thesis, is 7 TeV.

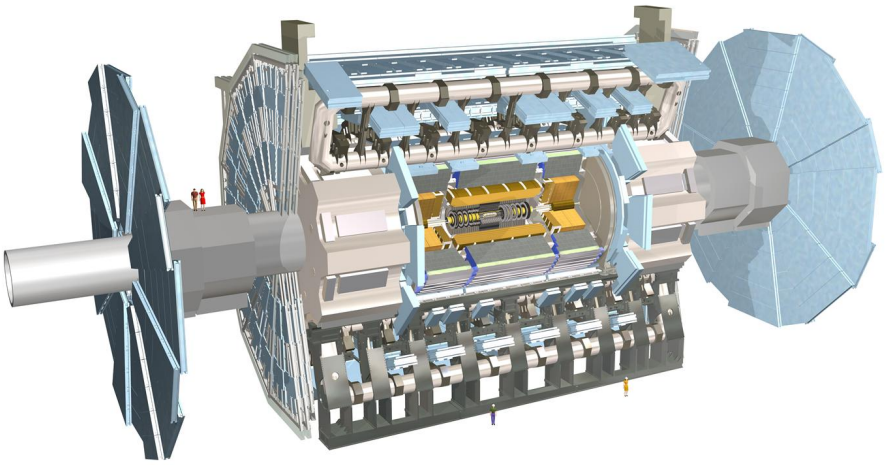

Figure 2.2: The ATLAS detector

The inner detector

The beam pipe with a radius of 36 mm is surrounded by the inner detector (ID) that is responsible for the reconstruction of tracks, vertices and the determination of momenta and charges of traversing particles. It is divided into the following three subparts:

- pixel detector
- silicon microstrip tracker (SCT)
- transition radiation tracker (TRT)

The whole ID (figure 2.3a) is immersed in a 2 T magnetic field that extends over a length of 5.3 m, diameter of 3.5 m and that is created by the central solenoid. As a consequence, charged particles that are flying through the inner detector have bend curves (seen from the transverse plane) from which one can conclude the sign of the particle's charge and its momentum.
For the pixel detector, pixel sensors of $50 \times 400\ \mu m^2$ are used. They are arranged on 3 concentric cylinders around the beam axis in the barrel region. Highest granularity can be achieved with the layer closest to the beam pipe, often referred to as "b-layer", which lies at a radius of 51 mm and is important for the reconstruction of secondary vertices like from tau- or b-decays. In the end-cap region, 2×3 disks are used that are perpendicular to the beam pipe.
Around the pixel detector lies the SCT. It consists of four cylindrical layers giving a precise measurement of the $R - \phi$ coordinate. Each detector module is built of two daisy-chained sensors with a strip pitch of 80 μm giving one space point. For the end caps, 2×9 disks with radially running strips are used.
With the pixel detector and SCT it is possible to do precision tracking up to a pseudorapidity (see section 2.1.2) of $|\eta| < 2.5$.
The last part of the ID is the TRT that usually provides a large number of hits (≈ 30) per track by its 4 mm diameter straw tubes. The TRT just provides information in the $R - \phi$ plane and enables track-following up to $|\eta| = 2.0$. For the barrel region the straws are arranged parallel to the beam axis and exhibit a length of 144 cm while in the end-cap region, the straws are arranged radially and have a length of 37 cm.
With the combination of the precision trackers around the beam pipe and the TRT it is possible to achieve a high precision in track and momentum measurement.

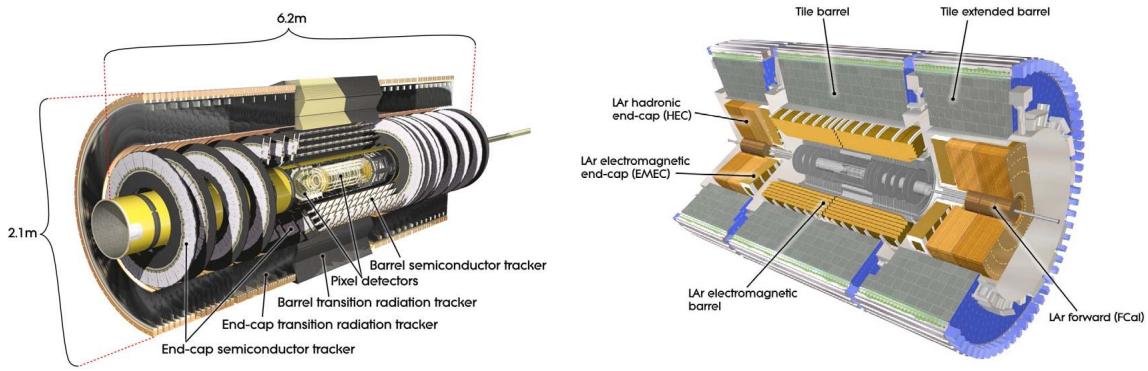

(a) ATLAS inner detector

(b) ATLAS calorimeter

Figure 2.3: Inner view of some parts of the ATLAS detector

The calorimeter

In the calorimeter (figure 2.3b), all the produced particles should deposit their entire energy. The calorimeters used in ATLAS cover the range of $|\eta| < 4.9$ and the full ϕ range. It is divided into an electromagnetic (EM) and a hadron calorimeter.

The electromagnetic calorimeter
The EM calorimeter itself is also divided into a barrel part ($|\eta| < 1.475$) and two end-cap parts ($1.375 < |\eta| < 3.2$). In this part of the detector, electrons and photons should deposit their energy by undergoing bremsstrahlung and pair production, thus building an electromagnetic shower. To achieve this requirement, the total thickness in the barrel is > 22 radiation lengths (X_0) and > 24 radiation lengths in the end cap. X_0 is the length at which a particle holds only $\frac{1}{e}$ of its initial energy. The calorimeter itself is arranged in an accordion geometry for the absorbers and electrodes, so that no cracks in ϕ direction can be observed. For the absorber material, lead is chosen whereas liquid argon serves as active material for the energy measurement. The resolution of the EM calorimetry is up to $\frac{\sigma_E}{E/\mathrm{GeV}} = \frac{10\%}{\sqrt{E/\mathrm{GeV}}}$.

The hadron calorimeter
As the name already suggests, this calorimeter has the duty to stop all the hadrons and measure their energy. The central part of it is the tile calorimeter with one barrel that reaches up to $|\eta| < 1.0$ and two extended barrels from $0.8 < |\eta| < 1.7$. They are arranged right behind the EM calorimeter envelope. Steel is used as absorber and scintillating tiles as active material. Two wheels per end-cap are placed behind the end-cap EM calorimeter. Liquid argon is used here as active material just like for the EM calorimeter, whereas copper is the passive material. The hadronic end-cap calorimeter extends out to $|\eta| < 3.2$. Its resolution is the same as for the barrel part and is about $\frac{\sigma_E}{E/\mathrm{GeV}} = \frac{50\%}{\sqrt{E/\mathrm{GeV}}}$. There are also forward calorimeters that provide coverage over $3.1 < |\eta| < 4.9$. It is important to cover as much of solid angle as possible to achieve a precise measurement of E_T^{miss}.

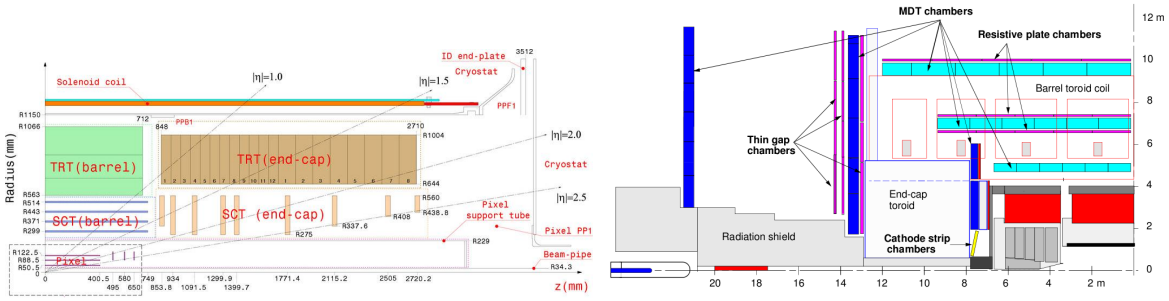

(a) Sideview schematics of the detector

(b) The muon spectrometer

Figure 2.4: Sideview of some parts of the ATLAS detector

The muon spectrometer

Muons produced in the collision don't deposit much of their energy in the calorimeter and need an extra device to detect them, this is the muon spectrometer (see figure 2.4b). It covers the range of $|\eta| < 2.7$ for reconstruction and $|\eta| < 2.4$ for triggering of muons with momenta between 3 and 1000 GeV. The concept of muon detection is based on bending their tracks in a magnetic field combined with trigger and high-precision track chambers. For the range up to $|\eta| < 1.4$, the magnetic field is provided by a large barrel toroid. In the end-cap region two smaller magnets are inserted into the ends of the barrel toroid, covering the range $1.6 < |\eta| < 2.7$. The spectrometer partially consists of monitored drift tube chambers measuring the η-coordinate up to $|\eta| < 2.7$ except for a region in the inermost end-cap layer. The other device for precision momentum and tracking measurement for muons are cathode-strip chambers used in the forward region ($2.0 < |\eta| < 2.7$). Here they provide higher rate capability and time resolution than the monitored drift tubes and also give a rough estimation (of the order of 1 cm) of the ϕ-coordinate.
In addition to the precision momentum measuring devices, there are resistive plate chambers (RPC) and thin gap chambers (TGC) that take care of triggering. The RPCs are placed in the barrel region ($\eta < 1.05$), while the TGCs are use in the end-caps ($1.05 < |\eta| < 2.4$). Both chambers can give a signal in the order of ten nanoseconds , which is required when going to small bunch spacing and therefore high luminosity.
Together with the measurements of calorimeter and inner detector, muons can be very well recontructed.

The trigger system

The collisions at the LHC take place at such a high rate, that not all events can be recorded because of limited disk space. However, most of them are minimum-bias events that are not interesting for the physics one wants to analyse. Hence, a trigger system is required to reduce the rate at which and what kind of events are recorded. In ATLAS , a three-level trigger system is used. The level-1 (L1) trigger searches for high transverse momentum objects using the information of the RPC and TGC for muons and the calorimeter systems for all other objects. E_T thresholds and the multiplicities of objects in trigger towers of 0.1×0.1 granularity in $\Delta\eta \times \Delta\phi$ are used to make a decision. This decision to keep an event is made in 2.5 μs and reduces the output rate to 75 kHz. In contrast to the L1 trigger, the L2 trigger is software-based and uses regions-of-interests (RoI), which are regions in the detector with interesting objects provided by the L1 trigger. The RoI uses information of p_T, η and ϕ of the L1 object and constructs a window around it. In that way, only the data in this region is used for the further

trigger decisions and not the data of the entire event, which would slow down the whole process. The L2 trigger repeats the analysis of the L1 trigger with improved resolution and also uses information like reconstructed tracks from the ID. The output rate can then be reduced to 2 kHz. The last link in the trigger chain is the Event Filter (EF), that has to further reduce the rate to 200 Hz, what corresponds to about 300 MB/s. It uses additional algorithms to the events that passed the L2 stage to achieve this.

2.1.2 Important variables

The coordinate system of the ATLAS experiment is righthanded with its origin lying in the middle of the detector, also called nominal interaction point. The direction of the beam defines the z-axis. The positive x-axis is pointing from the nominal interaction point to the centre of the LHC ring, while the positive y-axis is pointing upwards. Instead of using x and y for the plane transverse to the beam, one can also use the azimuthal angle ϕ, measured around the beam axis, and the polar angle θ, measured from the beam axis. Another important variable is the pseudorapidity η, which is defined as $\eta = -lntan(\theta/2)$ and that can be seen as an alternative to the polar angle. For relativistic particles, it is equal to the rapidity $y = \frac{1}{2} ln\left(\frac{E+p_z}{E-P_z}\right)$. Using the pseudorapidity brings the advantage that the number of observed particles per pseudorapidity interval is almost constant over a large range. It is also useful, since differences in pseudorapidities $\Delta\eta$ then become Lorentzinvariant. This is an important fact for the measurement of distances done in such a collider experiment. As a kind of distance measurement, the variable $\Delta R = \sqrt{(\Delta\phi)^2 + (\Delta\eta)^2}$ is defined.
The LHC is a proton-proton collider with a well-defined center-of-mass energy which is given by the sum of the two protons. Unfortunately, the protons themselves do not interact in the collision, but more its constituents (quarks and gluons) that carry an undefined fraction x of the proton's momentum. The proton remnants usually stay undetected as they still fly along the beam pipe. Therefore, the center-of-mass energy of the interaction is not known and the interaction system itself can be Lorentz-boosted with respect to the z-axis when constituents with a different momentum fraction x collide. The only component that stays constant throughout the whole collision is the transverse momentum $\vec{p}_T$, defined as

$$\vec{p}_T = \begin{pmatrix} p_x \\ p_y \end{pmatrix}.$$

The transverse energy $\vec{E}_T$ is defined in a similar way, where the entries of the different calorimeter cells are summed vectorially. The transverse momentum and energy should usually be close to 0 like before the interaction, neglecting efficiency and resolution effects. This is often not the case since weakly-interacting particles like the neutrino leave the detector without any significant energy deposition. Therefore one defines the missing transverse energy as

$$\vec{E}_T^{miss} = -\sum \vec{E}_T.$$

For the later analysis, one usually uses the absolute values of these vectors.

Chapter 3

Theory

This chapter gives a brief summary of the Standard Model and its properties and problems. Afterwards the basic idea of Supersymmetry and some solutions to the Standard Model problems are explained.

3.1 The Standard Model

The Standard Model theory of particle physics proposed by Weinberg and Salam in the late 60's is a theory to describe the electromagnetic and weak interactions between elementary particles [1]. Among other things it explains the coupling of spin-$\frac{1}{2}$ particles to the mediator of the forces, the gauge bosons. The gravitational force is not relevant in particle physics since the gravitational coupling between two particles is negligible. This theory made predictions on the existence of particles and their properties like the mass or the spin. Collider experiments like LEP at CERN or the Tevatron at the Fermilab showed very good agreement between the predictions and the measured values (for example for the masses of the W and Z boson) which made the Standard Model the most successful theory of particle physics yet. A sketch of the discovered particles and their properties can be found in figure 3.1.
Mathematically it is based on the $SU(3) \times SU(2) \times U(1)$ group. The $SU(3)$ factor describes the strong interactions (QCD) with the strong coupling g_s and 8 gauge bosons, which are the gluons of different color content. It acts the same way for left- and righthanded particles, why it is also called a non-chiral gauge group. The electroweak sector is defined by the $SU(2) \times U(1)$ factor. The $SU(2)$ part of it is described by a gauge coupling g and the gauge bosons W^1, W^2 and W^3. Contrary to the QCD sector, it only acts on lefthanded particles. The last factor is the $U(1)$ gauge group with the coupling g' and the corresponding gauge Boson B^0. Since it acts on left- and righthanded particles with different strength, it is also chiral.
The Lagrangian density containing the kinetic terms of the particles and potential terms has to be invariant under this gauge group. The invariance condition gives us the coupling strengths between the fermions and the mediated bosons and the masses of these bosons, which is always zero for such an invariance requirement. Yet, for example the small range of the weak force suggested massive exchange particles. So this theory cannot be complete. Furthermore, there are also no mass terms for fermions because they would break the $SU(2) \times U(1)$ symmetry. Hence, the symmetry must be broken at some point, in this case transforming $SU(2) \times U(1) \rightarrow U(1)_{em}$. In the following, a common solution to this problem will be explained.

3.1.1 The Higgs mechanism and spontaneous symmetry breaking

A new field ϕ and the corresponding potential $V_\phi = -\frac{1}{2}\mu^2\phi^2 + \frac{1}{4}\lambda\phi^4$ are introduced to the Lagrangian density. The potential can only contain even powers of ϕ to be invariant under $\phi \rightarrow -\phi$. Powers greater equal 6 are forbidden because of renormalisability. To have a sufficient amount of degrees of freedom

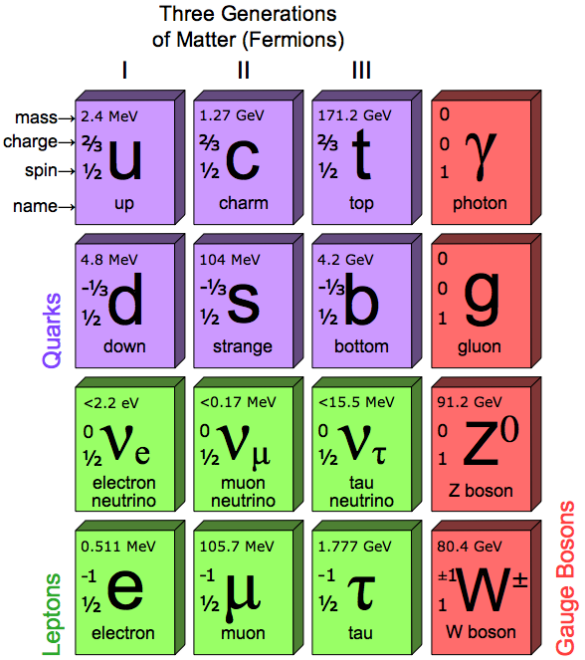

Figure 3.1: Particle content of the Standard Model of particle physics that has been discovered so far. The number for the masses of the particles (like for the top quark) don't have necessarily to match the latest official numbers. Taken from [14]

to create masses for our known massive gauge bosons, a complex scalar doublet is chosen for ϕ:

$$\phi = \begin{pmatrix} \phi^+ \\ \phi^0 \end{pmatrix} = \begin{pmatrix} \phi_1^+ + \phi_2^+ \\ \phi_1^0 + \phi_2^0 \end{pmatrix} \tag{3.1}$$

Assuming μ and λ to be positive in the potential term leads to a minimum of the field, which lies on a circle with $|\phi^2| = \frac{-\mu^2}{\lambda} \equiv \frac{v}{\sqrt{2}}$ (see fig. 3.2). In order to retrieve the mass states of particles in the Lagrangian density, one usually looks at the fluctuation of the field around the ground state, also called vacuum expectation value (vev). Since one of the vev on the circle has to be arbitrarily chosen, the symmetry is now broken.

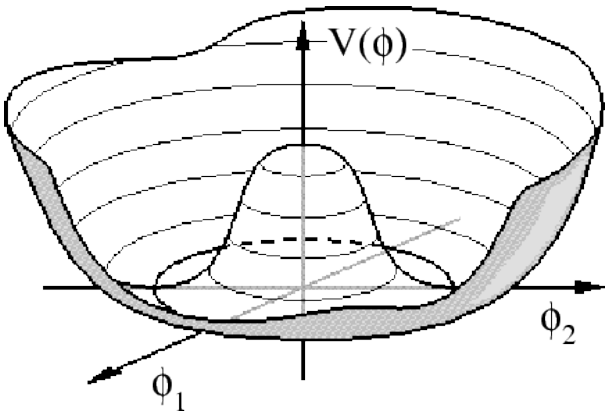

Figure 3.2: Higgs field potential; ϕ_1 and ϕ_2 are equivalent to ϕ^+ and ϕ^0 in equation 3.1

The field ϕ can now be rewritten as a sum of the vev v and a scalar field h with zero vacuum expectation value [15]. As all points on the circle in figure 3.2 are equal, one can choose one of them. Our field has therefore transformed to:

$$\phi = \begin{pmatrix} 0 \\ v + h \end{pmatrix} \tag{3.2}$$

The additional term in the Lagrangian density due to the field ϕ should also be invariant under the $SU(2) \times U(1)$ transformation. Using the expression of it above for the kinetic term of this field and requiring gauge invariance, one ends up with mass terms for Z and W boson, which are now mixtures of the B^0 and the W^i with $i = 1, 2, 3$:

$$M_W = \frac{gv}{\sqrt{8}} \tag{3.3}$$

$$M_Z = \frac{\sqrt{g^2 + g'^2}v}{\sqrt{8}} \tag{3.4}$$

Furthermore, the field ϕ allows mass terms for fermions by a so called Yukawa coupling between the fermions and the field.

Despite the success of the Standard Model, it is not considered as the ultimate theory that explains the whole particle physics world. There are some reasons that theoretical physicists build new theories with other symmetry groups that contain the Standard Model symmetry:

- The SM looks rather complicated and it contains many parameters that can not be predicted but have to be measured in experiments. The spontaneous symmetry breakdown is introduced ad hoc to explain the masses of the fermions and gauge bosons.
- Gravity is not included in this theory. So it has to break down at a certain scale. One usually assumes the Planck scale $M_{planck} \approx \frac{1}{\sqrt{G_{Newton}}} \approx 2 \cdot 10^{19}$ GeV.
- The loop corrections to the higgs mass give a quadratic divergence on the new physics scale.
- Masses of the neutrinos cannot be explained by the Standard Model.
- The matter described by the SM is only a fraction of the whole matter in the universe. It can not explain dark matter.

3.2 Supersymmetry

One of the main approaches to new physics in the last decades is the theory of supersymmetry (SUSY). It introduces a new generator Q that only acts on the spin of a particle leaving all the other properties invariant. Hence, it changes fermions to bosons and vice versa:

$$Q|fermion> = |boson> \qquad\qquad Q|boson> = |fermion> \tag{3.5}$$

The particle content is doubled by this operation. The fermion partners get an extra "s" before their names, so the supersymmetric partner of the electron is called the selectron. The partner of the gauge bosons end with "-ino", so having Higgsinos, Wino or short gauginos. Since Q commutes with all other operators (e.g. the momentum operator P_μ), the supersymmetric partners of our SM particles should have the same mass. Of course, nobody has ever observed a selectron with a mass of 0.51 MeV. Therefore, SUSY has to be a theory that is broken at the energy scales we have observed so far. The SUSY breaking introduces more than 100 new parameters that have to be determined in experiments. However, many parameters can be constrained by theoretical assumptions or existing experiments leading to a smaller amount of free parameters. One realisation of SUSY is the Minimal Supersymmetric Standard Model (MSSM) that is, as the name already says, a supersymmetric extension of the SM. It's minimal in a way, that except for a second Higgs doublet and of course all the superpartners, no further particles are introduced (see tables 3.1 and 3.2). Two doublets are required in SUSY models to cancel loop corrections to the higgs mass, for example, so that no fine-tuning is necessary. In the MSSM exist models that explain the supersymmetric breakdown through different interactions. One of them is minimal supergravity (mSUGRA), where this happens via gravitational interactions. mSUGRA and mSUGRA-like models have the great advantage, that they can be described by just a few free parameters. Parameters in such a kind of models mostly include mass scales of gluinos, sleptons, gauginos or the vacuum expectation values of the two Higgs doublets.
The different superpartners of the gauge bosons, the gauginos, mix in a way to form the charginos and neutralinos. There are two charginos $\chi^\pm$ and four neutralinos χ^0 (the superscript denotes the particle's charge), where the lightest neutralino χ_1^0 is in many models considered as the lightest supersymmetric particle (LSP) and thus a candidate for dark matter. This can be seen by the so called R-Parity $R_P \equiv (-1)^{3(B-L)+2s}$ introduced in many SUSY models, where B is the baryon number, L the lepton number and s the spin of the particle. SM particles have $R_P = 1$, whereas SUSY particles have $R_P = -1$. The collisions in the LHC tunnel take place for protons or their constituents, thus the initial R-Parity[1] is well-defined and equal to 1. If the R-parity has to be conserved, SUSY particles must be produced in pairs and decay until the LSP is produced. The LSP can neither decay to a lighter sparticle nor to two SM particles because this would violate R_P.
A nice feature of the MSSM is, that due to additional loop corrections, a unification of the three coupling constants at a high energy scale is possible (figure 3.3).

[1] R_P is multiplicative

Names		spin 0	spin 1/2
squarks, quarks (x3 families)	Q	$(\tilde{u}_L\ \tilde{d}_L)$	$(u_L\ d_L)$
	$\bar{u}$	$\tilde{u}_R^*$	u_R
	$\bar{d}$	$\tilde{d}_R^*$	d_R
sleptons, leptons (x3 families)	L	$(\tilde{\nu}_L\ \tilde{e}_L)$	$(\nu_L\ e_L)$
	$\bar{e}$	$\tilde{e}_R^*$	e_R
Higgs, higgsinos	H_u	$(H_u^+\ H_u^0)$	$(\tilde{H}_u^+\ \tilde{H}_u^0)$
	H_d	$(H_d^0\ H_d^-)$	$(\tilde{H}_d^0\ \tilde{H}_d^-)$

Table 3.1: Chiral supermultiplets in the Minimal Supersymmetric Standard Model; taken from [16]

Names	spin 1/2	spin 1
gluino, gluon	$\tilde{g}$	g
winos, W bosons	$\tilde{W}^{\pm}\ \tilde{W}^0$	$W^{\pm}\ W^0$
binos, B boson	$\tilde{B}^0$	B^0

Table 3.2: Gauge supermultiplets in the Minimal Supersymmetric Standard Model; taken from [16]

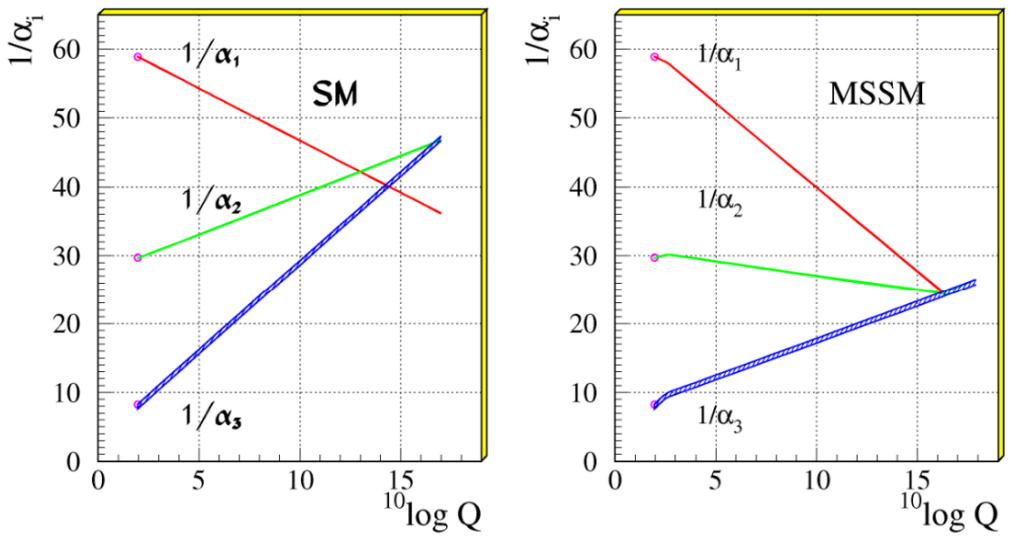

Figure 3.3: Running coupling constant for the Standard Model and the MSSM

Chapter 4

Signal and background processes

Before trilepton events can be analysed in simulated data, the possibilities to get the desired final state has to be discussed for signal and background.

4.1 Production of trilepton events in SUSY

There are several ways how trilepton events can be produced in SUSY. Essential for reaching such a final state is the production of charginos and neutralinos that offer the possibility of cascade decays. One way to get a gaugino pair is the production of squark-squark, gluino-gluino or squark-gluino pairs as it is favored by the strong interaction due to the large coupling strength and therefore high cross section of strong interacting particles compared to the weak interaction (see fig 4.1). A problem of the gluinos is

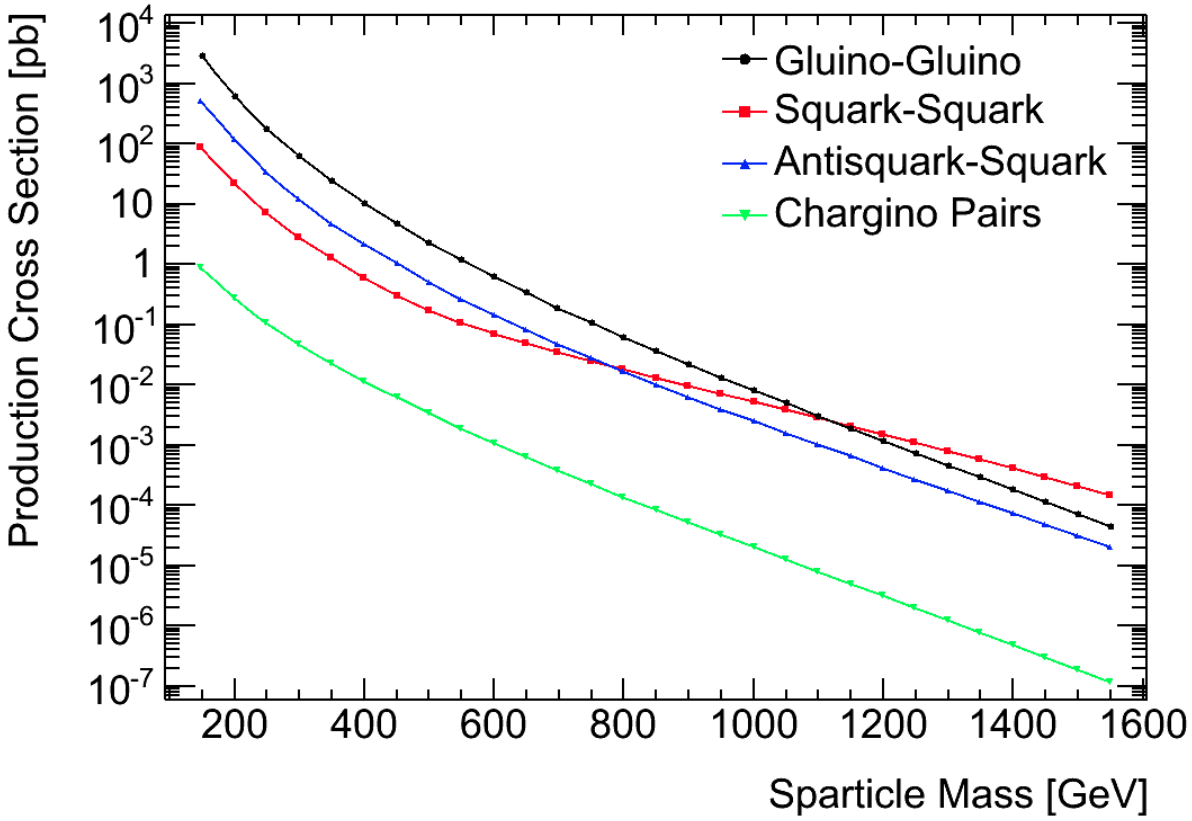

Figure 4.1: Example plot for the production cross section of light SUSY particle, when other sparticles are set to a mass of 4.5 TeV. Taken from [17]

that they cannot decay to neutralinos and charginos at one vertex [18], so one should have a closer look on the squarks, that can decay to a neutralino/chargino and a quark. Nevertheless, gluinos can decay to squarks and so also contribute to the signal. To get the trilepton final state, one of the squark decays has

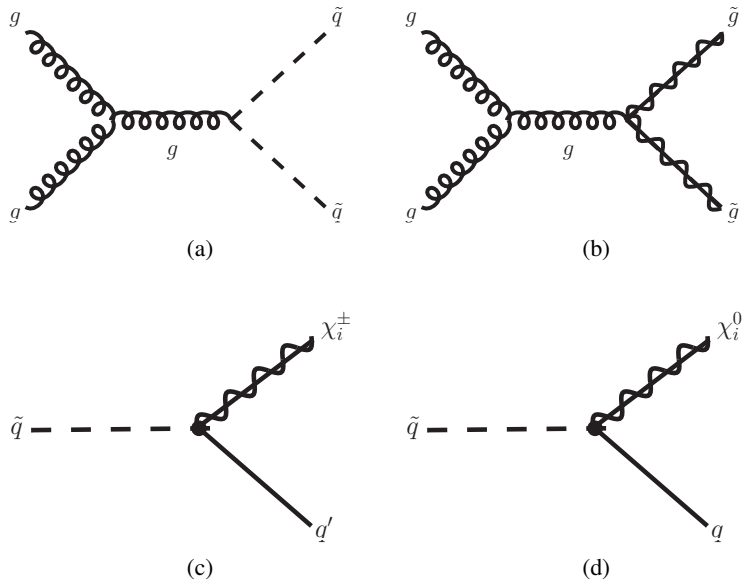

Figure 4.2: Squark production and decay to gauginos.

to contain a chargino and for the other one a neutralino which is not the lightest neutralino. Our desired trilepton event is then reached by a combination of the decays in figure 4.3.

At the end of the chargino decay we have on lepton, the corresponding neutrino and the lightest neutralino. The neutralino decay provides two leptons of opposite charge and the same flavour and again a lightest neutralino. To summarize, one ends up with three leptons, one from the chargino decay and two from the neutralino decay. Furthermore one gets one neutrino and two lightest neutralinos which are assumed to be stable and only weakly interacting (if it is the lsp). This leads to significant amount of E_T^{miss} compared to SM processes. In this trilepton signature, there should also be two jets from the gaugino production via the squarks. Charginos and neutralinos can also decay with higgs particles or higgsinos involved. This kind of decay process is not considered here, as it will not be part of the signal that will be analysed in Monte Carlo in chapter 5.

The ATLAS groups have already done a lot of work in excluding mass ranges for gluinos and squarks (see fig 4.5) for various scenarios and simplified models that are not constrained by a certain model. As the excluded masses for squarks and gluinos increase, so decreases their production cross section and the direct gaugino pair production becomes also important as their possible masses still cover a wide range down to masses of order 100 GeV. For the trilepton case, a representative of this mechanism would be the associated chargino-neutralino production by a virtual W boson (fig. 4.4). The event topology is the same as for trilepton events from squark-squark production except for the two jets from the neutralino and chargino production. The lack of two signal jets changes the composition of the background significantly, becoming more WZ-like and less like the event signature from $t\bar{t}$. Therefore it will not be considered in this analysis.

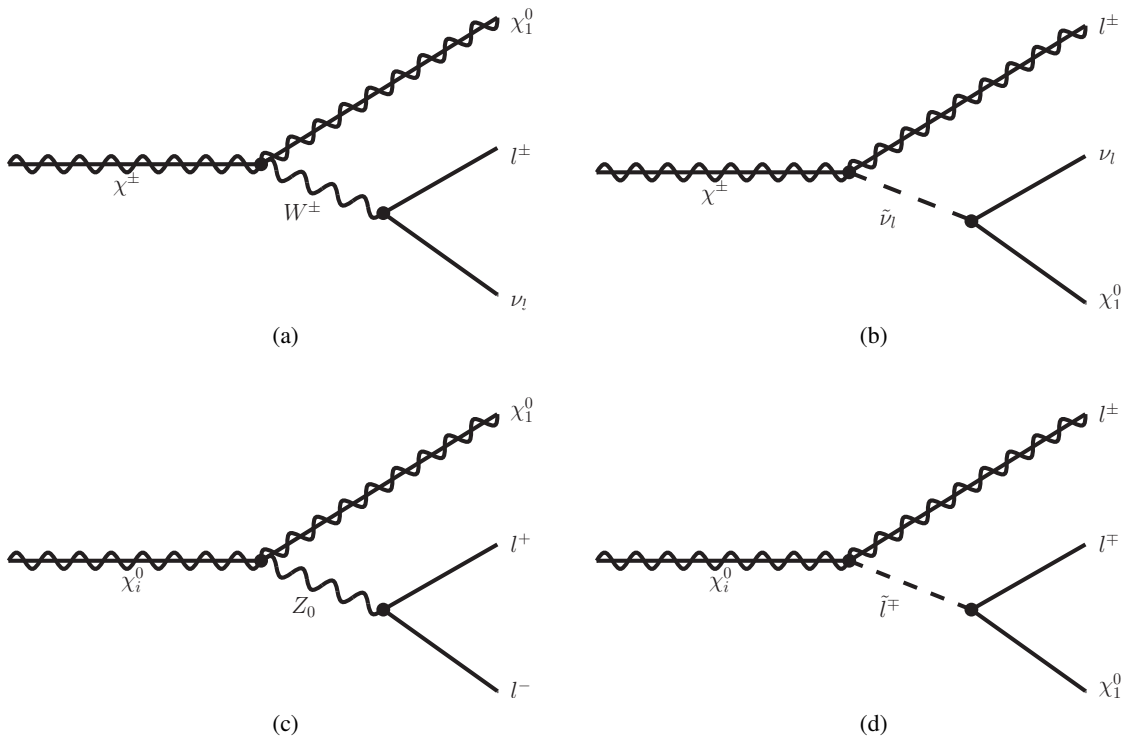

Figure 4.3: Possible chargino and neutralino decays leading to a three lepton final state

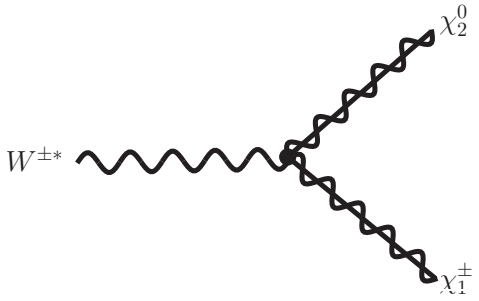

Figure 4.4: Associated chargino-neutralino production by a virtual W boson

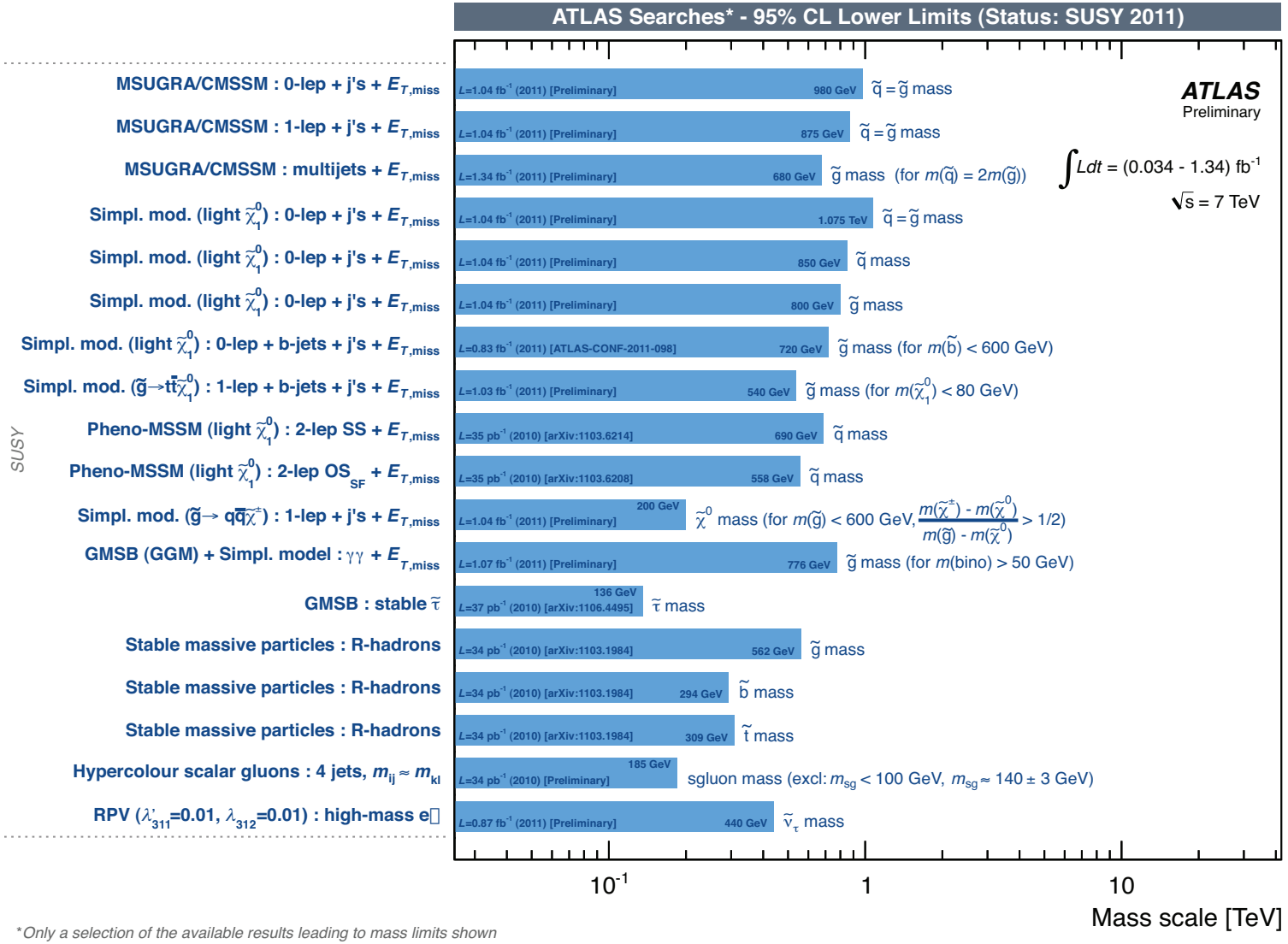

*Only a selection of the available results leading to mass limits shown

Figure 4.5: Exclusion plot for various SUSY models and assumption as done by the ATLAS SUSY group in 2011 [19]

4.2 Standard Model background

Although trilepton events coming from standard model processes are very rare, the desired signal is not completely free from background. This becomes more and more important the smaller the cross section and branching ratio for the signal is. The background can be divided into two parts. On one hand there are contributions from processes that generate at least three prompt leptons from the hard scattering. These events and leptons are considered as "real". On the other hand, there are events that have less than three prompt leptons, but that can produce secondary leptons by photon conversion or a semileptonic b-decay or other decays. It can also happen, that a light jet is misreconstructed as an electron due to its shower shape in the electromagnetic calorimeter. These events and leptons are called "fake"[1].

Real trilepton background:
The only contribution comes from the diboson production, i.e. ZZ and WZ. For the ZZ case, both Z's can decay leptonically producing 4 prompt leptons. If one of the leptons is not reconstructed or somehow lost in the detector, one has a well defined trilepton final state without significant E_T^{miss} or jets from the hard scattering. If a WZ pair is produced, both bosons again have to decay leptonically. This results in a final state with three leptons and /etmis from the leptonical W decay, where also a neutrino is produced. Jets can only occur from initial state radiation. Leptons from W or Z decays have very high p_T because of the large boson masses.
Fake trilepton background:
The largest fake contribution comes from the ttbar production. The top quark decays to almost 100 % to a W boson and a b quark. The two W bosons decay leptonically giving two leptons, whereas the b quark can decay semileptonically giving another lepton (see figure 4.6a). This lepton will usually not satisfy the object selection requirements and be considered as part of the jet. Nevertheless, it is possible that it survives the selection giving the additional lepton. Events from ttbar carry large E_T^{miss} due to the neutrinos from the W decay, at least two jets and the possibility to generate a third lepton, which gives a signal like signature in the detector (see table 4.1).
Another process to produce a fake event is the Drell-Yan process, where a Z boson or a virtual photon is produced decaying to two oppositely charged leptons. One of the leptons can undergo bremsstrahlung. If the resulting photon is emitted in the inner detector, it will very likely convert to two additional electrons (see figure 4.6b). If it is emitted outside the inner detector, the photon will create a shower in the electromagnetic calorimeter depositing all its energy. This shower can accidentally be matched to a track building a fake electron. Although the Drell-Yan process does not create E_T^{miss} and additional jets can only be produced by initial state radiation, its large cross section makes it to one of the major trilepton backgrounds.
Other processes like QCD or W boson production are not considered for the later signal region. Despite their high cross sections, the probability to create more than one fake lepton is really small. Combined with the lack of jets or E_T^{miss} , these processes will not be regarded as background for the SUSY signal.

[1] even though secondary leptons are properly reconstructed and actually not fakes, they will also be considered as fake leptons

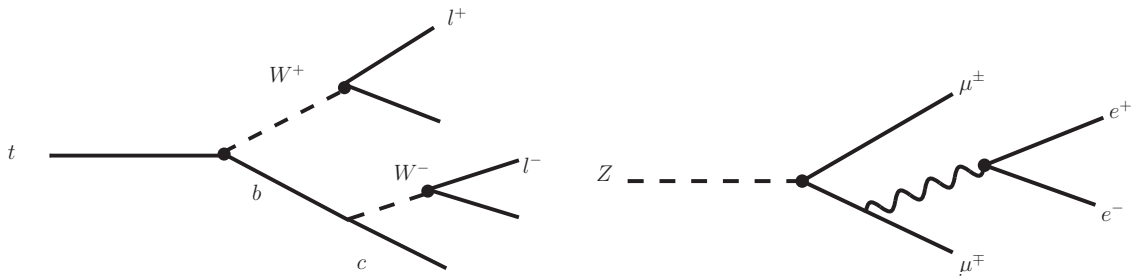

(a) top decay + secondary lepton from semileptonic b-decay (b) leptonic Z decay + secondary lepton from photon conversion

Figure 4.6: Possibilities to get a secondary lepton from top and Z decay

process	cross section [pb^{-1}]	# real lep.	E_T^{miss}	# jets	with Z
ZZ	≈ 0.85	4	no	no	yes
DY + jets	$\approx 1330 \cdot 0.2^{(\#\text{ of add. jets})}$	2	no	just by ISR	yes
WZ	≈ 3.5	3	yes	no	yes
$t\bar{t}$	≈ 89	2	yes	2	no
SUSY signal	see appendix A	3	yes	2	can be decay product

Table 4.1: Properties of SM background to the desired SUSY signal; cross sections taken from [20]; ISR = initial state radiation

Chapter 5

Monte Carlo analysis

This chapter describes the analysis done solely with Monte Carlo samples. Object definitions are introduced, the trilepton background investigated and a signal-optimized analysis performed.
Information about the different Monte Carlo samples used for this analysis can be found in appendix A.
The complete analysis is based on release 16(.6.5.5.1) of `Athena`, the reconstruction program of ATLAS.

5.1 Object definitions

The reconstructed objects used in the analysis like electrons, muons and jets have to fulfill certain requirements to be considered as this object. The efficiency of correctly reconstructing objects should be high while the probability to misidentify an object should be kept low. This section lists these different object definitions that were predominantly taken from the ATLAS top reconstruction group [21] :

5.1.1 Electrons

Reconstructed electrons are identified by a combination of clusters in the electromagnetic calorimeter and tracks from the inner detector. The definitions follow the e/gamma recommendations for the 2011 analysis [22].
Only electrons requiring the isEM-tight definition are considered for the analysis. To have electrons inside the coverage of the electromagnetic calorimeter and to avoid the crack region between barrel and end-cap, the electron objects have to be in the regions $0 < |\eta| < 1.37$ and $1.52 < |\eta| < 2.47$. Furthermore, a transverse energy of $E_T > 20$ GeV is required. To suppress the contribution of electrons from heavy flavor decays or fake electrons from light flavor jets, a calorimeter isolation of $E_T^{cone20} < 3.5$ GeV must be fulfilled. For electrons with a $p_T < 30$ GeV, this requirement changes to $E_T^{cone20} < 1.5$ GeV. The superscript $cone20$ indicates the radius in ΔR, for which the E_T is calculated, in this case $\Delta R = 0.2$. To correct for the energy that the electron deposited itself in the calorimeter, the energy measured in a calorimeter cell window of 5x7 in the electromagnetic calorimeter is subtracted [23]. If the value of the $E_{T,cone}$ variable is still high after that correction, this energy probably comes from nearby hadrons.
Scale factors (SF) are applied for the trigger efficiency, the reconstruction efficiency and the electron identification. Due to differences of these values between Monte Carlo simulation and real data, the efficiencies from Monte Carlo are scaled to match the data efficiencies. The scale factors are measured as a function of p_T and η. The energy of electrons in data is scaled to shift the Z peak to the exact Z mass. Furthermore, the energy of all electrons in Monte Carlo is smeared so that the invariant mass distribution of two electrons around the Z mass shows good agreement between MC and data. All scales applied to electrons are provided by the top reconstruction group [24].

5.1.2 Muons

Muons are taken from the MuidMuonCollection where only combined muons are taken from. This means that information from the inner detector and the muon spectrometer is used to reconstruct the muon object. They also have to pass the tight selection according to Muid [25]. Additional cuts are a transverse momentum of $p_T > 15$ GeV, $|\eta| < 2.5$, $p_T^{cone30} < 4$GeV, $E_T^{cone30} < 4$GeV. For muons with a $p_T < 30$ GeV, one requires $E_T^{cone30} < 2$GeV. Similar to elecrons, E_T^{cone30} is the E_T in a cone of $\Delta R = 0.3$. p_T^{cone30} is the summed p_T of tracks in a cone of the same size around the muon [23]. To reject muons from heavy or light flavor decays, every muon within a cone of $\Delta R < 0.4$ to a jet of $p_T > 20$ GeV is removed from the event.
Additional hit requirements for muons are [21]:

- Number of b-layer hits > 0
- Number of pixel hits + number of crossed dead pixel sensors > 1
- Number of SCT hits + number of crossed dead SCT sensors >=6
- Number of pixel holes + number of SCT holes < 3
- with n = number of TRT hits + number of TRT outliers:
  - $|\eta|$ < 1.9: n > 5 and (number of TRT outliers)/n < 0.9
  - $|\eta|$ >= 1.9: (number of TRT outliers)/n < 0.9 only if n > 5

An additional procedure to reject cosmic muons is also applied and described in [21].

5.1.3 Jets

The reconstruction algorithm for jets is AntiKt 0.4 TopoCluster with EM+JES calibration, where jets with negative energy are removed. Every reconstructed jet with a a $E_T > 20$ GeV is kept for the event. Further information on jets can be found in [26] One important fact that one has to consider when it comes to jets is, that almost every electron is also independently reconstructed as a jet due to its shower shape in the elctromagnetic calorimeter. This implies of course a double counting of the electron's energy. To avoid this double-counting, every selected [1] electron closer to a jet than $\Delta R = 0.2$ is removed from the event.
Jets that originate from b-quarks are tried to be tagged as 'b-jets'. Due to the large mass of the b-quark, they have a a lifetime that allows them to travel few mm in the detector before they decay and hadronize, which results in a secondary vertex that is used for b-tagging. The top reconstruction group provides different algorithms to tag those b-jets. In chapter 6, one of them is used to get a fake lepton rate from b-jets.

5.1.4 Additional information

E_T^{miss} is calculated by the objects passing the object selection. This alone would not give the correct E_T^{miss} because there are still many low energetic particles that do not survive the requirements of the different objects. Additional jets with a transverse momentum 20 GeV > p_T > 7 GeV are also added to the E_T^{miss} term. The remaining energy in the calorimeter that did also not belong to the low energetic jets, is then included in the E_T^{miss} calculation, too.

[1] Every object that passes the electron object selection

One important effect for a collider like the LHC is the pileup. Due to the enormous number of particles and bunches, there is not only one interaction per bunch crossing, but up to 24 for the design properties of the LHC. The small bunch spacing allows to measure even particles from the previous bunch crossing. This effect has to be included in the analysis. To some point, it is already included in the production of the Monte Carlo samples, but the real data conditions can only be guessed by that. Therefore the average number of pileup interactions has to be scaled to match the Monte Carlo with the data distribution by a tool provided by the ATLAS collaboration [27].

5.2 Background studies

In order to analyse and search for a certain signal hypothesis, its background has to be understood very well. The dominant background processes have already been discussed in chapter 4.2. First MC studies showed, that those are really the only processes contributing to final states with three leptons. QCD or W+jets are therefore not further investigated or shown in the following plots.
First of all, the statements given in chapter 4.2 have to be verified and the named properties to be compared to the signal. The use of Monte Carlo gives the possibility to look at the "truth" information of the reconstructed objects. For this purpose, information from the MCTruthClassifier [28] tool is used. As the name already suggests, it classifies the particles according to their origin, i.e. an electron coming from the decay $t \rightarrow W^+b \rightarrow e^+\nu_e b$ would have the top-quark as its origin. Figure 5.1 shows the particle's origin for all the trilepton events surviving the object selection criteria and some quality cuts that are explained later. For the electrons one can see the large contribution from the WZ decay into three leptons which is the dominant background when looking at all trilepton events. It is interesting to see, that there are not only prompt leptons from the decay of one of the bosons, but there is also a contribution from photon conversion which leads to a fake event. The same is valid for the other diboson production processes WW and ZZ, where ZZ is of more importance due to its larger amount of prompt leptons. The largest fake contribution from photon conversion comes from the DY process or better to say the decay of the Z boson, where an electron or muon undergoes bremsstrahlung and produces an electron-positron pair. But this is not the only possibility for a Z decay to end up as a trilepton event. In rare cases, additional heavy flavor jets can produce secondary electrons (see b-meson bin) that give us the third lepton. Fake trilepton events from top pair production is also clearly visible. The prompt leptons are coming from the top while the third lepton mostly comes from heavy flavour jets and the involving semileptonic decay of a b-meson. Some additional fake top trilepton events can occur due to photon conversion. The origin plot for muons shows a similar result like for electrons. Only the photon conversion bin is not filled, because it's very unlikely to produce a muon-pair instead of two electrons due to the high mass of the muon. In general, the bins where one expects prompt leptons like top, W and Z, is higher for muons than for electrons because of the better reconstruction and identification efficiencies of muons compared to electrons. Secondary electrons from heavy flavour decays are equally probable for both particle types, whereas a large amount of electrons can also come form photon conversion. It is hard to say in how far misreconstructed (light) jets are considered in the particle origin. Either in some light meson bin that is not filled for those reconstructed trilepton events or in the first bin, where the particle origin is not defined. Every particle, for which the MCTruthClassifier algorithm fails, has "not defined" as its origin. Why this happens a lot more often for muons than for elecrons, was not further investigated in this thesis. As a closer look, the p_T-distributions of particles with origin "not defined", "photon conversion" and "b-meson" are shown in figure 5.2. While particles from heavy flavour decays usually have quite low p_T (of course depending on the p_T of the initial b-quark), particles from photon conversion or with an undefined origin usually bare a larger and wider

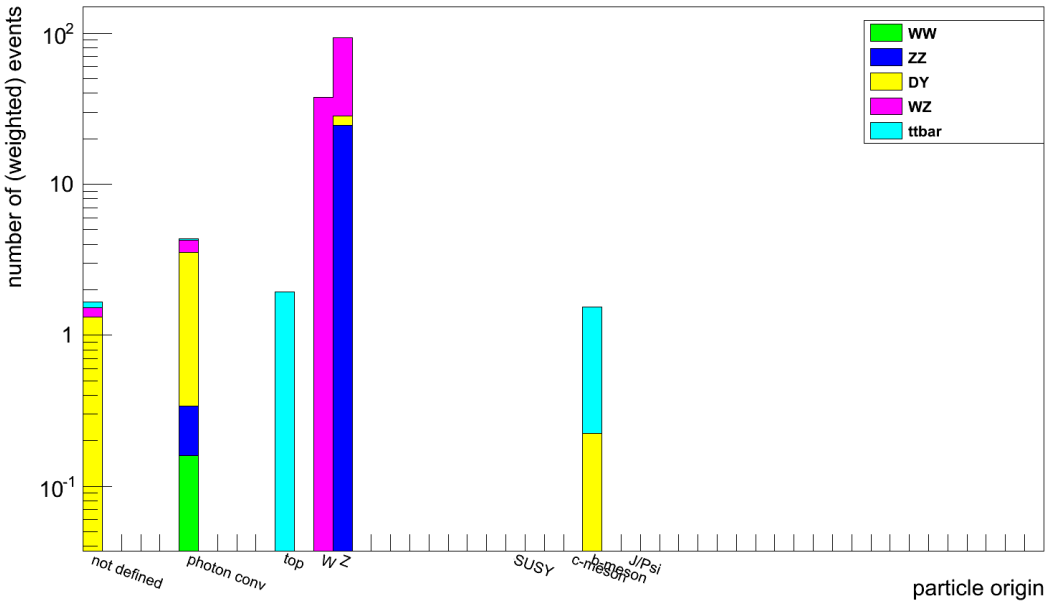

(a) electron origin

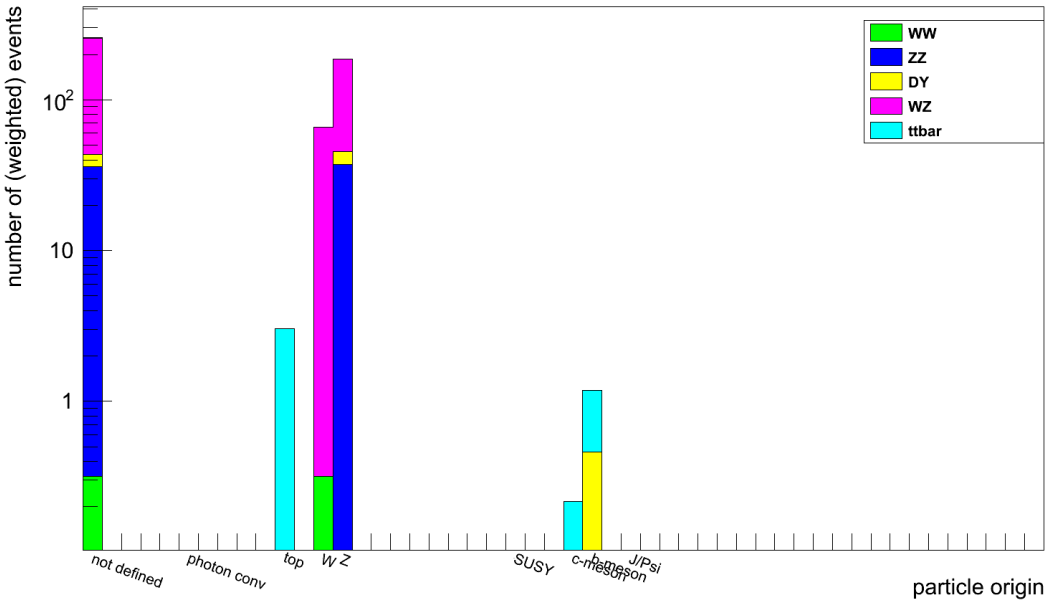

(b) muon origin

Figure 5.1: Origin of the particles in a trilepton event according to the MCTruthClassifier tool

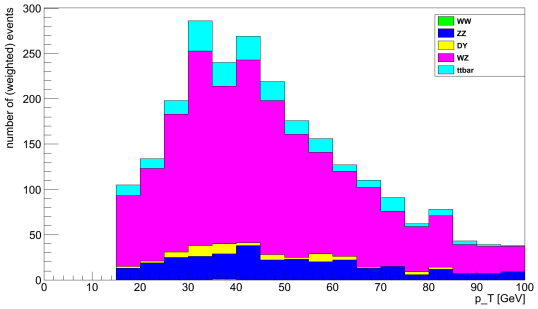

(a) not defined origin

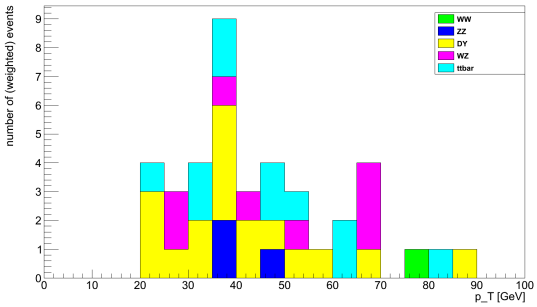

(b) photon conversion

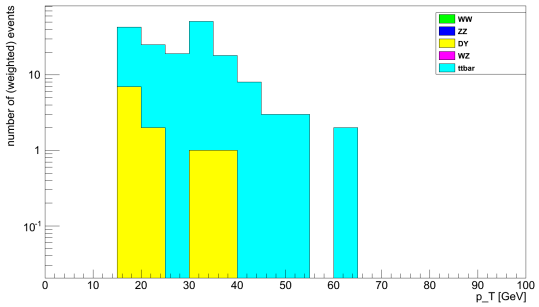

(c) b-meson (heavy flavour)

Figure 5.2: p_T-distribution of particles with different origin according to the MCTruthClassifier tool.

distributed p_T. The peak at around 30 GeV in the heavy flavour distribution arises from a p_T cut at 30 GeV for the leading leptons and will be discussed later.
As top quark pair production has a very "SUSY-like" signature, as pointed out in chapter 4.2, and is therefore an important background source, the behaviour of the fake trilepton events coming from $t\bar{t}$ is further investigated. The most significant difference between a trilepton event from SUSY and one from $t\bar{t}$ is the secondary lepton coming from the b-jet. This lepton source implies a high hadronic activity around the lepton since this will usually follow the direction of the formed jet. This also means a small distance measured in ΔR between lepton and jet, why the heavy flavour overlap removal is done for the object selection of muons. The hadronic activity shows itself in the isolation variable E_T^{cone}, which is also part of the object definition. Nevertheless, there is still the possibility for a secondary lepton to survive this selection. Figure 5.3 shows the dependence of this variable on the p_T of electrons and muons. As comparison, the distribution is shown for leptons that are tagged as "isolated" by the MCTruthClassifier tool and for leptons that do not fulfill this requirement. Isolated leptons come from the signal process, e.g. a top quark or a W or Z boson. Thus, all the other leptons come from heavy flavour decays, photon conversion, light jets or other processes that produce non-prompt leptons. One can clearly see that isolated leptons tend to have a small E_T^{cone} value over the whole p_T range. Non-isolated leptons on the other side have a higher E_T^{cone} value and low p_T, especially the muons. This information was used to make a tighter E_T^{cone} cut in the object selection for leptons with $p_T < 30$ GeV and will be used later in a data-driven method to estimate the fake contribution.

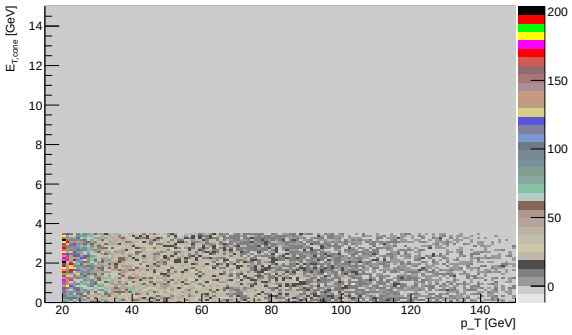

(a) non isolated electrons

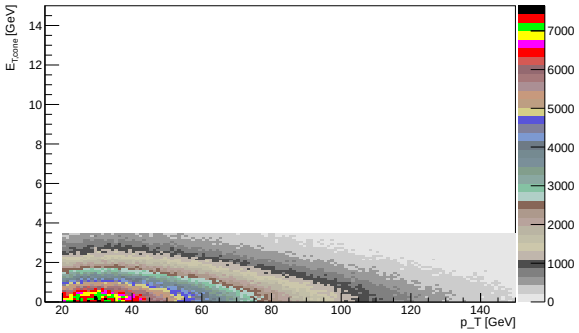

(b) isolated electrons

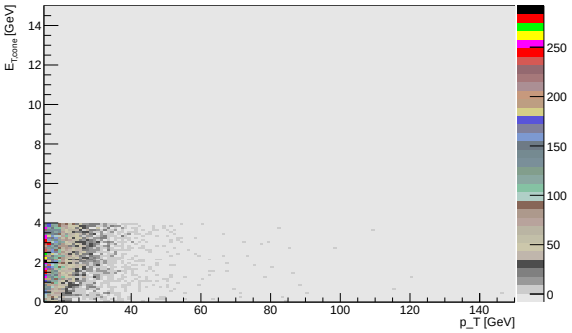

(c) nonisolated muons

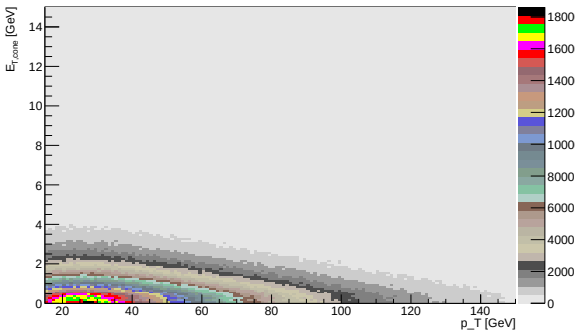

(d) isolated muons

Figure 5.3: Two-dimensional plots of E_T^{cone} vs. p_T of reconstructed leptons in the $t\bar{t}$ MC sample, where the reconstruction involves the object selection cuts for leptons. The distributions are shown for electrons and muons separately. The (non)isolated term refers to the corresponding notation in the MCTruthClassifier tool. Nonisolated leptons have a higher E_T^{cone} value because of nearby jets.

5.3 Cut and count analysis

This section covers the actual analysis which is optimized to search for supersymmetric events. Instead of taking a specific model, where assumptions on the SUSY breaking mechanisms have been made, a phenomenological model which was already used for other SUSY analysis (see figure 4.5 under Pheno-MSSM) is used to describe the signal process. As input parameters, masses of the squarks, the gluino and the lsp are used. $tan\beta$ is set to 4 and $\mu = 1.5 \cdot \{m_{gluino}, m_{squark}\}$. Other parameters of the grid can be looked up in [29]. This grid targets the production mechanism that is explained in chapter 4, so producing initially two gluinos/squarks or one squark and a gluino. Between the masses of the two lightest neutralinos, the masses of the sleptons are put to have an intermediate slepton state that has effect on the decay modes and cross sections. The masses of the different sparticles are set in the following way:
The masses of gluinos and squarks define a grid with values from 300 – 1100 GeV in steps of 100 GeV. An asymptotic grid point with a mass of 3000 GeV won't be considered in this analysis. To avoid the same masses of gluinos and squarks, one of the masses is always set 10 GeV higher than the mass of the other sparticle. Thus, instead of heaving one grid point for the combination 400-400, there are two points with the combination 410-400 and 400-410. The mass of the lsp, which is the lightest neutralino in this case, is either set fix to 100 GeV (light lsp) or 150 GeV below the mass of the gluino or squark (compressed mode). The second lightest neutralino is 100 GeV below this boundary for the first case and 50 GeV below it for the second case. For both cases, the slepton masses are exactly between the masses of these two neutralinos (see 5.4).
The squarks mentioned above only consider the first two generations, which are almost degenerate in mass and therefore define a general squark mass. Masses of third generation squarks are set to 3 GeV and play no role in the decay topology. Due to a mSUGRA-like mass scale behaviour ($\mu > M1 > M2$, where μ: Higgs parameter; $M1$: bino mass term; $M2$: wino mass term), the two heavy neutralinos and the heavier chargino (containing the higgsinos) have too high masses to be considered in this model. The lighter neutralinos and the light chargino contain the wino and bino and complete the model.
Figure 5.5 illustrates the masses of the particles defined in table 5.1. Figure 5.6 shows the comparison between the SM background and the SUSY signal for some variables. The SUSY signal has large E_T^{miss} compared to the SM background as one would expect it. Especially for the point from the light lsp mode, this is true. Due to the high mass differences in the light lsp mode, the decay particles have very high p_T and for the case of the lightest neutralino, this amount of p_T can then not be detected as it is the lsp. In the compressed mode, there is still high E_T^{miss} compared to the background, but the difference is not as much as for the light lsp. The number of jet distribution shows a clear peak in the 2 jet bin for the SUSY signal because of the gaugino production, whereas the background decreases to higher jet multiplicities. For the invariant mass distribution of the opposite sign, same flavour pair, the background peaks at the Z mass because of the WZ, ZZ and Z background. Although the SUSY signal can also contain a Z in the decay of the neutralino, no peak is visible for the chosen grid points. Again, the compressed mode shows a more background like behaviour except for the Z peak and the light lsp mode shows almost a flat distribution, that can also be explained by the mass differences. A similar behaviour is shown for the transverse momentum of the first electron and muon, where first means the lepton with the hightest p_T.

5.3.1 Cuts

Based on the Monte Carlo comparison of distributions and shapes for the SUSY signal s and SM background b, a $\frac{s}{\sqrt{b}}$ optimisation is performed for E_T^{miss} , the invariant mass of two leptons of the same flavour

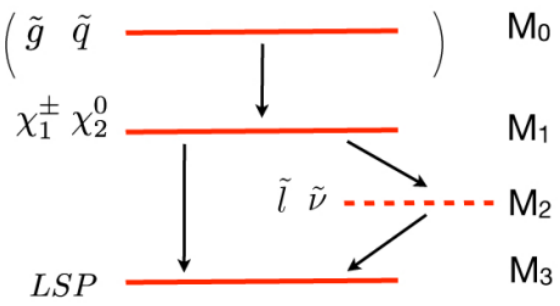

Figure 5.4: Sketch illustrating the mass scale for the different sparticles. [30] The mass scale parameters on the right side of the sketch are not the wino/bino mass terms mentioned before.

mode	compressed	light lsp
$m_{\chi_2^0}$	min{m_{gluino},m_{squark}} - 50 GeV	min{m_{gluino},m_{squark}} - 100 GeV
$m_{slepton}$	$(m_{\chi_1^0} + m_{\chi_2^0})/2$	$(m_{\chi_1^0} + m_{\chi_2^0})/2$
$m_{\chi_1^0}$	min{m_{gluino},m_{squark}} - 150 GeV	100 GeV

Table 5.1: Mass definitions of the neutralinos and sleptons for the phenomenological grid

and opposite charge, p_T of electrons and muons and the number of jets in an event. As it is not possible to optimise for each grid point of the SUSY signal, compromises have to be made and the optimisation is done with respect to the compressed mode, as it is harder to discriminate from the signal. The distributions of the optimisation can be seen in chapter B. Some cuts will distinguish between the different channels that are possible. By requiring an opposite sign, same flavour pair, the following channels can be observed: $e^+e^-e^\pm$, $e^+e^-\mu^\pm$, $\mu^+\mu^-e^\pm$ and $\mu^+\mu^-\mu^\pm$. Each channel will be investigated separately by the cuts.
Along with some quality requirements for an event, the following cuts are applied to each event[2]:

- **Trigger**: For data, the events have to fulfill the requirement of the following event filters according to their stream:
  - `EF_e20_medium` for electrons from data periods B2-J.
  - `EF_e22_medium` for electrons from data period K.
  - `EF_mu18` for muons from data periods B2-I.
  - `EF_mu18_medium` for muons from data periods J and K.

  The number in the event filter name tells at what p_T the trigger efficiency is increasing. Leptons used for the analysis have to fulfill a certain p_T requirement to be able to compare Monte Carlo and data events. Monte Carlo events have to be treated differently in order to consider the different data periods in a correct way with the WhichPeriod tool provided by the Top Working Group. If a MC event is assigned to period K of 2011 data, the `EF_22_medium` event filter is used, otherwise `EF_20_medium`. `EF_mu18` is used as trigger for muons in MC. Due to a problem with the muon trigger in the mc10b Monte Carlo samples [24] and a missing trigger variable in the available Top D3PDs, the trigger cut itself is not used for Monte Carlo. Instead, trigger efficiencies provided

[2]For the last cuts, abbreviations that will be used for cutflow plots or as reference to the cut will be put in parentheses

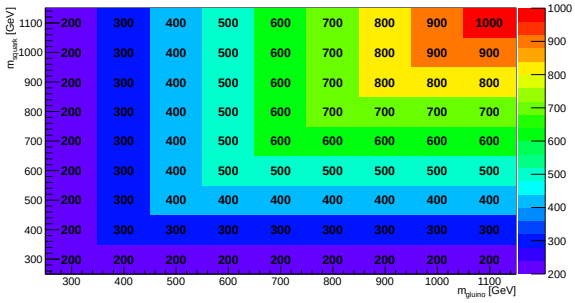

(a) $m_{\chi_2^0}$ in the light lsp mode

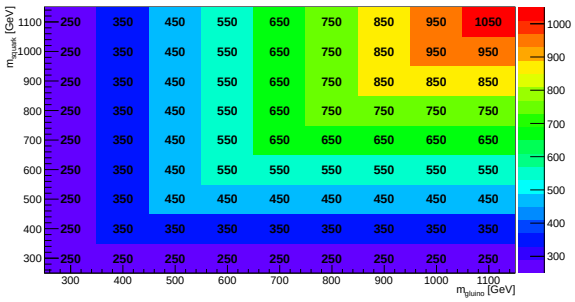

(b) $m_{\chi_2^0}$ in the compressed mode

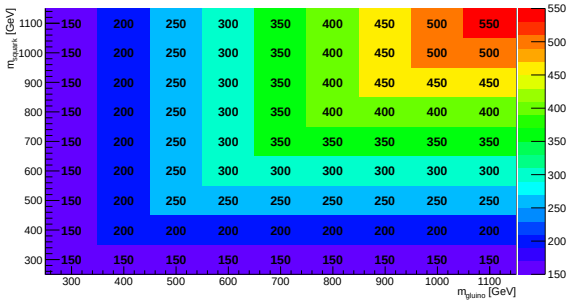

(c) $m_{slepton}$ in the light lsp mode

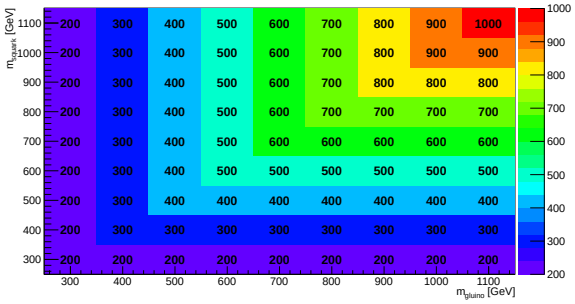

(d) $m_{slepton}$ in the compressed mode

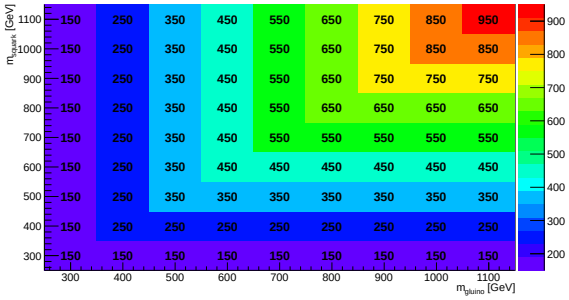

(e) $m_{\chi_1^0}$ in the compressed mode; the light lsp mode is not shown here, because the mass of the lightest neutralino is fix for this case

Figure 5.5: Illustration of the masses of the second lightest neutralino and the intermediate sleptons for the compressed and light lsp mode as they are described in table 5.1.

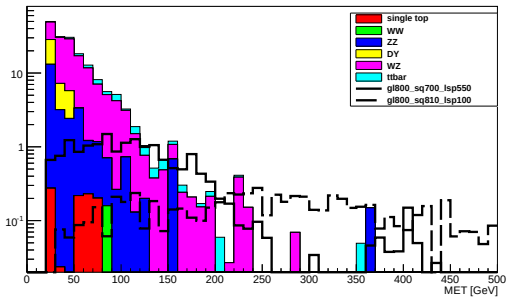

(a) E_T^{miss}

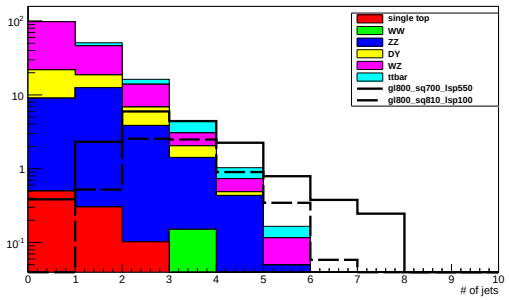

(b) Number of jets

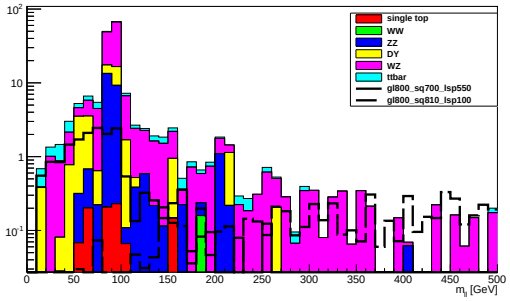

(c) Invariant mass of a lepton pair of the same flavour and opposite charge

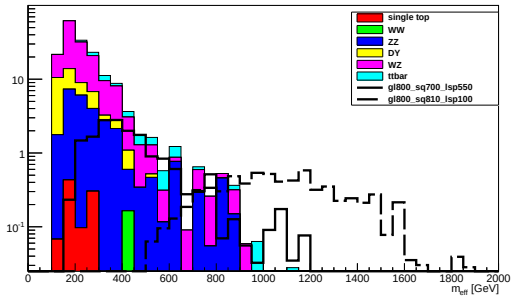

(d) Effective mass scale $m_{eff} = E_T^{miss} + \sum |\vec{p}_T|$

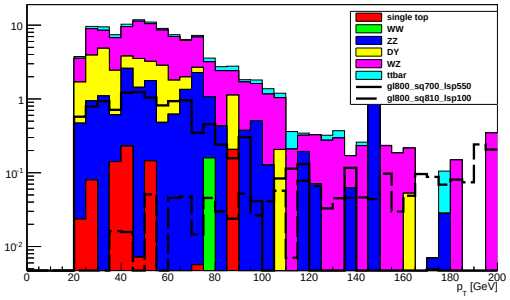

(e) p_T of the first (by p_T) electrons

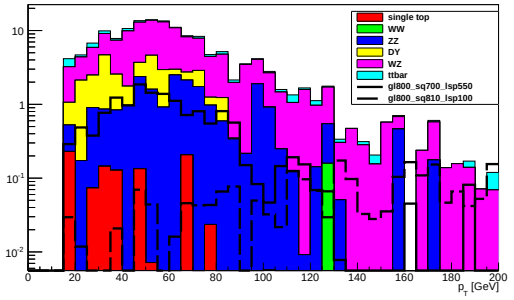

(f) p_T of the first muon

Figure 5.6: Comparison between SM background and two points from the SUSY grid after requiring three leptons; one grid point is taken from the light lsp mode and the other from the compressed mode. As one can see, trilepton events coming from SUSY have large E_T^{miss} and many associated jets, which is not the case for the SM background. For the invariant mass of two leptons of the same flavour and opposite charge, a clear peak can be seen for the SM background.

by [24] are used.
To avoid doublecounting of events in the four different channels $e^+e^-e^\pm$, $e^+e^-\mu^\pm$, $\mu^+\mu^-e^\pm$ and $\mu^+\mu^-\mu^\pm$, the trigger conditions are used. The muon trigger is used for the $\mu^+\mu^-e^\pm$ and $\mu^+\mu^-\mu^\pm$ channels or for the $e^+e^-\mu^\pm$channel, if the electron trigger did not fire. Similarly for the electron trigger, that is used for $e^+e^-e^\pm$ and $e^+e^-\mu^\pm$ channels or for $\mu^+\mu^-e^\pm$, if the muon trigger did not fire.

- **Cleaning of bad jets**: Requirements on the jets to throw away events with bad jets according to the Top Working Group.
- **Vertex event cut**: More than four tracks from the primary vertex.
- **At least 2 leptons**:
  $e^+e^-e^\pm$: At least two electrons and no muon.
  $e^+e^-\mu^\pm$: At least two electrons.
  $\mu^+\mu^-e^\pm$: At least two muons.
  $\mu^+\mu^-\mu^\pm$: At least two muons and no electron.
- **First E_T^{miss} cut**: This cut can be seen as an auxiliary cut. The low E_T^{miss} region showed some discrepancy between data and MC, therefore $E_T^{\text{miss}} > 20$ GeV is required.
- **Exactly three leptons**:
  $e^+e^-e^\pm$: Exactly three electrons and no muon.
  $e^+e^-\mu^\pm$: Excactly two electrons and one muon.
  $\mu^+\mu^-e^\pm$: Exactly two muons and one electron.
  $\mu^+\mu^-\mu^\pm$: Exactly three muons and no electron.
  After this cut, the four channels can be distinguished without any overlap of two channels.
- **Trigger matching**: Not applied in MC or for the muon stream in data because of the bug mentioned in the trigger cut explanation. For electrons in data, the electrons are matched to the object that passed the trigger requirement. At least one electron has to fulfill this requirement.
- **Lepton p_T requirement**:
  - $e_{1,p_T} > 30$ GeV, $e_{2,p_T} > 25$ GeV, $e_{3,p_T} > 20$ GeV.
  - $\mu_{1,p_T} > 25$ GeV, $\mu_{2,p_T} > 25$ GeV, $\mu_{3,p_T} > 15$ GeV.

  Cutflows and some distributions will just be shown after this cut where I will refer to it as leptonp_T cut (stage). The Monte Carlo trigger require at least one electron with a $p_T > 25$ GeV and one muon with $p_T > 20$ GeV. Therefore the comparison between Monte Carlo and data makes sense just after this cut.
- **Opposite sign, same flavour (OSSF) pair**: At least one pair of the same lepton flavour and opposite charge is required because of the neutralino decay topology. (OS2L)
- **Minimum ΔR between each lepton pair**: Events with leptons that are closer in ΔR to each other than 0.2 are removed. Trilepton events coming from Z+jets with photon conversion as third lepton origin showed such a behaviour. (deltaR)
- **Lower bound on invariant mass of an OSSF pair**: To avoid having leptons from low resonances or photon decay, at least one OSSF pair has to fulfill $m_{l^+l^-} > 15$ GeV. (mll)
- **Second E_T^{miss} cut**: Events not having $E_T^{\text{miss}} > 50$ GeV are removed. (cutmetandht)

- **Z veto**: Another cut on the invariant mass of an OSSF pair. Events with an OSSF pair that has an invariant mass of 91 ± 10 GeV are cut. (Zveto)
- **At least 2 jets**: The event has to contain at least 2 jets. (atleast2Js)

Table 5.2 shows the cutflow for the Monte Carlo samples of the complete Standard Model background and two chosen grid points from the SUSY model. Events are scaled to an integrated luminosity of 2.05 fb^{-1}. Cuts that cause a significant change in the number of background events are the second E_T^{miss} cut, the Z veto and atleast2Js cut. One can also see the differences between light lsp and compressed mode. The light lsp mode has cut efficiencies of more than 90 % throughout the cutflow, whereas the example point for the compressed mode has a cut efficiency of 61.6 % for the Z veto. Figure 5.7 shows the number of events one would expect after all cuts for the SUSY signal in a data sample of 2.05 fb^{-1}. Missing grid points correspond to missing Monte Carlo samples, where some problems occured for their production, and will be shown for other figures of the SUSY grid as well. For points with $m_{gluino} > m_{squark}$, much more events are expected than for the reverse case. This is due to the high gluino production cross section and the possibility for gluinos to decay to squarks. As one would further expect from the distributions and the cut efficiencies, the yield for the light lsp mode is higher than for the compressed mode.

	800_700_550		800_810_100		SM bkg	
cut	# of evts.	cut eff. [%]	# of evts.	cut eff. [%]	# of evts.	cut eff. [%]
without cuts	127.88	-	44.89	-	31465232	-
3 leps	18.25	14.27	7.05	15.71	166.22	$5 \cdot 10^{-6}$
lepton p_T	16.82	92.1	6.95	98.7	155.73	93.7
OS2L	16.78	99.8	6.91	99.3	152.91	98.2
ΔR	16.78	100.0	6.89	99.8	141.56	92.6
m_{ll}	16.63	99.1	6.89	100.0	141.18	99.7
E_T^{miss}	13.98	84.1	6.75	97.9	51.64	36.6
Z veto	8.61	61.6	6.71	99.4	6.29	12.2
> 2 jets	7.39	85.8	6.19	92.2	1.59	25.3

Table 5.2: Cutflow comparison of SM background and SUSY signal based on the cuts defined in chapter 5.3.1 using Monte Carlo Samples. Estimates from Monte Carlo are scaled to an integrated luminosity of 2.05 fb^{-1} including the statistical uncertainty. The cutflow is shown for the combination of all four channels. The numbers of the SUSY samples are defined in the following way: $m_{gluino}\_m_{squark}\_m_{lsp}$

5.4 Monte Carlo and data comparison

The cut and count analysis is performed with data taken in year 2011 for the periods B - K (table 5.3). After applying the good rund list provided by the top working group [31], 2052.49 pb^{-1} of good data remain for the analysis.
Applying the cuts to Monte Carlo and the amount of good data, the cutflow shown in figure 5.8 is maintained. After each cut stage, the expected number of events in data and MC is compared. For data, the error bars are ”poissonized” to get uncertainties corresponding to one standard deviation. For all cut stages, data and MC agree with each other with less than two standard deviations. The main background contributions come from WZ and $t\bar{t}$. The ZZ background is almost completely lost after the Z veto, whereas the DY background already dies out after the second E_T^{miss} cut. Since DY is a background containing fakes, there could be the possibility that it is not well modeled in MC and there

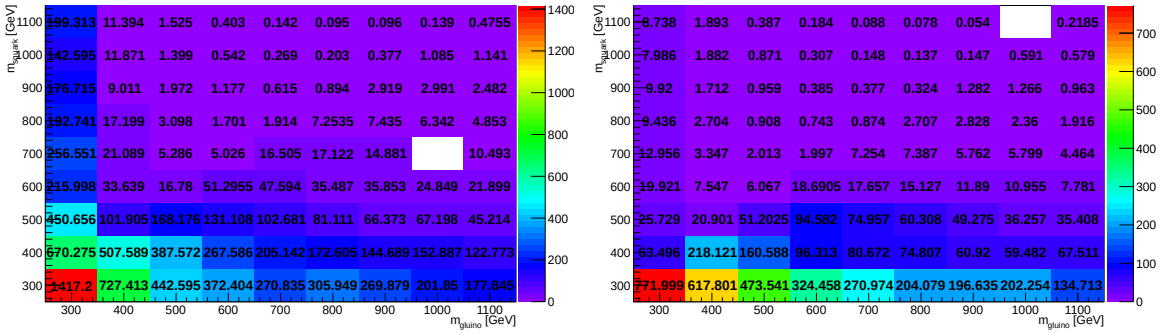

(a) light lsp mode

(b) compressed mode

Figure 5.7: Number of events passing all cuts scaled to an integrated luminosity of 2.05 fb^{-1}. For the diagonal, where two grid points are put very close to each other (m_{gluino} + 10 GeV,m_{squark} and m_{gluino},m_{squark} + 10 GeV), the arithmetic mean of both points is taken. White spaces indicate missing MC samples for the corresponding grid point.

might be a contribution of it after this cut. On the other hand, such an event would also have to pass the last cut requiring at least two jets, which is also not very DY-like. So it can be completely neglected for the event yield after all cuts. For each channel separately and the sum of all channels, the number of expected events from background MC and from data after the last cut is listed in table 5.4.

period	runs	rec. int. Lumi. [pb^{-1}]	peak Lumi. [$\frac{1}{cm^2 s}$]
B	177986 - 178109	16.986	$2.44 \cdot 10^{32}$
D	17910 - 180481	179.214	$6.65 \cdot 10^{32}$
E	180614 - 180776	50.245	$8.37 \cdot 10^{32}$
F	182013 - 182519	152.320	$1.11 \cdot 10^{33}$
G	182726 - 183462	561.254	$1.27 \cdot 10^{33}$
H	183544 - 184169	278.516	$1.27 \cdot 10^{33}$
I	185353 - 186493	399.722	$1.90 \cdot 10^{33}$
J	186516 - 186755	233.017	$2.02 \cdot 10^{33}$
K	186873 - 187815	660.541	$2.33 \cdot 10^{33}$
total data		2531.784	

Table 5.3: Amount of data taken in the periods that are used for this analysis [32]

5.5 Systematic uncertainties

Not all input parameters and properties in this analysis are exactly known. Therefore, studies have to be included to estimate the systematic uncertainties of those. The different changes of the parameter's values for the systematic study follow the ATLAS top reconstruction group recommendations [33]. The estimation of the different uncertainties is always the same. Uncertainties on the different input parameters are applied (either added or multiplied) and all the available MC samples analysed with this changed object definition. Afterwards, the number of events surviving the whole MC analysis is compared to the number of events one obtains without variation of the input parameters (nominal sample).

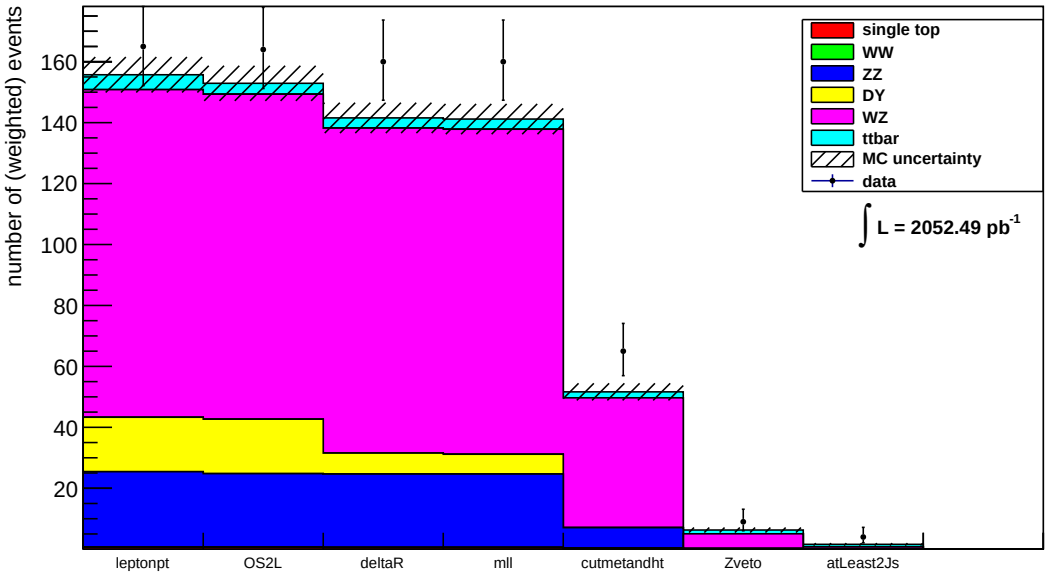

Figure 5.8: Cutflow comparison of MC and data corresponding to an integrated luminosity of 2fb^{-1}.

process	$e^+e^-e^\pm$	$e^+e^-\mu^\pm$	$\mu^+\mu^-e^\pm$	$\mu^+\mu^-\mu^\pm$	all
single top	- 0.01	-	-	-	-0.01
WW	-	-	0.16	-	0.16
ZZ	-	0.01	-	-	0.01
DY+jets	-	-	-	-	-
WZ	0.14	0.16	0.06	0.29	0.64
$t\bar{t}$	0.02	0.44	0.18	0.16	0.80
800_700_550	0.93	1.56	2.88	2.03	7.39
800_700_100	1.70	1.71	1.52	1.26	6.19
total bkg	0.15 ± 0.10	0.61 ± 0.22	0.39 ± 0.20	0.44 ± 0.20	1.59 ± 0.39
data [2.05 fb^{-1}]	1 ± 1	1 ± 1	0	2 ± 1.41	4 ± 2

Table 5.4: Event comparison of background, signal (using Monte Carlo Samples) and data after the last cut (at least 2 jets). Estimates from Monte Carlo are scaled to an integrated luminosity of 2.05 fb^{-1}. The cutflow is shown for the four channels independently and for the combination of all channels. Statistical uncertainties are only quoted for the total background and the measurement from data, where the Poisson error is applied.

run number	event number	channel	lepton 1 p_T [GeV]	lepton 2 p_T [GeV]	lepton 3 p_T [GeV]
186399	12454697	$e^+e^-\mu^\pm$	85.11	31.85	19.05
184022	103742121	$e^+e^-e^\pm$	90.45	43.08	23.77
180400	107867460	$\mu^+\mu^-\mu^\pm$	52.68	44.53	19.17
182747	22756789	$\mu^+\mu^-\mu^\pm$	74.52	50.78	39.98
	E_T^{miss} [GeV]	# of jets	m_{ll1} [GeV]	m_{ll2} [GeV]	
	104.7	2	103.6	-	
	53.50	4	107.6	56.12	
	50.15	2	73.97	45.59	
	73.17	2	124.2	22.04	

Table 5.5: Events details for the data events that survived all cuts in data corresponding to an integrated luminosity of 2.05 fb^{-1}

The difference between both is treated as absolute systematic uncertainty. To get the relative systematic uncertainty, the absolute value is normalized by the number of events of the nominal sample.
jet systematics: The uncertainties concerning the jet energy scale are maintained by the usage of the `JESUncertaintyProvider` [34] which provides uncertainties on the jet energies for jets up to $\eta = 4.5$. The jet reconstruction efficiency (JRE) is obtained by matching jets reconstructed from jets to calorimeter based jets [35]. To get the uncertainty, jets from the event are randomly dropped and the efficiency calculated again. The difference will be taken as symmetric systematic uncertainty. The jet energy resolution and its uncertainty is provided again by the ATLAS top group [26]. The reconstructed transverse momentum of the jet is smeared by a Gaussian with a width of $\sqrt{(\sigma + \sigma_{uncert.})^2 - \sigma^2}$, where σ is the initial resolution and $\sigma_{uncert.}$ its uncertainty.
electron systematics: The ATLAS top group also provides uncertainties of the trigger SF, reconstruction efficiency and identification SF which are applied to the electron object definition [24]. For the systematics of the electron energy scale and resolution, the `EnergyRescaler` tool is provided.
muon systematics: The systematics for muons are quite similar as for electrons. Trigger SF, top-ID efficiency SF and reconstruction efficiency SF are varied to obtain the systematics. The uncertainties on the muon momentum scale and resolution are obtained. by the `SmearingClass` tool.
E_T^{miss} **systematics**: Every systematic for a reconstructed object has an effect on the E_T^{miss} distribution because the E_T^{miss} is calculated by them. But there are also systematics that only affect the E_T^{miss} . Every remaining energy in the calorimeter that is not associated to an object like an electron or muon is part of the so called Cell out term and is varied to get the systematic uncertainty. The effect of pileup on the E_T^{miss} is considered by applying a flat uncertainty of 10 % on it, using the `Top_Met_Tool` [36].
$t\bar{t}$ **systematics**: For the $t\bar{t}$ process exist additional systematics uncertainties. MC samples including initial and final state radiation (ISR and FSR) have to be compared to the nominal MC sample (ACER + pythia in this case) of the $t\bar{t}$ process. The difference in the number of events after the whole cutflow is taken as additional systematic uncertainty. Another systematic considers different MC generator for this process. MC@NLO and POWHEG are compared and the difference taken as symmetric systematic uncertainty. Differences in the parton shower and fragmentation model can be investigated by evaluating the difference for $t\bar{t}$ between PowHeg + Pythia vs. Herwig. Further details to the procedures can be found in [33].

The systematic uncertainties for the two largest background, $t\bar{t}$ and WZ, as well as the systematic uncertainty for the total background is given in table 5.6. To get the total systematic uncertainty, the single

uncertainties are summed quadratically, so no correlation between systematics were taken into account. For WZ, the $e^+e^-e^\pm$channel was not considered by obtaining the systematic uncertainty by the variation of the parameters. This channel gave unreasonable results for every systematic leading to a large negative systematic uncertainty (for both up and down variation) that cancelled all positive systematic uncertainties of e.g. the $t\bar{t}$ process. The result was a small positive systematic uncertainty compared to the negative one. Without including the $e^+e^-e^\pm$channel, the results for the systematics are more reasonable.
Applying the systematic uncertainty of table 5.6 to the event expectation from Monte Carlo by adding it quadratically to the statistical uncertainty, the estimated trilepton background becomes $1.59^{+0.89}_{-0.92}$.

systematic	$t\bar{t}$	WZ	tot. bkg.
JES	+8.5/−8.5	+13.5/−0.0	+11.0/−6.3
JRE	+15.2/−15.2	+37./−37.0	+27.1/−27.1
el ID SF	+6.8/−6.6	+10.4/−9.8	+7.9/−8.2
mu ID SF	+1.0/−1.0	+1.3/−1.3	+1.1/−1.1
el ES	+3.9/−0.6	+0.0/−0.0	+2.9/−0.4
el ER	+0.0/−6.8	+0.0/−0.0	+0.0/−4.2
MET Cell	+0.0/−0.0	+0.0/−24.4	+0.0/−16.3
ISR+FSR	+38.2/−34.7	-	28.4+/−25.9
MC gen.	+41.3/−41.3	-	+30.7/−30.7
tot. syst. uncert.	+59.4/−57.07	+40.7/−45.1	+50.2./−52.2

Table 5.6: Systematic uncertainties given in % for the SM background for the two largest background processes and the total background. Systematics that don't contribute are not listed; ID: identification; ES; energy scale; ER: energy resolution

Chapter 6

Matrix Method

Monte Carlo simulations are an important tool to study background processes or to verify/falsify physics hypotheses from theory. Nevertheless, one can not be sure that the known physics is simulated well enough for the whole event and not only for the hard scattering of a process. Side effects like misreconstruction of objects, mismodelling of some detector parts or the production of secondary particles are often not well understood and can affect properties like E_T^{miss} in a significant way. But even important physics like the hadronisation of quarks is very difficult to model in a correct way. Therefore one does not want to rely only on Monte Carlo simulation but rather tries to extract the necessary information directly from data. One way to estimate the fake contribution from data is the so called Matrix Method which is already used in ATLAS analyses like the top quark pair production [37], on which this study will be based on.

6.1 The Matrix Method

Reconstructed objects like electrons and muons have to fulfill a set of criteria to be considered as this object and to be kept for analysis. These requirements are set in a way that most of the fake or "bad" [1] objects are rejected while the efficiency for reconstructing a real object is still high. Of course, this procedure can not give a reconstruction efficiency of 100 % for real objects and 0 % for all the fake ones. Thus there is some small overlap of real and fake leptons in the final selection and trilepton events can also be mimicked by $t\bar{t}$ and Z+jets events which do not have three leptons from its original process. In the matrix method, the object definition is loosened in a way such that the fraction of fake objects increases compared to real objects. This leads to two different object definitions called "loose" and "tight", where the tight definition is the same as used for the objects in the cut-and-count analysis. Then the efficiency for a loose lepton (L) to be reconstructed as tight (T) [2] is measured in a real and in a fake lepton enhanced region in data[3]. Knowing the rate for a loose fake lepton to be reconstructed as tight (f; fake rate) and the similar expression for real leptons (r; real efficiency), one is able to calculate the number of events with real and fake leptons from the events selected in the analysis by the loose and tight definition (see equation 6.3). N_{TTT} denotes events with three tight leptons [4], N_{RRR} events with three real leptons and so on. The real efficiencies r_i and the fake rates f_i refer to the i-th lepton, where the leptons are ordered from highest to lowest p_T. The real and fake events are marked with an l, because these events can also contain loose leptons that do not survive the tight selection, whereas the wanted number of events for the fake estimation only contains tight leptons. Since we can just measure events according to tight and loose leptons, the matrix in equation (6.3) has to be inverted and multiplied with the left-hand-side. To get the number of events with fakes that satisfy the tight selection, all events with

[1] the "fake" expression will again be used for fake and secondary leptons in the same way
[2] the tight selection here is a subsample of the loose selection
[3] It can also be done in Monte Carlo to test it since only reconstructed objects are involved
[4] tight and loose leptons are now distinguished

at least one fake lepton F have to be summed and multiplied with the corresponding fake rates and real efficiencies:

$$N_{fakes} = r_1 r_2 f_3 N_{RRF} + r_1 f_2 r_3 N_{RFR} + f_1 r_2 r_3 N_{FRR} + r_1 f_2 f_3 N_{RFF} + f_1 r_2 f_3 N_{FRF} + f_1 f_2 r_3 N_{FFR} + f_1 f_2 f_3 N_{FFF} \tag{6.1}$$

The matrix method requires the input of the real efficiencies and fake rates for each selected lepton. Since the real efficiencies should not depend on the performed analysis, they are mostly taken from [37]. In contrast to the real efficiencies, the fake rates can differ significantly depending on the signal region one looks at, therefore they are measured in a fake lepton enriched region using the following cuts that also base on the selection in [37]:

- exactly one lepton fulfilling the loose requirement
- at least one jet
- $\Delta R(leading\,jet, lepton) > 0.7$
- $5 < E_T^{miss} < 20GeV$

Loose muons do not require any isolation cuts compared to tight muons, i.e. no requirement on p_T^{cone} or E_T^{cone}. Loose electrons have to satisfy medium electron requirements, one b-layer hit, no conversion match (accordding to isEM) and $E_{T,cone} < 6$ GeV.
Using these definitions and cuts, the fake rates can be measured by

$$f = \frac{N_T^{data} - N_T^{MC}}{N_L^{data} - N_L^{MC}}. \tag{6.2}$$

The measured events in data have to be subtracted by the events in Monte Carlo to account for real lepton contamination in the sample.
Equation (6.2) reflects just the basic measurement. Since the rates depend on kinematic variables like the transverse momentum or the pseudorapidity of the lepton, this calculation has to be done for every bin in the 2-dimensional space spanned by the p_T and η of the leptons. Another fact that could be taken into account is the composition of the different fake sources, i.e. leptons from light flavor jets, heavy flavor jets and from photon conversion[5]. However, the Monte Carlo analysis in chapter 5.4 showed, that the main process that contributes to trilepton events from photon conversion, namely DY + jets, dies out after the second E_T^{miss} cut. Even though Monte Carlo does not have to be correct and we actually want to measure fakes from data, a possible contribution from DY+ jets and a lepton from photon conversion after requiring high E_T^{miss} and at least jets seems to be negligible. The same is valid for photon conversion from diboson or $t\bar{t}$ production. So the fake estimation here targets fakes from light and heavy flavour jets that predominantly come from $t\bar{t}$.

[5] photon conversion would be only considered for elecrons, because it's unlikely to produce a muon pair

$$
\begin{pmatrix} N_{TTT} \\ N_{TTL} \\ N_{TLT} \\ N_{LTT} \\ N_{TLL} \\ N_{LTL} \\ N_{LLT} \\ N_{LLL} \end{pmatrix} =
\begin{pmatrix}
r_1r_2r_3 & r_1r_2f_3 & r_1f_2r_3 & f_1r_2r_3 & r_1f_2f_3 & f_1r_2f_3 & f_1f_2r_3 & f_1f_2f_3 \\
r_1r_2(1-r_3) & r_1r_2(1-f_3) & r_1f_2(1-r_3) & f_1r_2(1-r_3) & r_1f_2(1-f_3) & f_1r_2(1-f_3) & f_1f_2(1-r_3) & f_1f_2(1-f_3) \\
r_1(1-r_2)r_3 & r_1(1-r_2)f_3 & r_1(1-f_2)r_3 & f_1(1-r_2)r_3 & r_1(1-f_2)f_3 & f_1(1-r_2)f_3 & f_1(1-f_2)r_3 & f_1(1-f_2)f_3 \\
(1-r_1)r_2r_3 & (1-r_1)r_2f_3 & (1-r_1)f_2r_3 & (1-f_1)r_2r_3 & (1-r_1)f_2f_3 & (1-f_1)r_2f_3 & (1-f_1)f_2r_3 & (1-f_1)f_2f_3 \\
r_1(1-r_2)(1-r_3) & r_1(1-r_2)(1-f_3) & r_1(1-f_2)(1-r_3) & f_1(1-r_2)(1-r_3) & r_1(1-f_2)(1-f_3) & f_1(1-r_2)(1-f_3) & f_1(1-f_2)(1-r_3) & f_1(1-f_2)(1-f_3) \\
(1-r_1)r_2(1-r_3) & (1-r_1)r_2(1-f_3) & (1-r_1)f_2(1-r_3) & (1-f_1)r_2(1-r_3) & (1-r_1)f_2(1-f_3) & (1-f_1)r_2(1-f_3) & (1-f_1)f_2(1-r_3) & (1-f_1)f_2(1-f_3) \\
(1-r_1)(1-r_2)r_3 & (1-r_1)(1-r_2)f_3 & (1-r_1)(1-f_2)r_3 & (1-f_1)(1-r_2)r_3 & (1-r_1)(1-f_2)f_3 & (1-f_1)(1-r_2)f_3 & (1-f_1)(1-f_2)r_3 & (1-f_1)(1-f_2)f_3 \\
(1-r_1)(1-r_2)(1-r_3) & (1-r_1)(1-r_2)(1-r_3) & (1-r_1)(1-r_2)(1-r_3) & (1-r_1)(1-r_2)(1-r_3) & (1-r_1)(1-r_2)(1-r_3) & (1-r_1)(1-r_2)(1-r_3) & (1-r_1)(1-r_2)(1-r_3) & (1-r_1)(1-r_2)(1-r_3)
\end{pmatrix}
\begin{pmatrix} N^l_{RRR} \\ N^l_{RRF} \\ N^l_{RFR} \\ N^l_{FRR} \\ N^l_{RFF} \\ N^l_{FRF} \\ N^l_{FFR} \\ N^l_{FFF} \end{pmatrix} \tag{6.3}
$$

A first look at data showed slight differences in the fake rates of events that contain a b-tagged jet and those that do not. Hence, the fake rates will be measured for events with and without b-tagged jets. The b-tagging algorithm used for the fake rate measurement is the IP3D+SV1 at a working point of 60 % corresponding to a b-tag weight of 4.5 for this algorithm [38]. A low working point is used to keep the number of falsely b-tagged jets low. Later for the usage of the matrix method to get the fake yield, a working point of 80 % corresponding to a b-tag weight of -0.85 is used (corresponds to a probability of correctly tagging a b-jet to 0.8).

Since the definition of loose and tight leptons changes compared to [37] for leptons with $p_T < 30$ GeV, the real efficiencies of these leptons have to be measured in a real lepton enhanced region. An appropriate region is where two leptons of the same flavour and opposite charge have an invariant mass of ±5 GeV and the event satisfies $E_T^{\text{miss}} < 20$ GeV. These leptons then probably come from the Z decay to two leptons, because this process dominates this region due to its high cross section. Other than the real efficiency measurement in [37], no tag-and-probe method is used for simplicity reasons. To account for that, the low p_T real efficiencies are scaled by a factor, that is determined in a region, where the numbers of [37] and this method should agree. Otherwise, the number of loose leptons, that don't satisfy the tight criteria, would be too high and the real efficiencies therefore too small.

6.2 Validation with Monte Carlo samples

Before the matrix method is applied to real data, its functionality should be first studied with Monte Carlo samples to see that it works properly[6]. Without having real data, the definition of the fake and real lepton enhanced regions will slightly change. For this purpose, the fake rates are determined in the $t\bar{t}$ MC sample and real efficiencies are measured in the sample for Z+jets. The results can be found in tables 6.1 and 6.2. Although Monte Carlo samples are used for the MC real efficiencies, the same procedure is applied as for real data (see chapter 6.1). The fake rates from Monte Carlo have to be determined in a different way, because of too small statistics after the whole cutflow and possible contamination from real leptons. The MCTruthClassifier is used again to get the leptons not coming from W decay in the $t\bar{t}$ sample. Every lepton, that does not overlap with an isolated lepton of the same flavour within $\Delta R < 0.4$, is taken for the analysis. Since this also includes a big amount of electrons coming from photon conversion, no electrons, that are tagged as background electrons according to the MCTruthClassifier, are taken for the fake measurement. In the end, there should only be fake leptons from light and heavy flavour jets.
After having measured MC fake rates and real efficiencies, the normal analysis defined in chapter 5 is then run on the MC samples itself with the loose lepton selection. Every event surviving the cut with the p_T requirements for three leptons is used as input for the matrix. The outcome of 6.1 is then used as weight to the event.
In figure 6.1 the fake rate dependence on the kinematic variables p_T and η is shown. For both electrons and muons the fake rates decrease with increasing p_T. That means, higher p_T leptons coming from a light or heavy flavour jet have a small probability to satisfy the tight criteria. A reason might be, that the leptons come from hadrons with high p_T and are boosted into the direction of the corresponding jet. Another reason could be a larger jet cone for jets with higher p_T and therefore more hadronic activity in the calorimeter around the lepton. The kink at 30 GeV comes from the change in the tight E_T^{cone} requirement for leptons below and above 30 GeV. For very high p_T of above 70 GeV, the fake rates seem to be stable or even increase a little bit. Due to low statistics, a clear trend is not visible. The

[6] Later this will be referred to as closure test

structure in the η distributions is mainly caused by the detector's transition region beween barrel and end-caps, but seems to have a different effect on electron and muon reconstruction.

electrons					
p_T [GeV]; η	$-2.5 \rightarrow -2.0$	$-2.0 \rightarrow -1.5$	$-1.5 \rightarrow -1.0$	$-1.0 \rightarrow -0.5$	$-0.5 \rightarrow -0.0$
$20 \rightarrow 25$	0.17±0.02	0.09±0.01	0.10±0.01	0.17±0.01	0.17±0.01
$25 \rightarrow 30$	0.11±0.02	0.08±0.01	0.06±0.01	0.09±0.01	0.12±0.01
$30 \rightarrow 40$	0.22±0.03	0.16±0.02	0.19±0.01	0.24±0.02	0.26±0.02
$40 \rightarrow 50$	0.26±0.05	0.10±0.02	0.08±0.01	0.12±0.02	0.10±0.02
$50 \rightarrow 70$	0.22±0.05	0.06±0.01	0.05±0.01	0.07±0.01	0.08±0.01
$70 \rightarrow \infty$	0.09±0.04	0.09±0.03	0.04±0.01	0.07±0.01	0.06±0.01
p_T [GeV]; η	$0.0 \rightarrow 0.5$	$0.5 \rightarrow 1.0$	$1.0 \rightarrow 1.5$	$1.5 \rightarrow 2.0$	$2.0 \rightarrow 2.5$
$20 \rightarrow 25$	0.18±0.01	0.17±0.01	0.10±0.01	0.10±0.01	0.14±0.02
$25 \rightarrow 30$	0.14±0.01	0.11±0.01	0.06±0.01	0.07±0.01	0.13±0.02
$30 \rightarrow 40$	0.26±0.02	0.25±0.02	0.13±0.01	0.21±0.02	0.21±0.03
$40 \rightarrow 50$	0.10±0.02	0.15±0.02	0.10±0.01	0.12±0.02	0.19±0.04
$50 \rightarrow 70$	0.07±0.01	0.07±0.01	0.06±0.01	0.08±0.02	0.17±0.04
$70 \rightarrow \infty$	0.08±0.01	0.05±0.01	0.02±0.01	0.07±0.02	0.10±0.04
muons					
p_T [GeV]; η	$-2.5 \rightarrow -2.0$	$-2.0 \rightarrow -1.5$	$-1.5 \rightarrow -1.0$	$-1.0 \rightarrow -0.5$	$-0.5 \rightarrow -0.0$
$20 \rightarrow 25$	0.07±0.01	0.09±0.01	0.09±0.01	0.07±0.01	0.07±0.01
$25 \rightarrow 30$	0.04±0.01	0.05±0.01	0.07±0.01	0.04±0.01	0.04±0.01
$30 \rightarrow 40$	0.02±0.01	0.04±0.01	0.05±0.01	0.03±0.01	0.03±0.01
$40 \rightarrow 50$	0.03±0.01	0.08±0.01	0.11±0.01	0.08±0.01	0.09±0.01
$50 \rightarrow 70$	0.01±0.01	0.07±0.03	0.06±0.02	0.06±0.02	0.06±0.02
$70 \rightarrow \infty$	0.08±0.05	0.16±0.06	0.15±0.06	0.16±0.05	0.08±0.03
p_T [GeV]; η	$0.0 \rightarrow 0.5$	$0.5 \rightarrow 1.0$	$1.0 \rightarrow 1.5$	$1.5 \rightarrow 2.0$	$2.0 \rightarrow 2.5$
$20 \rightarrow 25$	0.06±0.01	0.07±0.01	0.10±0.01	0.10±0.01	0.07±0.01
$25 \rightarrow 30$	0.04±0.01	0.04±0.04	0.06±0.01	0.05±0.01	0.03±0.01
$30 \rightarrow 40$	0.03±0.01	0.03±0.01	0.03±0.01	0.02±0.01	0.02±0.01
$40 \rightarrow 50$	0.07±0.01	0.09±0.01	0.10±0.01	0.09±0.01	0.05±0.01
$50 \rightarrow 70$	0.07±0.02	0.06±0.02	0.09±0.03	0.07±0.02	0.03±0.02
$70 \rightarrow \infty$	0.04±0.03	0.07±0.03	0.08±0.05	0.03±0.02	0.01±0.01

Table 6.1: Fake rates evaluated in the $t\bar{t}$ MC sample

If the $t\bar{t}$ MC sample is run with the matrix method, one should get the same yield as for using it without the matrix method and the loose selection since all trilepton events are fakes. Figure 6.2 shows the comparison of the cutflow for the $t\bar{t}$ MC sample using and not using the matrix method. Both cutflows agree within the errors. Possible deviations come from statistical effects of the fake rate measurement and the usage of the matrix method. Since only probabilities for a lepton to be reconstructed as tight are measured, the matrix method would give the same result as MC only for high statistics and perfectly measured rates. Also in figure 6.2, the output of the matrix method is shown separately for events with a different number of fake leptons at the leptonp_T cut stage. It is basically every single term of equation 6.1 plus the term with the yield for the real leptons. The bin with only real leptons agrees with zero within the errors as it was expected from the $t\bar{t}$ sample. The largest contribution comes from events, where the lepton with the lowest p_T is a fake lepton. This is also expected since fake leptons usually

electrons				
p_T [GeV]; $\|\eta\|$	$0.0 \rightarrow 0.7$	$0.7 \rightarrow 1.4$	$1.4 \rightarrow 2.0$	$2.0 \rightarrow 2.5$
$20 \rightarrow 30$	0.85±0.01	0.74±0.01	0.72±0.01	0.80±0.01
$30 \rightarrow 40$	0.92±0.01	0.84±0.01	0.84±0.01	0.88±0.01
$40 \rightarrow 50$	0.92±0.01	0.84±0.01	0.85±0.01	0.89±0.01
$50 \rightarrow \infty$	0.92±0.01	0.85±0.01	0.85±0.01	0.89±0.01
muons				
p_T [GeV]; $\|\eta\|$	$0.0 \rightarrow 0.7$	$0.7 \rightarrow 1.4$	$1.4 \rightarrow 2.0$	$2.0 \rightarrow 2.5$
$20 \rightarrow 30$	0.92±0.01		0.95±0.01	
$30 \rightarrow 40$	0.93±0.01		0.95±0.01	
$40 \rightarrow 50$	0.99±0.01		0.99±0.01	
$50 \rightarrow \infty$	0.99±0.01		0.99±0.01	

Table 6.2: Real efficiencies evaluated in the Z+jets MC sample

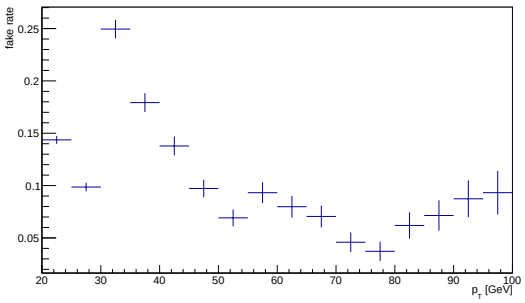

(a) Fake rates for electrons (p_T in GeV)

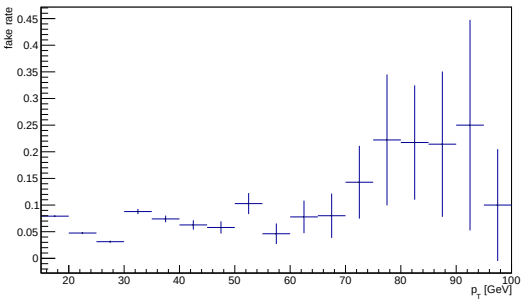

(b) Fake rates for muons (p_T in GeV)

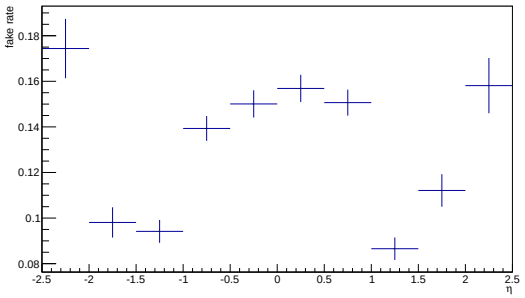

(c) Fake rates for electrons (η)

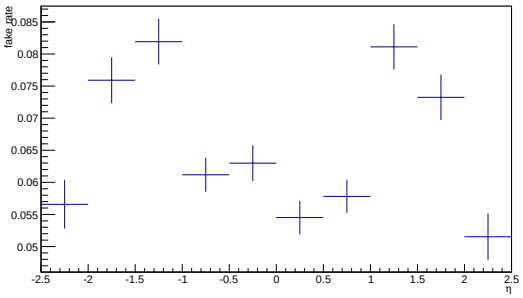

(d) Fake rates for muons (η)

Figure 6.1: Fake rate dependence on the transverse momentum and the pseudorapidity for electrons and muons evaluated in the $t\bar{t}$ MC sample

have low p_T. As a second cross-check, this method is applied to a sample where one would mostly expect three prompt leptons. As the WZ decay provides the largest event yield for such a kind of events, the matrix method is tested on it. Figure 6.3 shows again the cutflow and the composition of the event as it is computed by the matrix method. Only a small contribution of the events is considered as fake, which is ok since figure 5.1 also showed a small contribution not coming from W and Z. Nevertheless, most of the events were supposed to have three real leptons what is also shown with the matrix method.

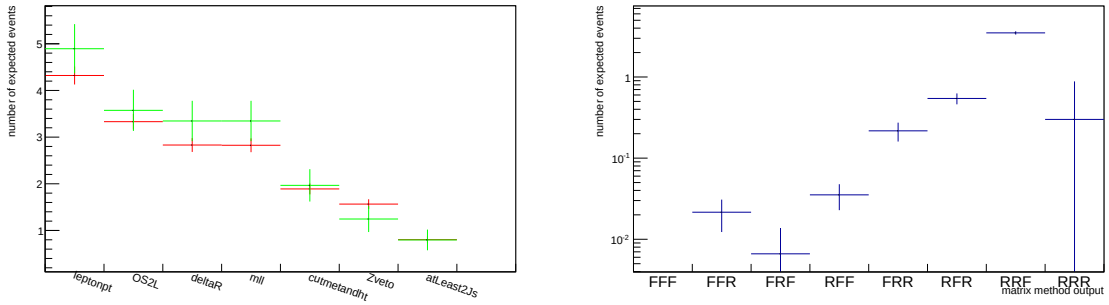

(a) $t\bar{t}$ cutflow with (green) and without (red) using the matrix method

(b) Event composition for $t\bar{t}$ using the matrix method

Figure 6.2: (a) Cutflow comparison between matrix method and the normal MC analysis for the $t\bar{t}$ sample. red(MC), green(matrix) (b) event composition at the leptonp_T cut stage taken from the matrix method

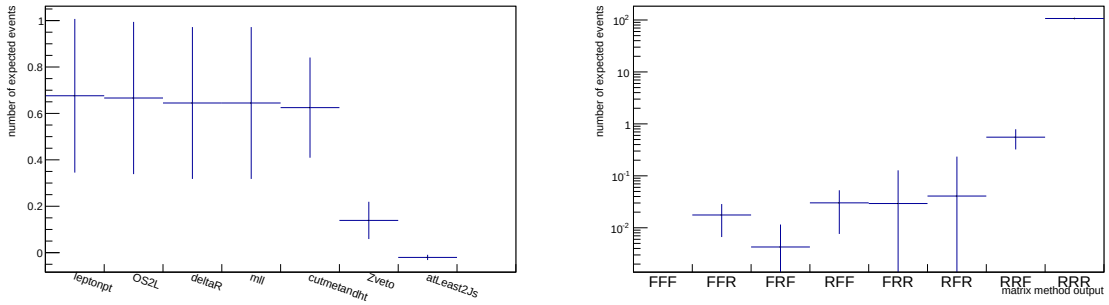

(a) WZ cutflow using the matrix method

(b) Event composition for WZ using the matrix method

Figure 6.3: (a) The cutflow of the WZ Monte Carlo sample using the matrix method. As the WZ decay predominantly provides three real leptons, the output of the matrix method should give a small event yield. (b) event composition at the leptonp_T cut stage taken from the matrix method

6.3 Fake estimation from data

The closure tests in MC promise a good functionality of the matrix method. Therefore the method is used in data to get an estimate of the fake contribution in trilepton events and to get a cross-check of the yields taken from the MC analysis.
Unlike for the closure tests, the fake rates are now measured in the low E_T^{miss} region as it is described in chapter 6.1. A plot of the E_T^{miss} distribution and the discrepancy of MC and data due to the fakes can

be seen in figure 6.4. The distribution is shown for loose and tight leptons separately. One can clearly see the increase of fakes at low E_T^{miss} due to the QCD contribution that is responsible for the fakes. The same effect can be seen for the p_T distribution in figure 6.5. It shows again the fake enriched low p_T region ($p_T < 40$ GeV), but there is still a significant fake contribution at high p_T for electrons, whereas muons do not show this behaviour.
The fake rates are measured using equation 6.2 for a p_T and η binning and separately for events with and without b-tagged jets. They are listed in tables 6.3 and 6.4 and are shown as histograms in figure 6.6. In order not to lose information of the jet, from which the fake lepton originated, the b-tagging algorithm is applied before the electron-jet overlap removal in the object selection is performed. The electron fake rates seem to look like one would expect them from the Monte Carlo tests. Especially for electrons, the fake rates with a b-tagged jet in the event are higher in the central region with $|\eta| < 1$ whereas they are slightly lower for muons over the whole η range. One significant difference between fake rates from Monte Carlo and data can be seen for muons in figures 6.6 and 6.7a. Above a transverse momentum of ≈ 50 GeV, the fake rates increase up to values between 0.8 and 0.9. On one hand, one could say that the fake muons coming from jets could become more signal like and well-isolated for high transverse momentum. On the other hand, the bins with $p_T > 50$ GeV and $\eta < -1.0$ in figure 6.6 for the 'muons - no b-tag' case are more compatible with the fake rates with low p_T. If one does not expect the fake rates to change at such a high rate, when one goes from negative to positive values of the pseudorapidity η, the fake rate measurement for muons at high p_T seems to be wrong. A problem could be the small statistics of fake muons at high p_T and the real lepton subtraction by Monte Carlo. This can be seen in the bottom plots of figure 6.5. Compared to the case of electrons, there are very few fake muon events so that the distributions of data and Monte Carlo background (only real leptons) almost match. Thus, there is lack of fake muons in this range. Assuming those high fake rates are simply wrong, all fake rates with values above 0.45 for a $p_T > 50$ GeV are set to 0.3 in the no b-tag case and 0.25 for events with a b-tagged jet. The other plots of figure 6.7 show the fake rate dependence on the pseudorapidity η, E_T^{miss} and the run period. The η distribution looks like the distribution measured in the $t\bar{t}$ MC sample (see figure 6.1), where possible deviations probably come from the different binning. In the E_T^{miss} distribution of the fake rates, one can see that it suffers from the same lack of statistics for high E_T^{miss} like it was shown for the p_T distribution before. This case is only different, because the same effect is observable for muons and electrons. Since the fake rates shouldn't depend on the E_T^{miss} , this is another hint that the fake rates for high p_T muons really make no sense and that there are regions, where the fake rate measurement can be problematic. The last plot shows the dependence of the fake rates on the run period. While the muon fake rate seems to be independent on the run period, the electron fake rates have increased from periods B-D to period K by 7 %. As the instantaneous luminosity increases for the newer runs (see table 5.3), pileup effects become more important and can lead to more "noise" and activity in the detector around the reconstructed leptons. But this should actually decrease the leptons' fake rates as it becomes more likely for them not to be reconstructed as tight lepton due to the pileup effects.
To account for the different measurement of the real efficiencies explained in chapter 6.1, the measured real efficiencies have to be scaled. Tables 6.5 and 6.6 show them for this measurement and the one provided by the top fakes group. Due to not using a tag-and-probe method, too many loose leptons are taken for the measurement which results in smaller fake rates. This can clearly be seen for the electron efficiencies, whereas the efficiencies for muons seem to agree with each other. As the ratio of the different real efficiencies seems to be constant looking at the same η-interval (see table 6.7), the arithmetic mean of the ratios is taken and the inverse of it applied to the measured efficiency of electrons with $p_T < 30$ GeV. For electrons with $p_T > 30$ GeV, real efficiencies of table 6.6 are taken.
Figure 6.8 shows a twodimensional histogram with particle's p_T on the x axis and the E_T^{cone} variable on the y axis for all measured data events. The black line indicates the begin of the tight selection.

For electrons one can very well see the transition from the real lepton dominated region to the fake dominated one. Furthermore, the distribution is very smooth and doesn't contain any spikes. On the contrary, the muon distribution has a peak at 18 GeV, that cannot be explained and could have unexpected effects on the fake rate measurement. The distribution for the fake rate measurement or the signal region, where the matrix method is applied, could of course look a little bit different because no cuts were applied before taking those leptons. It is more used as illustration how data events are distributed in this twodimensional plane and to compare it with the figures taken from the $t\bar{t}$ MC sample.

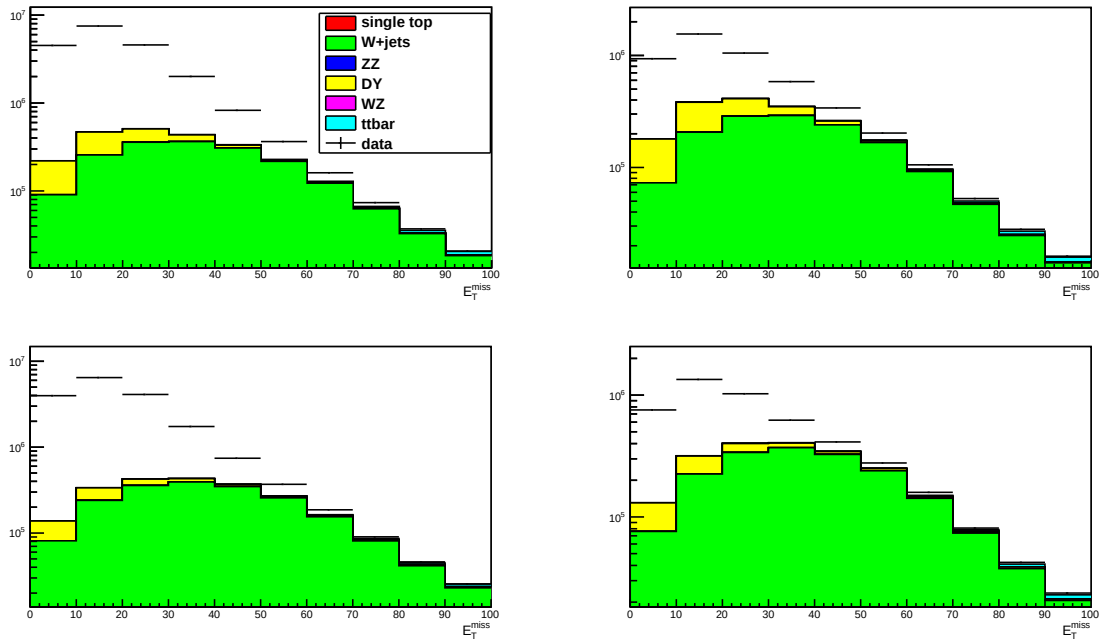

Figure 6.4: E_T^{miss} distribution for the fake measurement before the E_T^{miss} window cut is applied. left: loose leptons; right: tight leptons; top: electrons; bottom: muons

6.4 Event yield using the matrix method

After having measured fake rates and real efficiencies for electrons and muons and corrected them for specific p_T regions, they can be applied to the data. Just like for the Monte Carlo case, the whole 2.05 fb^{-1} of data is run with the loose selection and the events weighted by the output of the matrix method. Figure 6.9 shows the cutflow, where the number of fake events is now estimated from data by the matrix method. The real trilepton estimation is still taken from Monte Carlo and added to the fake contribution. As one can see, data and the estimated background agree very well for every cut stage. No systematic uncertainties are applied to the background. After the last cut, one expects 3.82 ± 0.97 background events when using the matrix method for the fake estimation. The expected yield agrees very well with the four measured events in data and also within 2σ with the expected yield from purely Monte Carlo background estimation.
The uncertainty from the matrix method up to this point is purely statistical. To get an estimate of how sensitive the matrix method is to its input parameters, the fake rates are varied by ± 10%, which is higher than the statistical uncertainty of the fake rates, and applied to the matrix method. For the

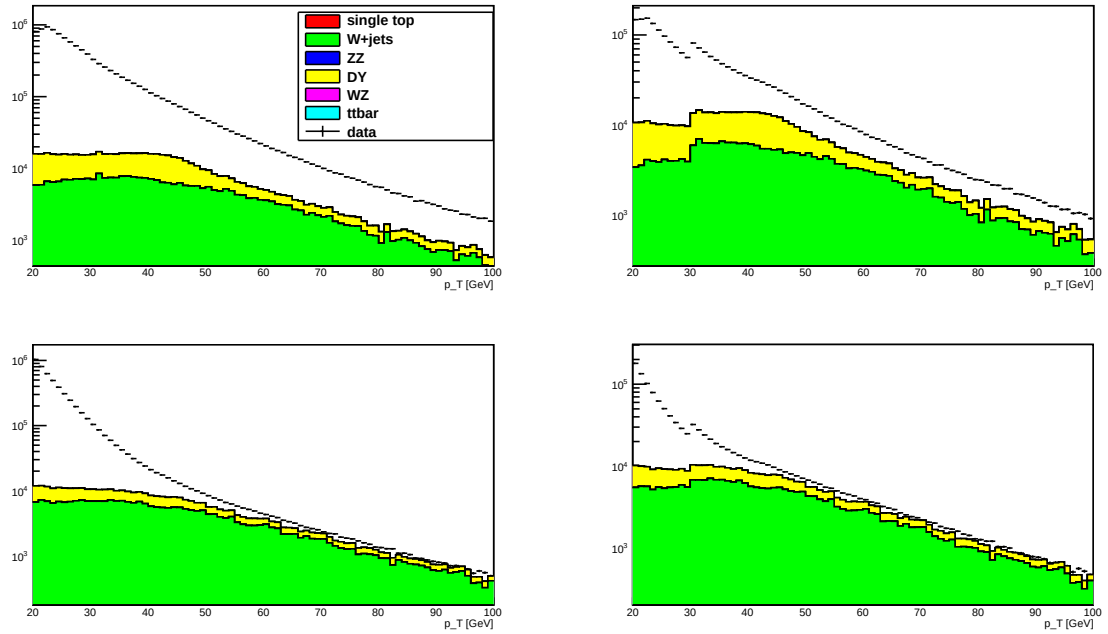

Figure 6.5: p_T distribution for the fake measurement after all cuts are applied. left: loose leptons; right: tight leptons; top: electrons; bottom: muons

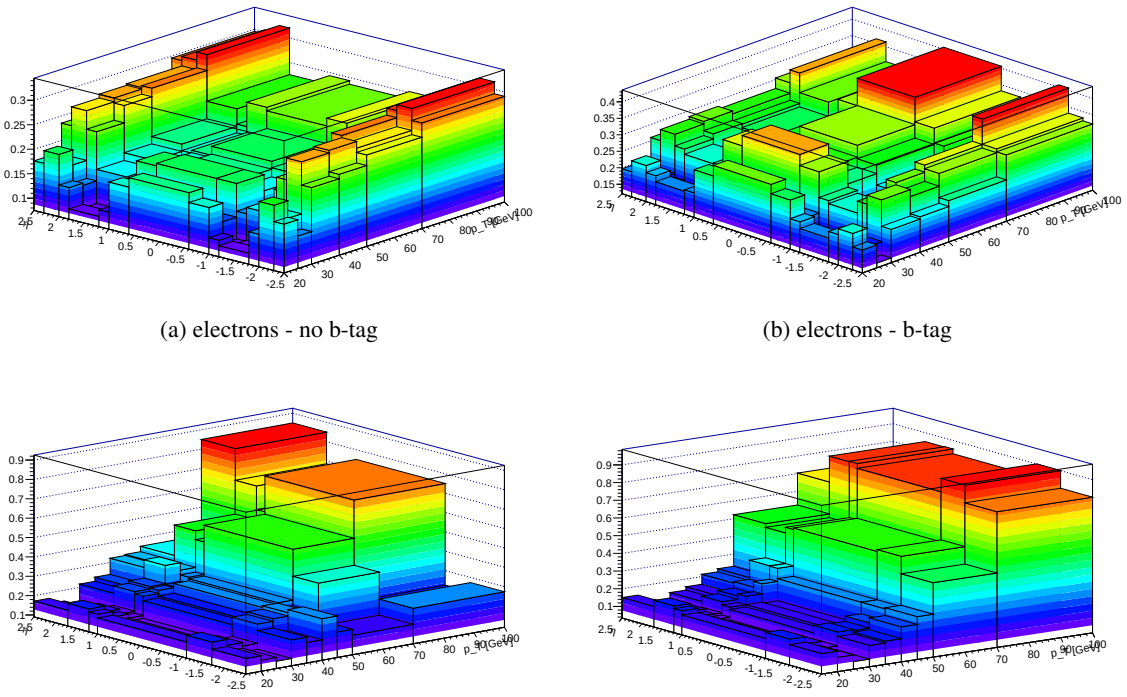

(a) electrons - no b-tag

(b) electrons - b-tag

(c) muons - no b-tag

(d) muons - b-tag

Figure 6.6: Fake rates measured with a p_T and η binning for electrons and muons with and without at least one b-tagged jet in the event

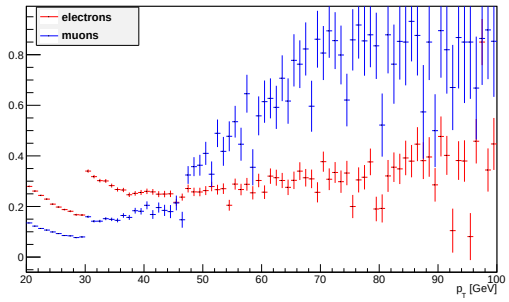

(a) Fake rates depending on the transverse momentum p_T

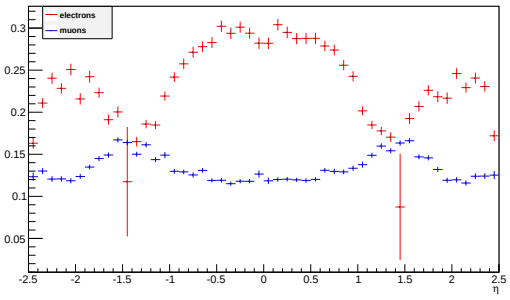

(b) Fake rates depending on the pseudorapidity η

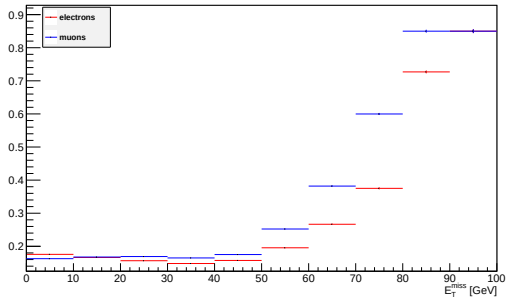

(c) Fake rates depending on E_T^{miss}

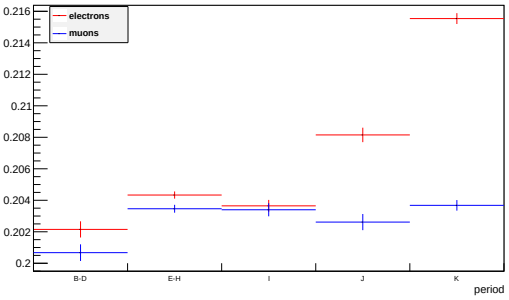

(d) Fake rates depending on the run period

Figure 6.7: Fake rates of electrons and muons for different variables

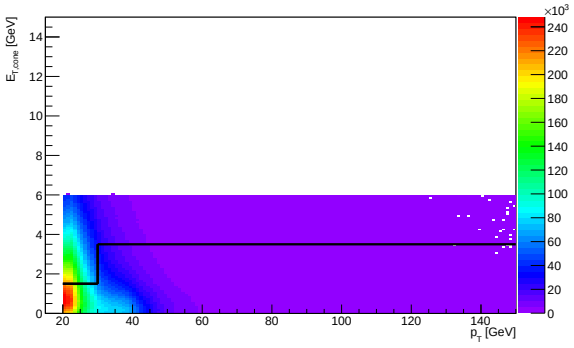

(a) electrons

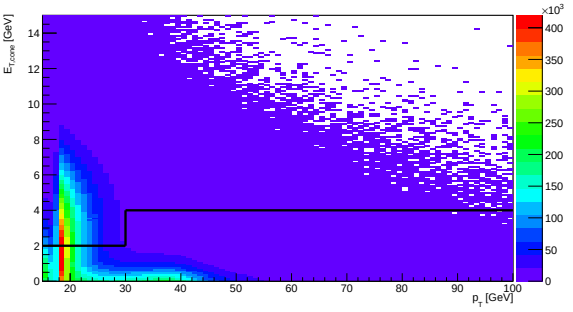

(b) muons

Figure 6.8: $E_{T,cone}$ vs. p_T for electrons and muons using all the events from data.

electrons - no b-tagged jet					
p_T [GeV]; η	$-2.5 \to -2.3$	$-2.3 \to -2.0$	$-2.0 \to -1.8$	$-1.8 \to -1.2$	$-1.2 \to -1.0$
$20 \to 25$	0.175±0.001	0.209±0.001	0.141±0.001	0.098±0.001	0.109±0.001
$25 \to 30$	0.142±0.001	0.173±0.001	0.136±0.001	0.090±0.001	0.088±0.001
$30 \to 40$	0.231±0.002	0.279±0.002	0.235±0.002	0.158±0.001	0.145±0.002
$40 \to 50$	0.204±0.003	0.284±0.003	0.258±0.004	0.177±0.002	0.146±0.003
$50 \to 70$	0.262±0.004	0.271±0.004	0.289±0.005	0.197±0.003	0.158±0.004
$70 \to \infty$	0.291±0.010	0.316±0.008	0.304±0.011	0.236±0.006	0.219±0.009
p_T [GeV]; η	$-1.0 \to -0.6$	$-0.6 \to 0.6$	$0.6 \to 1.0$	$1.0 \to 1.2$	$1.2 \to 1.8$
$20 \to 25$	0.171±0.001	0.191±0.001	0.171±0.001	0.110±0.001	0.096±0.001
$25 \to 30$	0.133±0.001	0.145±0.001	0.134±0.001	0.087±0.001	0.089±0.001
$30 \to 40$	0.202±0.002	0.202±0.001	0.197±0.001	0.154±0.001	0.159±0.001
$40 \to 50$	0.169±0.003	0.184±0.002	0.177±0.003	0.150±0.003	0.175±0.002
$50 \to 70$	0.187±0.004	0.200±0.003	0.182±0.004	0.176±0.005	0.189±0.003
$70 \to \infty$	0.252±0.007	0.236±0.005	0.244±0.007	0.194±0.009	0.225±0.006
p_T [GeV]; η	$1.8 \to 2.0$	$2.0 \to 2.3$	$2.3 \to 2.5$		
$20 \to 25$	0.140±0.001	0.202±0.001	0.176±0.001		
$25 \to 30$	0.135±0.001	0.172±0.001	0.142±0.001		
$30 \to 40$	0.235±0.002	0.274±0.001	0.235±0.002		
$40 \to 50$	0.271±0.004	0.281±0.003	0.25±0.003		
$50 \to 70$	0.288±0.005	0.285±0.004	0.261±0.004		
$70 \to \infty$	0.321±0.010	0.304±0.008	0.296±0.009		
electrons - at least one b-tagged jet					
p_T [GeV]; η	$-2.5 \to -2.3$	$-2.3 \to -2.0$	$-2.0 \to -1.8$	$-1.8 \to -1.2$	$-1.2 \to -1.0$
$20 \to 25$	0.191±0.007	0.232±0.005	0.214±0.006	0.194±0.003	0.214±0.005
$25 \to 30$	0.136±0.007	0.176±0.006	0.174±0.008	0.145±0.004	0.143±0.006
$30 \to 40$	0.222±0.010	0.302±0.010	0.274±0.013	0.238±0.007	0.247±0.010
$40 \to 50$	0.229±0.017	0.281±0.017	0.309±0.022	0.220±0.012	0.186±0.016
$50 \to 70$	0.247±0.022	0.320±0.022	0.330±0.030	0.238±0.017	0.222±0.024
$70 \to \infty$	0.323±0.048	0.331±0.045	0.407±0.043	0.240±0.030	0.287±0.046
p_T [GeV]; η	$-1.0 \to -0.6$	$-0.6 \to 0.6$	$0.6 \to 1.0$	$1.0 \to 1.2$	$1.2 \to 1.8$
$20 \to 25$	0.271±0.004	0.299±0.003	0.266±0.004	0.196±0.005	0.191±0.003
$25 \to 30$	0.200±0.005	0.227±0.003	0.212±0.005	0.146±0.006	0.142±0.004
$30 \to 40$	0.325±0.008	0.358±0.006	0.327±0.008	0.246±0.010	0.243±0.007
$40 \to 50$	0.257±0.015	0.287±0.010	0.232±0.014	0.194±0.016	0.206±0.011
$50 \to 70$	0.282±0.019	0.323±0.014	0.283±0.020	0.202±0.024	0.261±0.015
$70 \to \infty$	0.332±0.037	0.406±0.023	0.323±0.037	0.246±0.048	0.305±0.031
p_T [GeV]; η	$1.8 \to 2.0$	$2.0 \to 2.3$	$2.3 \to 2.5$		
$20 \to 25$	0.209±0.007	0.231±0.005	0.197±0.007		
$25 \to 30$	0.164±0.008	0.176±0.006	0.149±0.007		
$30 \to 40$	0.259±0.012	0.294±0.009	0.261±0.011		
$40 \to 50$	0.274±0.021	0.302±0.064	0.261±0.019		
$50 \to 70$	0.272±0.027	0.293±0.020	0.254±0.024		
$70 \to \infty$	0.364±0.053	0.325±0.042	0.219±0.043		

Table 6.3: Electron fake rates measured in a low E_T^{miss} region in data

muons - no b-tagged jet			
p_T [GeV]; η	$-2.5 \rightarrow -1.7$	$-1.7 \rightarrow -1.1$	$-1.1 \rightarrow 1.0$
$15 \rightarrow 20$	0.171±0.001	0.208±0.001	0.173±0.001
$20 \rightarrow 25$	0.148±0.001	0.178±0.001	0.145±0.001
$25 \rightarrow 30$	0.128±0.001	0.159±0.001	0.129±0.001
$30 \rightarrow 35$	0.224±0.003	0.259±0.003	0.22±0.002
$35 \rightarrow 40$	0.196±0.006	0.272±0.006	0.23±0.003
$40 \rightarrow 45$	0.305±0.009	0.289±0.008	0.28±0.005
$45 \rightarrow 50$	0.222±0.011	0.261±0.011	0.29±0.006
$50 \rightarrow 70$	0.191±0.008	0.413±0.009	0.552±0.005
$70 \rightarrow \infty$	0.274±0.014	0.225±0.014	0.75±0.008
p_T [GeV]; η	$1.0 \rightarrow 1.2$	$1.2 \rightarrow 1.7$	$1.7 \rightarrow 2.5$
$15 \rightarrow 20$	0.193±0.001	0.208±0.001	0.172±0.001
$20 \rightarrow 25$	0.165±0.001	0.178±0.001	0.144±0.001
$25 \rightarrow 30$	0.144±0.003	0.154±0.001	0.131±0.001
$30 \rightarrow 35$	0.243±0.006	0.255±0.004	0.217±0.003
$35 \rightarrow 40$	0.259±0.011	0.267±0.006	0.238±0.006
$40 \rightarrow 45$	0.265±0.016	0.362±0.009	0.322±0.008
$45 \rightarrow 50$	0.299±0.021	0.323±0.012	0.327±0.011
$50 \rightarrow 70$	0.466±0.016	0.512±0.009	0.355±0.008
$70 \rightarrow \infty$	0.565±0.027	0.687±0.016	0.85±0.014
muons - at least one b-tagged jet			
p_T [GeV]; η	$-2.5 \rightarrow -1.7$	$-1.7 \rightarrow -1.1$	$-1.1 \rightarrow 1.0$
$15 \rightarrow 20$	0.150±0.002	0.181±0.002	0.147±0.001
$20 \rightarrow 25$	0.115±0.002	0.141±0.002	0.11±0.001
$25 \rightarrow 30$	0.078±0.002	0.102±0.003	0.078±0.001
$30 \rightarrow 35$	0.155±0.006	0.180±0.007	0.137±0.003
$35 \rightarrow 40$	0.166±0.011	0.175±0.012	0.151±0.006
$40 \rightarrow 45$	0.233±0.024	0.204±0.023	0.145±0.012
$45 \rightarrow 50$	0.277±0.041	0.270±0.042	0.270±0.022
$50 \rightarrow 70$	0.455±0.045	0.553±0.042	0.542±0.023
$70 \rightarrow \infty$	0.801±0.084	0.901±0.075	0.825±0.037
p_T [GeV]; η	$1.0 \rightarrow 1.2$	$1.2 \rightarrow 1.7$	$1.7 \rightarrow 2.5$
$15 \rightarrow 20$	0.171±0.004	0.185±0.002	0.150±0.002
$20 \rightarrow 25$	0.126±0.003	0.141±0.002	0.113±0.002
$25 \rightarrow 30$	0.092±0.005	0.105±0.003	0.082±0.002
$30 \rightarrow 35$	0.150±0.012	0.168±0.007	0.138±0.006
$35 \rightarrow 40$	0.198±0.025	0.186±0.013	0.157±0.012
$40 \rightarrow 45$	0.254±0.048	0.223±0.025	0.213±0.024
$45 \rightarrow 50$	0.328±0.085	0.330±0.045	0.231±0.041
$50 \rightarrow 70$	0.534±0.084	0.502±0.048	0.523±0.047
$70 \rightarrow \infty$	0.852±0.126	0.85±0.079	0.703±0.080

Table 6.4: Muon fake rates measured in a low E_T^{miss} region in data

electrons				
p_T [GeV]; $\|\eta\|$	0.0 → 0.7	0.7 → 1.4	1.4 → 2.0	2.0 → 2.5
20 → 30	0.815±0.008	0.739±0.009	0.748±0.012	0.771±0.012
30 → 40	0.902±0.005	0.872±0.006	0.837±0.009	0.848±0.010
40 → 50	0.914±0.005	0.886±0.006	0.871±0.008	0.887±0.009
50 → ∞	0.923±0.009	0.899±0.010	0.876±0.015	0.888±0.018
muons				
p_T [GeV]; $\|\eta\|$	0.0 → 1.1		1.1 → 2.5	
15 → 20	0.931±0.014		0.950±0.011	
20 → 30	0.934±0.006		0.955±0.006	
30 → 40	0.986±0.004		0.987±0.005	
40 → ∞	0.990±0.003		0.991±0.003	

Table 6.5: Real efficiencies measured in a Z-window in data

electrons				
p_T [GeV]; $\|\eta\|$	0.0 → 0.7	0.7 → 1.4	1.4 → 2.0	2.0 → 2.5
20 → 30	0.894	0.867	0.878	0.879
30 → 40	0.915	0.894	0.895	0.931
40 → 50	0.926	0.908	0.921	0.959
50 → ∞	0.937	0.928	0.941	0.966
muons				
p_T [GeV]; $\|\eta\|$	0.0 → 1.1		1.1 → 2.5	
20 → 30	0.985		0.989	
30 → 40	0.989		0.987	
40 → ∞	0.993		0.994	

Table 6.6: Real efficiencies from Top Fakes Group [37]

electrons				
p_T [GeV]; $\|\eta\|$	0.0 → 0.7	0.7 → 1.4	1.4 → 2.0	2.0 → 2.5
30 → 40	0.986	0.975	0.935	0.910
40 → 50	0.987	0.975	0.946	0.899
50 → ∞	0.985	0.968	0.932	0.919
arithmetic mean	0.986	0.973	0.938	0.909

Table 6.7: Ratio of the real efficiencies of tables 6.5 and 6.6 for electrons

upward variation, the total background changes to 4.21 ± 1.10, for the downward variation to 3.43 ± 0.85. The background contribution from WZ and ZZ is not affected by the change of the fake rates because they are still taken from Monte Carlo. So the change in the total background comes. So this gives a symmetric systematic uncertainty of ±0.39 events. Adding this systematic uncertainty and the systematic uncertainty from the real lepton MC background quadratically and adding this uncertainty again quadratically with the statistical uncertainty, the final background expectation using fakes by the matrix method is 3.82 ± 1.04 events.
Figures 6.10 and 6.11 show the input and output of the matrix method at the leptonp_T cut stage. In 6.10, the largest contribution comes from events with three tight leptons and events, where the third lepton is loose. The ≈160 events in the TTT bin are the events, that are measured when one doesn't use the matrix method. With the loose lepton being the second or first lepton, thus having high p_T, the number of events drastically decreases, but there is still a significant contribution by them. Events with two loose leptons are not so likely, but also appear quite often, if the first lepton is tight. The other contributions get very small. Figure 6.11 shows the output of the matrix method after the matrix and the rates and efficiencies are applied. There is a logarithmic decrease as one goes from events with a fake third lepton to events with a real first lepton. This behaviour could also be seen in figure 6.2b, where the fakes were measured in the $t\bar{t}$ Monte Carlo sample. So one can conclude that at the leptonp_T cut stage, there seem to be fakes that mostly resemble fakes from $t\bar{t}$.
The usage of the matrix method gives a result that is more compatible with data than the background estimation using exclusively simulated data from Monte Carlo. Nevertheless, regarding the relatively large uncertainties for both methods and the Poisson error of data, none of them disagree significantly and the Monte Carlo estimation is therefore validated by the matrix method

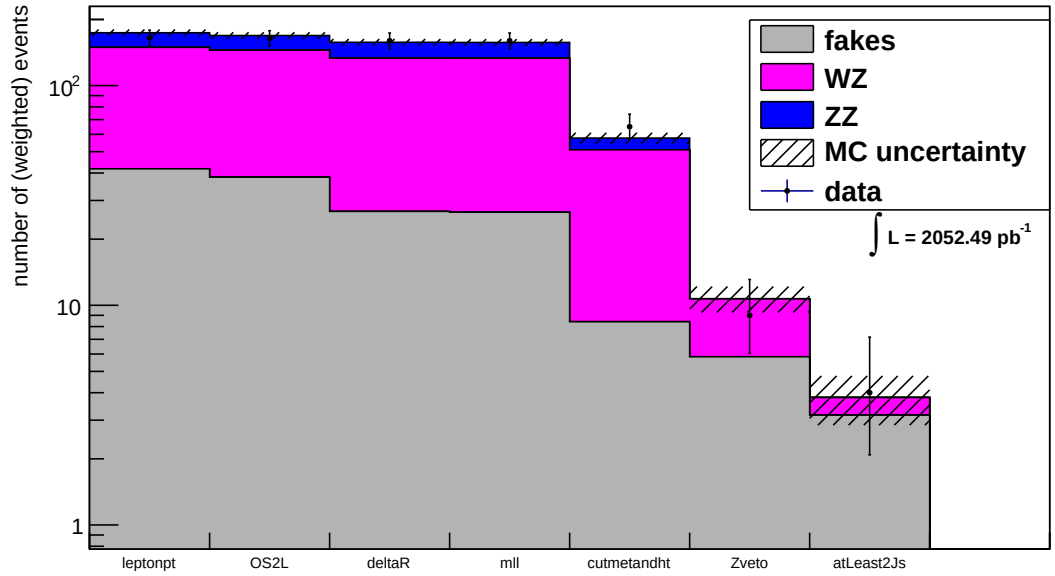

Figure 6.9: Cutflow with fake estimation taken from data by the matrix method.

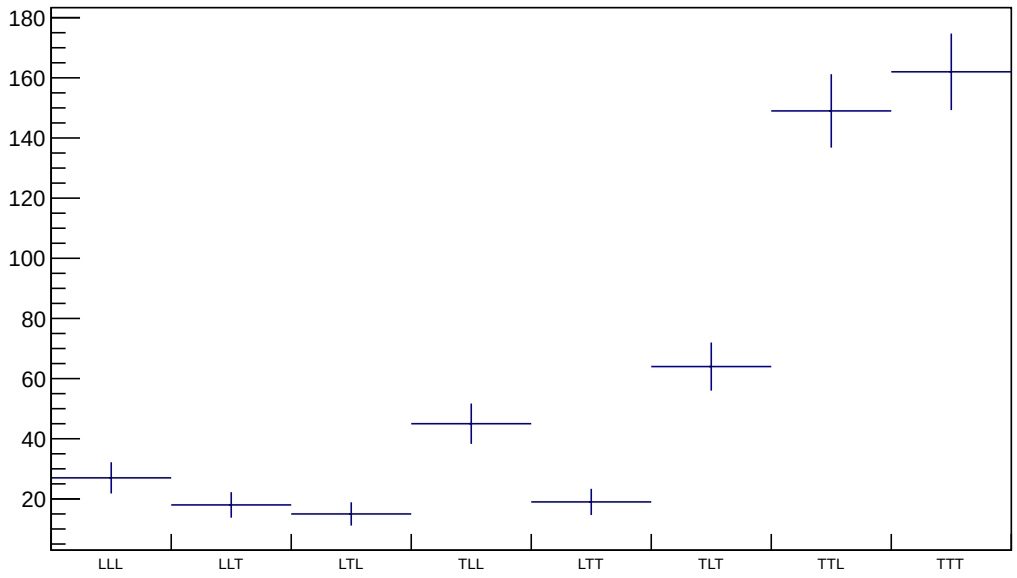

Figure 6.10: Event composition by loose and tight leptons as used by the matrix method at the leptonp_T cut stage.

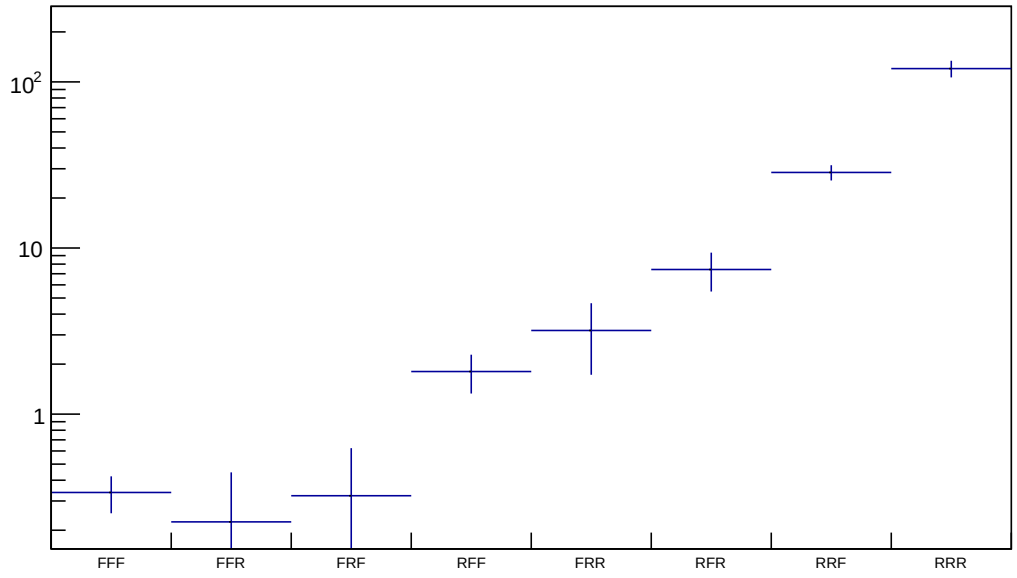

Figure 6.11: Event composition by fake and real leptons as given by the matrix method at the leptonp_T cut stage in a logarithmic scale.

Chapter 7

Limit Setting using the CL_s method

In order to interpret the result obtained from the cut and count analysis, one has to use methods which can set limits on the hypothesized parameters that one tested. The basic question is, how compatible is the measured result with the expectation I had for various scenarios? One of these methods is the so called CL_s method developed by Alex Read for the Higgs boson search at LEP [39]. It allows to determine an exclusion interval for a certain signal hypothesis.
The basic idea of limit setting is the creation of a test statistic Q for a null (background) and an alternative (signal+background) hypothesis, which gives a good discrimination of both. Either the shape of the distribution is known or the probability density function (pdf) for the test statistic of both hypotheses is built with toy MC samples. Usually, the test statistics are positive and the signal+background hypothesis reaches up to larger values. This can be easily seen if one takes the Poisson distribution, which is the pdf of a counting experiment with one channel. If one observes a certain value Q_{obs} for this test statistic in data, it is easy to calculate the probability to observe a value smaller than Q_{obs}, which gives us the confidences CL_{s+b} and CL_b for both hypotheses:

$$CL_{s+b} \equiv P_{s+b}(Q \leq Q_{obs}) = \int_{-\infty}^{Q_{obs}} \frac{dP_{s+b}}{dQ} dQ \tag{7.1}$$

$$CL_b \equiv P_b(Q \leq Q_{obs}) = \int_{-\infty}^{Q_{obs}} \frac{dP_b}{dQ} dQ \tag{7.2}$$

Values of CL_b close to 1 point out a non-background like behaviour whereas small values of CL_{s+b} demonstrate bad compability with the signal+background hypothesis. The interpretation of these confidences is shown in the so called p-values. Exclusion of the background hypothesis (i.e. discovery) is observed, if $p_{value}(CL_b) \equiv 1-CL_b < 5.7 \cdot 10^{-7}$, which can be expressed in terms of Gaussian standard deviations as 5σ [40]. Exclusion of an alternative hypothesis is achieved, if $p_{value}(CL_{s+b}) \equiv CL_{s+b} < 0.05$, also called exclusion at 95% confidence level (CL).
However, this interpretation of the measured results can pose a problem if a downward fluctuation of the background is involved in the measurement. This situation could lead to a strong exclusion of even zero signal at 95% CL. To account for this effect and to reduce the influence of the background hypothesis on the measurement, the confidence level of the signal+background hypothesis is normalized by the confidence level of the background hypothesis, leading to the modified frequentist re-normalization

$$CL_s \equiv CL_{s+b}/CL_b. \tag{7.3}$$

The test statistic that is used in this analysis is the likelihood ratio $Q = \mathcal{L}_{s+b}(x)/\mathcal{L}_b(x)$, which is, according to the Neyman-Pearson lemma [41], the strongest test to distinguish two different hypotheses. $\mathcal{L}(x)$ labels the likelihood function for a given observable x. For a simple counting experiment like this analysis, x is the number of observed events and therefore $\mathcal{L}(x)$ the Poisson distribution $f(x,\mu) = \frac{\mu^x}{x!} exp(-\mu)$ where μ is the mean value of the distribution. In a counting experiment with just one channel, i.e. one

only counts all the events no matter what kind of different signature they belong to, just the Poisson distributions are integrated for the calculation of CL_s. Hence, the exclusion confidence for the signal is

$$CL \equiv 1 - CL_s = 1 - \frac{\sum_{n=0}^{n_{obs}} \frac{e^{-(s+b)}(s+b)^n}{n!}}{\sum_{n=0}^{n_{obs}} \frac{e^{-b}b^n}{n!}}. \tag{7.4}$$

n_{obs} is the number of observerd events, b and s are the background and signal estimation (from MC). In this analysis, events can be distinguished by their lepton content to four different channels, this would be $e^+e^-e^\pm$, $e^+e^-\mu^\pm$, $\mu^+\mu^-e^\pm$ and $\mu^+\mu^-\mu^\pm$. To combine the different channels to get the total likelihood ratio Q_{tot}, the different likelihood ratios are simply multiplied. Considering that we deal with Poisson distributions and taking the logarithm for convenience, one gets

$$lnQ_{tot} = -s_{tot} + \sum_{i \in channel} n_{obs,i} ln(1 + \frac{s_i}{b_i}). \tag{7.5}$$

This means that every channel contributes with a weight of $ln(1 + \frac{s_i}{b_i})$ to the combined (log) likelihood ratio. To get the probability density function of the combined likelihood ratio, equation (7.5) is often evaluated with random numbers for $n_{obs,i}$ according to the MC estimation for background and signal respectively, where the random numbers have to follow a Poisson distribution. An example how the distribution looks like is pictured in figure 7.1 using the background estimation from MC and data events obtained after all cuts. $-2 \cdot lnQ_{tot}$ is usually shown, because this should converge to $\Delta\chi^2$ distributions for high statistics. The CL_b value for the distribution in 7.1 is 0.93. Thus, it tends to be not background-like, but it is still below 2σ when speaking of standard deviations. The shape of the background distribution is caused by the small event yield for each channel. For such a small mean value, the Poisson distributed random number gives often zero for each or some channels resulting in a non-smooth shape. To consider systematic effects on the measurement of the distributions, the estimation for background and signal from MC is used as the mean for a random number, that follows a Gaussian distribution with a width defined by the systematic uncertainty for signal and background. This increases the overlap of the $(s + b)$- and b-hypothesis and so decreases the confidence level slightly in the end. Since a negative number of events could be possible by this procedure, all negative event numbers are set to 0. Just as for the case without the combination of the channels, the distributions have to be integrated up to the observed point in data. Since the distribution is made of $-2 \cdot lnQ_{tot}$, i.e. it is multiplied with a negative number, the distributions have to be integrated from the right to the observed value. Doing this for both hypotheses, one gets CL_{s+b} and CL_b and can thus calculate CL_s to get the confidence level for each signal point. The confidence levels for the different signal modes are shown in 7.2. The combination of the channels gives a much better confidence level than just taking one channel with the sum of all events. The reason is, that one has more information about the composition of the events and that every channel has to be compatible with the signal to be not excluded. If just one or two channels show a more signal-like behaviour and the others not, the observed value will be on the more background like side of the distribution for the $s + b$ hypothesis shown in 7.1. As the number of expected events after all cuts was higher for $m_{qluino} > m_{squark}$, a much larger range can be excluded there. Likewise, the light lsp mode bares a wider exclusion range than the compressed mode because of the larger number of expected events that were obtained after all cuts. Exclusions are usually called exclusion at xx % confidence level, where typically 95 % is taken. This value will be used here to call a mass excluded, if its confidence level is higher than 0.95. For both scenarios, masses of gluinos smaller than 400 GeV can be excluded. Excluded squark masses are 700 GeV for the light lsp mode and 600 GeV for the

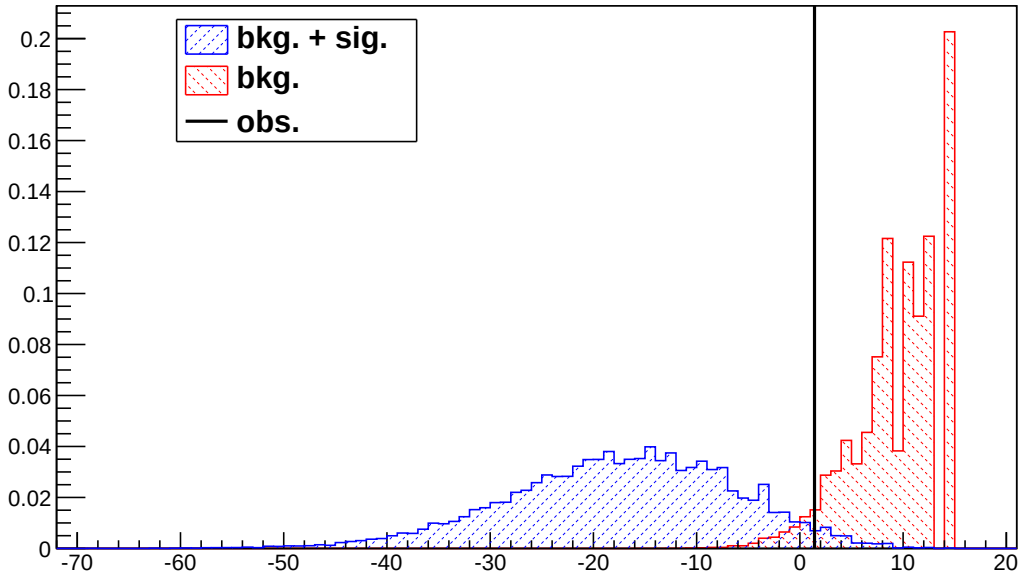

Figure 7.1: $-2 \cdot lnQ_{tot}$ as defined in equation 7.5. The integral of the distributions is normalized to 1.

compressed one. Assuming equal masses for squarks and gluinos, the exclusion would be 900 GeV in the light lsp scenario and in the compressed scenario 800 GeV.

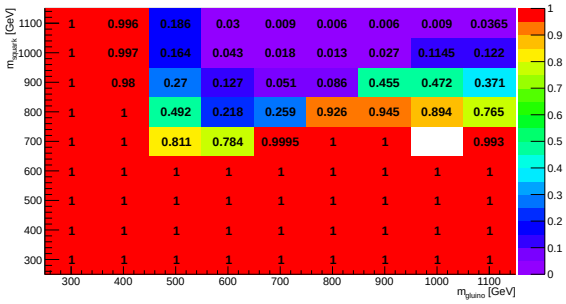

(a) light lsp mode, without combination of channels

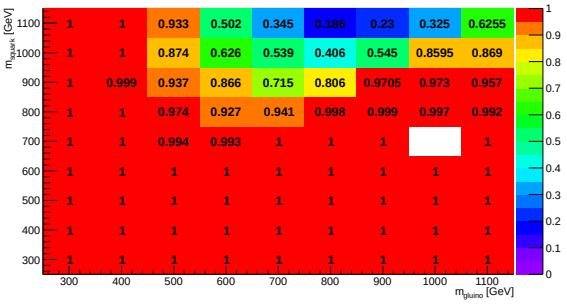

(b) light lsp mode, with combination of channels

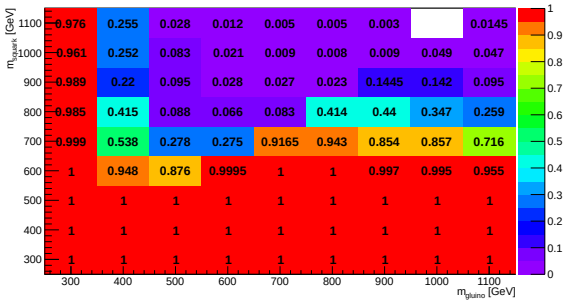

(c) compressed mode, without combination of channels

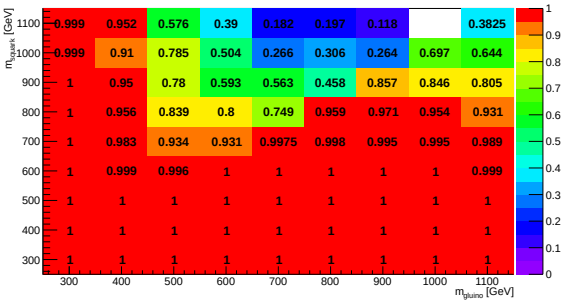

(d) compressed mode, with combination of channels

Figure 7.2: Confidence level of the grid points for the different modes and with/without combination of the channels; white spaces don't contain confidence levels due to missing MC samples. For the diagonal, the arithmetic mean is again taken for the two close by grid points.

Chapter 8

Conclusion

In order to look for new physics, clean channels and signatures with small background from known physics are desired. This is the main reason, that the so called trilepton channel is interesting to look at. The only contribution from the Standard Model is the leptonic decay of W and Z bosons from diboson production, which has a cross section of the order of a few pb. Due to secondary decays like photon conversion or semileptonic b-decays and misreconstruced jets, processes like the leptonic Z decay or the dileptonic $t\bar{t}$ decay channel can also form a final state with three leptons, but are more difficult to model in MC. On the other side, BSM theories like SUSY offer many possibilities to form final states with three leptons. Therefore a search for trilepton events using 2.05 fb^{-1} data from the ATLAS experiment at the LHC is done in this thesis.

In the first part of the thesis, a cut-and-count analysis is performed. As a signal, a mSUGRA like, R-parity conserving phenomenological model using masses of squarks, gluinos and the lsp as input parameters was taken and tanβ set to 4. There are two different scenarios for the model, one with a light lsp of 100 GeV and a compressed mode with a mass of the lsp that is much closer to the masses of the gluinos and squarks. The event topology, which was targeted at, included the production of gluinos and squarks, that should decay to gauginos and SM quarks. By the further decay of the gauginos, the desired final state should include three isolated leptons with an opposite sign, same flavour pair, 2 jets and high E_T^{miss} due to a neutrino and the lightest neutralinos, that are the lsp in this model. Cuts were defined based on this topology and a $\frac{signal}{\sqrt{background}}$ optimisation done for kinematic variables. Thus, looking for three leptons with E_T^{miss} and jets in an event, the expected Standard Model background from Monte Carlo was $1.59^{+0.89}_{-0.92}$ including statistical and systematic uncertainties, whereas 4 ± 2 events were measured in the data sample of 2.05 fb^{-1}. Expectation and measurement are therefore in agreement within the uncertainties.

Since the Standard Model trilepton contribution, where secondary leptons are involved, is not so simple to model in Monte Carlo, data driven methods become important to validate Monte Carlo or to replace the Monte Carlo estimation of these "fake" trilepton events. The data driven method used in this analysis is the matrix method, that has already been used in analyses with one or two leptons and is extended to three leptons in this thesis. It is based on defining loose and tight selections for leptons and measuring fake rates and real efficiencies for loose fake/real leptons to be reconstructed as tight lepton. Measuring loose and tight leptons, the numbers of events containing a fake lepton can be calculated via a matrix containing the fake rates and real efficiencies. Applying the matrix method to the data, that was analysed in the cut-and-count analysis, and adding real trilepton contribution by WZ and ZZ decays from Monte Carlo, a Standard Model background of 3.82 ± 1.04 events including statistical and systematic uncertainties was calculated. It is compatible with the data measurement and also within 2σ with the expectation from only Monte Carlo samples, that are therefore validated.

Taking the measurement from data and the background estimation from Monte Carlo, limits to the gluino and squark masses for both scenarios are set. The calculation of the limits was done with the CL_s technique once with all observed events and once with a combination of 4 different channels, that can be distinguished by its lepton content. For both lsp scenarios, masses of gluinos smaller than 400 GeV can be excluded. Excluded squark masses are 700 GeV for the light lsp mode and 600 GeV for the compressed one. Assuming equal masses for squarks and gluinos, the exclusion would be 900 GeV in the light lsp scenario and in the compressed scenario 800 GeV. All exclusions are exclusions at 95 % confidence level or higher.

As a conclusion, no excess in data was observed looking for final states with three leptons, E_T^{miss} and jets in a data sample of 2fb^{-1} of the ATLAS experiment at the LHC and limits have been set to a phenomenological model of supersymmetry. The matrix method seems to be a good approach to estimate the trilepton background, that doesn't have three leptons from the primary decay, directly from data whereas Monte Carlo estimation is also in agreement with the measurements.

As more and more data will be taken at the LHC , the statistical uncertainty of data will decrease. Therefore data-driven methods for the fake estimation like the matrix method have to validate or falsify the Monte Carlo modeling of the fake trilepton events. An almost fakefree object selection by going to higher p_T and smaller E_T^{cone} is not desired for many models, as one also reduces the signal significantly. The matrix method showed a good functionality, but was performed in a simple way. A different fake enhanced region like low $m_T(W)$ could validate the measured fake rates and solve the problem with the too large fake rates for high p_T muons. For the measurement of the real efficiencies, a tag-and-probe method should be used instead of taking all leptons inside the Z window. Furthermore, a better way to handle the different fake sources could be used by using truth information from Monte Carlo and transferring the fake rates to the signal region, like it was done in [37]. For the limit setting, one could assume a linear behaviour of the confidence level between neighbouring grid points. By this procedure, more exact exclusion limits could be set by looking, at which gluino/squark mass the linear dependence reaches a confidence level of 0.95. But also methods like a profile likelihood fit could be an alternative to the limit setting in this analysis.

Appendix A

Monte Carlo samples used for analysis

process	sample	process	sample	process	sample
ttbar (dilep)	105200	ZtautauNp0	107670	single-top_s.chan_taunu	108345
WWlnulnuNp0	107100	ZtautauNp1	107671	single-top_Wt.chan	108346
WWlnulnuNp1	107101	ZtautauNp2	107672	ZeebbNp0	109300
WWlnulnuNp2	107102	ZtautauNp3	107673	ZeebbNp1	109301
WWlnulnuNp3	107103	ZtautauNp4	107674	ZeebbNp2	109302
WZincllNp0	107104	ZtautauNp4	107675	ZeebbNp3	109303
WZincllNp1	107105	WenuNp0	107680	ZmumubbNp0	109305
WZincllNp2	107106	WenuNp1	107681	ZmumubbNp1	109306
WZincllNp3	107107	WenuNp2	107682	ZmumubbNp2	109307
ZZincllNp0	107108	WenuNp3	107683	ZmumubbNp3	109308
ZZincllNp1	107109	WenuNp4	107684	ZtautaubbNp0	109310
ZZincllNp2	107110	WenuNp5	107685	ZtautaubbNp1	109311
ZZincllNp3	107111	WmunuNp0	107690	ZtautaubbNp2	109312
WbbNp0	107280	WmunuNp1	107691	ZtautaubbNp3	109313
WbbNp1	107281	WmunuNp2	107692	ZeeNp0_Mll10to40	116250
WbbNp2	107282	WmunuNp3	107693	ZeeNp1_Mll10to40	116251
WbbNp3	107283	WmunuNp4	107694	ZeeNp2_Mll10to40	116252
ZeeNp0	107650	WmunuNp5	107695	ZeeNp3_Mll10to40	116253
ZeeNp1	107651	WtaunuNp0	107700	ZeeNp4_Mll10to40	116254
ZeeNp2	107652	WtaunuNp1	107701	ZeeNp5_Mll10to40	116255
ZeeNp3	107653	WtaunuNp2	107702	ZmumuNp0_Mll10to40	116260
ZeeNp4	107654	WtaunuNp3	107703	ZmumuNp1_Mll10to40	116261
ZeeNp5	107655	WtaunuNp4	107704	ZmumuNp2_Mll10to40	116262
ZmumuNp0	107660	WtaunuNp5	107705	ZmumuNp3_Mll10to40	116263
ZmumuNp1	107661	single-top_t.chan_enu	108340	ZmumuNp4_Mll10to40	116264
ZmumuNp2	107662	single-top_t.chan_munu	108341	ZmumuNp5_Mll10to40	116265
ZmumuNp3	107663	single-top_t.chan_taunu	108342	ZtautauNp0_Mll10to40	116270
ZmumuNp4	107664	single-top_s.chan_enu	108343	ZtautauNp1_Mll10to40	116271
ZmumuNp5	107665	single-top_s.chan_munu	108344	ZtautauNp2_Mll10to40	116272

Table A.1: List of Monte Carlo samples (mc10b production) used in this analysis for background estimation; cross sections and k-factors for the analysis were taken from [20]

process	sample
ZtautauNp3_Mll10to40	116273
ZtautauNp4_Mll10to40	116274
ZtautauNp5_Mll10to40	116275
WW Herwig	105985
WZ Herwig	105986
ZZ Herwig	105987
AcerMCttbar	105205
TTbar PowHeg Jimmy	105860
TTbar PowHeg Pythia	105861
AcerMCttbar_isr_down	117255
AcerMCttbar_isr_up	117256
AcerMCttbar_fsr_down	117257
AcerMCttbar_fsr_up	117258
AcerMCttbar_isr_down_fsr_down	117259
AcerMCttbar_isr_up_fsr_up	117260

Table A.2: List of Monte Carlo samples (mc10b production) used in this analysis for background estimation; cross sections and k-factors for the analysis were taken from [20]

run	m_{gluino}	m_{squark}	m_{lsp}	cross section * filter eff. []	# after last cut
137976	300	310	100	16.4079	1,608.02
137977	300	310	150	7.2343	504.19
137978	300	400	100	8.3765	670.28
137979	300	400	150	1.3541	63.50
137980	300	500	100	5.0528	450.66
137981	300	500	150	0.7627	25.73
137982	300	600	100	3.8582	216.00
137983	300	600	150	0.5551	19.92
137984	300	700	100	3.3627	256.55
137985	300	700	150	0.4524	12.96
137986	300	800	100	3.072	192.74
137987	300	800	150	0.415	9.44
137988	300	900	100	2.8812	176.72
137989	300	900	150	0.3813	9.92
137990	300	1000	100	2.8148	142.60
137991	300	1000	150	0.373	7.99
137992	300	1100	100	2.782	199.31
137993	300	1100	150	0.3586	8.74
137994	300	3000	100	3.4017	166.17
137995	300	3000	150	0.6846	13.54
137996	310	300	100	12.5539	1,226.38
137997	310	300	150	12.5171	1,039.81
137998	400	300	100	7.083	727.41
137999	400	300	150	6.612	617.80
138000	400	410	100	2.4927	424.77
138001	400	410	250	1.5572	149.11
138002	400	500	100	0.8395	101.91
138003	400	500	250	0.3213	20.90
138004	400	600	100	0.4286	33.64
138005	400	600	250	0.1741	7.55
138006	400	700	100	0.2993	21.09
138007	400	700	250	0.1221	3.35
138008	400	800	100	0.2394	17.20
138009	400	800	250	0.0962	2.70
138010	400	900	100	0.2068	9.01
138011	400	900	250	0.0828	1.71
138012	400	1000	100	0.1922	11.87
138013	400	1000	250	0.0778	1.88
138014	400	1100	100	0.1807	11.39
138015	400	1100	250	0.0734	1.89
138016	400	3000	100	0.2638	7.54
138017	400	3000	250	0.1172	2.99
138018	410	400	100	2.8865	590.41
138019	410	400	250	2.5961	287.14
138020	500	300	100	4.5177	442.60
138021	500	300	150	4.3233	473.54
138022	500	400	100	1.8559	387.57
138023	500	400	250	1.5974	160.59
138024	500	510	100	0.5661	145.06
138025	500	510	350	0.4233	39.88

Table A.3: Monte Carlo sample used for the SUSY signal with the used cross section*filter efficiencies taken from [29] and the expected number of events after all cut weighted to an integrated luminosity of 2.05 fb^{-1}

run	m_{gluino}	m_{squark}	m_{lsp}	cross section * filter eff. []	# after last cut
138026	500	600	100	0.1617	16.78
138027	500	600	350	0.0909	6.07
138028	500	700	100	0.0821	5.29
138029	500	700	350	0.0493	2.01
138030	500	800	100	0.0576	3.10
138031	500	800	350	0.0339	0.91
138032	500	900	100	0.0439	1.97
138033	500	900	350	0.0255	0.96
138034	500	1000	100	0.0385	1.40
138035	500	1000	350	0.022	0.87
138036	500	1100	100	0.0355	1.53
138037	500	1100	350	0.0193	0.39
138038	500	3000	100	0.0541	1.55
138039	500	3000	350	0.0274	0.52
138040	510	500	100	0.8031	191.29
138041	510	500	350	0.7069	62.52
138042	600	300	100	3.545	372.40
138043	600	300	150	3.316	324.46
138044	600	400	100	1.3108	267.59
138045	600	400	250	1.1151	96.31
138046	600	500	100	0.5466	131.11
138047	600	500	350	0.9332	94.58
138048	600	610	100	0.1688	38.53
138049	600	610	450	0.143	13.00
138050	600	700	100	0.0486	5.03
138051	600	700	450	0.0309	2.00
138052	600	800	100	0.0251	1.70
138053	600	800	450	0.0165	0.74
138054	600	900	100	0.0326	1.18
138055	600	900	450	0.0109	0.38
138056	600	1000	100	0.0133	0.54
138057	600	1000	450	0.0083	0.31
138058	600	1100	100	0.0111	0.40
138059	600	1100	450	0.0068	0.18
138060	600	3000	100	0.0205	0.33
138061	600	3000	450	0.0078	0.16
138062	610	600	100	0.2459	64.06
138063	610	600	450	0.2207	24.38
138064	700	300	100	2.9964	270.84
138065	700	300	150	2.8107	270.97
138066	700	400	100	1.0068	205.14
138067	700	400	250	0.845	80.67
138068	700	500	100	0.4031	102.68
138069	700	500	350	0.6528	74.96
138070	700	600	100	0.1822	47.59
138071	700	600	450	0.1662	17.66
138072	700	710	100	0.0589	12.72
138073	700	710	550	0.0525	5.81
138074	700	800	100	0.0177	1.91
138075	700	800	550	0.0113	0.87

Table A.4: Monte Carlo sample used for the SUSY signal with the used cross section*filter efficiencies taken from [29] and the expected number of events after all cut weighted to an integrated luminosity of 2.05 fb^{-1}

run	m_{gluino}	m_{squark}	m_{lsp}	cross section * filter eff. []	# after last cut
138076	700	900	100	0.0092	0.61
138077	700	900	550	0.0061	0.38
138078	700	1000	100	0.0064	0.27
138079	700	1000	550	0.0038	0.15
138080	700	1100	100	0.0049	0.14
138081	700	1100	550	0.003	0.09
138082	700	3000	100	0.0083	0.15
138083	700	3000	550	0.0025	0.08
138084	710	700	100	0.0855	20.29
138085	710	700	550	0.08	8.70
138086	800	300	100	2.6438	305.95
138087	800	300	150	2.4623	204.08
138088	800	400	100	0.8331	172.61
138089	800	400	250	0.7167	74.81
138090	800	500	100	0.3211	81.11
138091	800	500	350	0.518	60.31
138092	800	600	100	0.1365	35.49
138093	800	600	450	0.126	15.13
138094	800	700	100	0.0655	17.12
138095	800	700	550	0.0631	7.39
138096	800	810	100	0.0218	6.19
138097	800	810	650	0.0216	2.15
138098	800	900	100	0.0072	0.89
138099	800	900	650	0.0044	0.32
138100	800	1000	100	0.0038	0.20
138101	800	1000	650	0.0023	0.14
138102	800	1100	100	0.0026	0.09
138103	800	1100	650	0.0015	0.08
138104	800	3000	100	0.0034	0.04
138105	800	3000	650	0.0008	0.01
138106	810	800	100	0.0312	8.32
138107	810	800	650	0.0319	3.27
138108	900	300	100	2.4265	269.88
138109	900	300	150	2.2325	196.64
138110	900	400	100	0.7218	144.69
138111	900	400	250	0.6254	60.92
138112	900	500	100	0.2649	66.37
138113	900	500	350	0.4167	49.27
138114	900	600	100	0.1129	35.85
138115	900	600	450	0.102	11.89
138116	900	700	100	0.0518	14.88
138117	900	700	550	0.0488	5.76
138118	900	800	100	0.0246	7.43
138119	900	800	650	0.0253	2.83
138120	900	910	100	0.0089	2.43
138121	900	910	750	0.0093	1.18
138122	900	1000	100	0.003	0.38
138123	900	1000	750	0.0018	0.15
138124	900	1100	100	0.0016	0.10
138125	900	1100	750	0.001	0.05
138126	900	3000	100	0.0013	0.03

Table A.5: Monte Carlo sample used for the SUSY signal with the used cross section*filter efficiencies taken from [29] and the expected number of events after all cut weighted to an integrated luminosity of 2.05 fb^{-1}

run	m_{gluino}	m_{squark}	m_{lsp}	cross section * filter eff. []	# after last cut
138127	900	3000	750	0.0003	0.01
138128	910	900	100	0.0118	3.41
138129	910	900	750	0.0131	1.39
138130	1000	300	100	2.1994	201.85
138131	1000	300	150	2.0862	202.25
138132	1000	400	100	0.6482	152.89
138133	1000	400	250	0.5677	59.48
138134	1000	500	100	0.2322	67.20
138135	1000	500	350	0.3402	36.26
138136	1000	600	100	0.0938	24.85
138137	1000	600	450	0.0875	10.96
138138	1000	700	100	0.0422	-
138139	1000	700	550	0.0407	5.80
138140	1000	800	100	0.0199	6.34
138141	1000	800	650	0.0199	2.36
138142	1000	900	100	0.01	2.99
138143	1000	900	750	0.0104	1.27
138144	1000	1010	100	0.0037	0.89
138145	1000	1010	850	0.0039	0.52
138146	1000	1100	100	0.0013	0.14
138147	1000	1100	850	0.0008	-
138148	1000	3000	100	0.0005	0.01
138149	1000	3000	850	0.0001	0.00
138150	1010	1000	100	0.0047	1.28
138151	1010	1000	850	0.0056	0.66
138152	1100	300	100	2.089	177.85
138153	1100	300	150	1.9202	134.71
138154	1100	400	100	0.5968	122.77
138155	1100	400	250	0.5386	67.51
138156	1100	500	100	0.2073	45.21
138157	1100	500	350	0.2944	35.41
138158	1100	600	100	0.0819	21.90
138159	1100	600	450	0.074	7.78
138160	1100	700	100	0.0361	10.49
138161	1100	700	550	0.0356	4.46
138162	1100	800	100	0.017	4.85
138163	1100	800	650	0.017	1.92
138164	1100	900	100	0.008	2.48
138165	1100	900	750	0.0086	0.96
138166	1100	1000	100	0.0038	1.14
138167	1100	1000	850	0.0047	0.58
138168	1100	1110	100	0.0016	0.40
138169	1100	1110	950	0.0018	0.18
138170	1100	3000	100	0.0002	0.00
138171	1100	3000	950	0	0.00
138172	1110	1100	100	0.0019	0.55
138173	1110	1100	950	0.0025	0.25
138174	3000	300	100	1.7324	201.03
138175	3000	300	150	1.5724	153.61
138176	3000	400	100	0.3541	67.38

Table A.6: Monte Carlo sample used for the SUSY signal with the used cross section*filter efficiencies taken from [29] and the expected number of events after all cut weighted to an integrated luminosity of 2.05 fb^{-1}

run	m_{gluino}	m_{squark}	m_{lsp}	cross section * filter eff. []	# after last cut
138177	3000	400	250	0.3066	32.30
138178	3000	500	100	0.0924	25.35
138179	3000	500	350	0.1089	11.64
138180	3000	600	100	0.0306	8.04
138181	3000	600	450	0.0281	3.39
138182	3000	700	100	0.0119	3.43
138183	3000	700	550	0.0114	1.36
138184	3000	800	100	0.0049	1.58
138185	3000	800	650	0.0051	0.63
138186	3000	900	100	0.0021	0.58
138187	3000	900	750	0.0024	0.25
138188	3000	1000	100	0.0009	0.28
138189	3000	1000	850	0.0012	0.15
138190	3000	1100	100	0.0004	0.11
138191	3000	1100	950	0.0006	0.08

Table A.7

Appendix B

More distributions

B.1 WZ Herwig vs. Alpgen

There are two different Monte Carlo generator for the WZ process by Herwig and Alpgen. Figure B.1 shows the invariant mass distribution of the corresponding Z using truth information. The Alpgen distribution of the Z peak shows a clear cut right above the Z mass, where it has a strong peak. The Herwig distribution has a much wider width and a smaller peak. Figure B.2 shows the same distribution for reconstructed leptons at the leptonp_T cut stage using an ossf pair with the highest p_T. The structure of the hard cut in the invariant mass and the higher peak for Alpgen are still visible. Since the cut-and-count analysis uses a Z veto to reduce the WZ background, the Z peak has to modeled correctly to avoid discrepancies for MC and data in either control or signal regions. Therefore WZ Herwig is taken for the analysis instead of Alpgen, as its invariant mass distribution looks more reasonable.

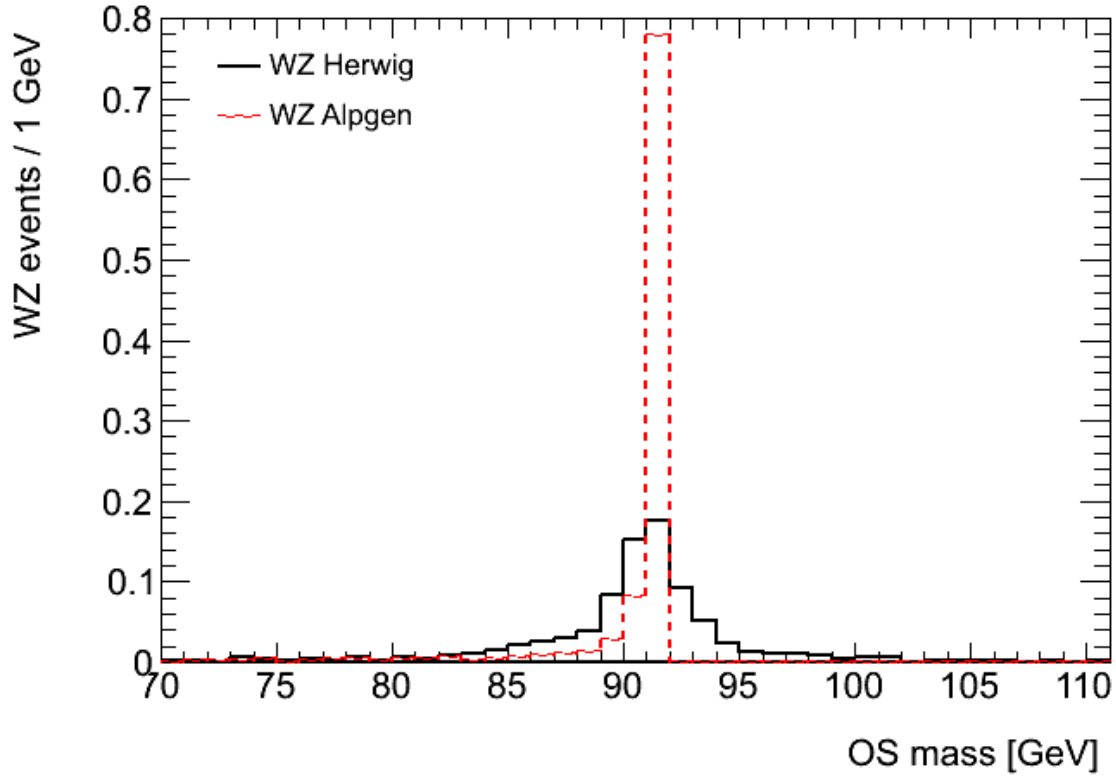

Figure B.1: Invariant mass distribution on truth level of the Z in a WZ decay for Alpgen and Herwig. Taken from [42].

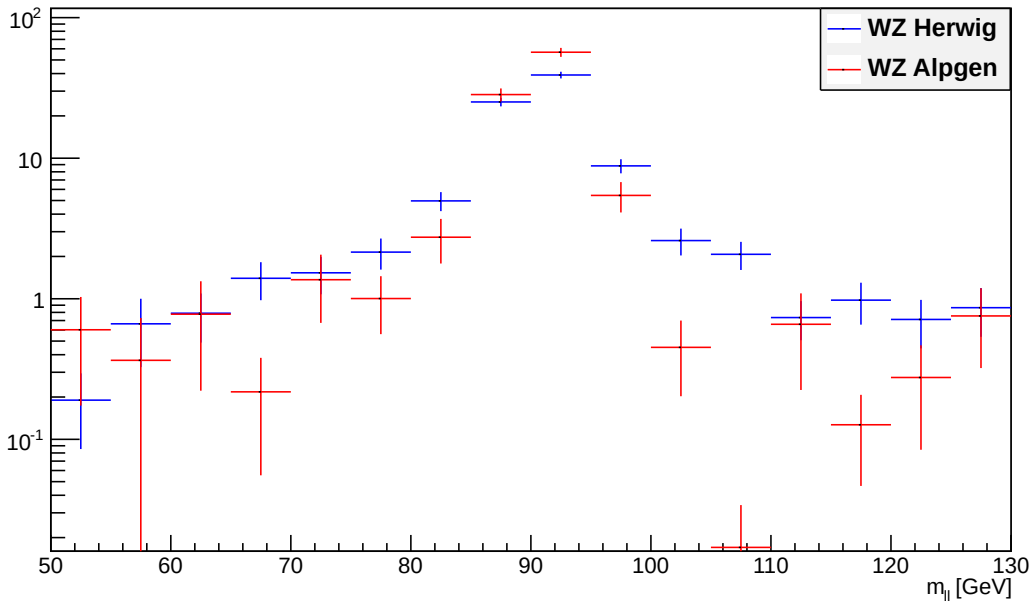

Figure B.2: Invariant mass distribution on reconstruction level for Alpgen and Herwig requiring three leptons.

B.2 Delta R between nonisolated leptons and jets

The trilepton events in the $t\bar{t}$ MC sample are investigated a little bit closer. After requiring the leptonp_T, the secondary lepton is searched for with the information of the MCTruthClassifier. If a lepton doesn't overlap with a signal lepton (according to the classifier) within a ΔR of 0.4, it is considered as nonisolated. With the further help of truth information, the ΔR to the closest reconstructed jet, to the closest true b-quark and this b-quark to the closest true jet is shown for electrons and muons in figures B.3 and B.4. It is clearly visible, that there is a large distance in ΔR between the nonisolated leptons and the closest reconstructed jet. Nevertheless, they overlap very well with a b-quark and a true jet. Hence, the b-jet from which the nonisolated lepton originated, has to be lost in the reconstruction. For electrons this can be the case because of the electron-jet overlap removal. For muons, this cannot be the case, because the jet-muon overlap removal was not applied. Because of this, the b-tagging algorithm in the fake rate measurement is applied before any overlap removal was done.

B.3 Optimisation plots for the cut-and-count analysis

The $\frac{s}{\sqrt{b}}$ optimisation of some variables for the cut-and-count analysis is shown in figure B.5. The plots contain the optimisation for all SUSY signal points and the integral of each distribution is scaled to 1.

B.4 Figures comparing distributions of data and MC/Fake

The comparison between data + Monte Carlo and data + MatrixMethod/Monte Carlo has only be done for the cutflow and the signal region so far. To show, that the matrix methods does not only work for

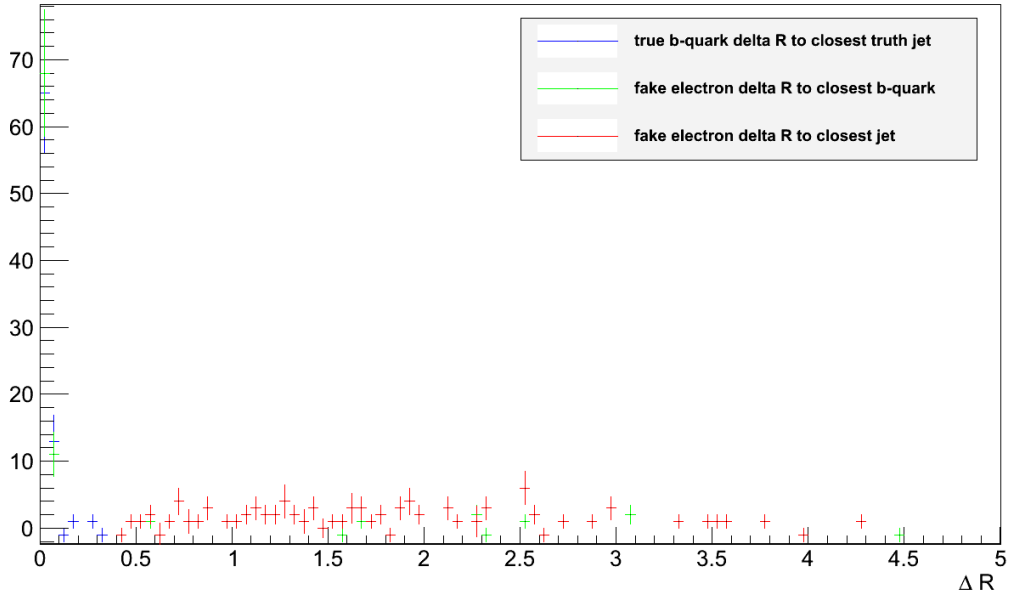

Figure B.3: ΔR between nonisolated electrons and the closest reconstructed jet, true b-quark and true jet.

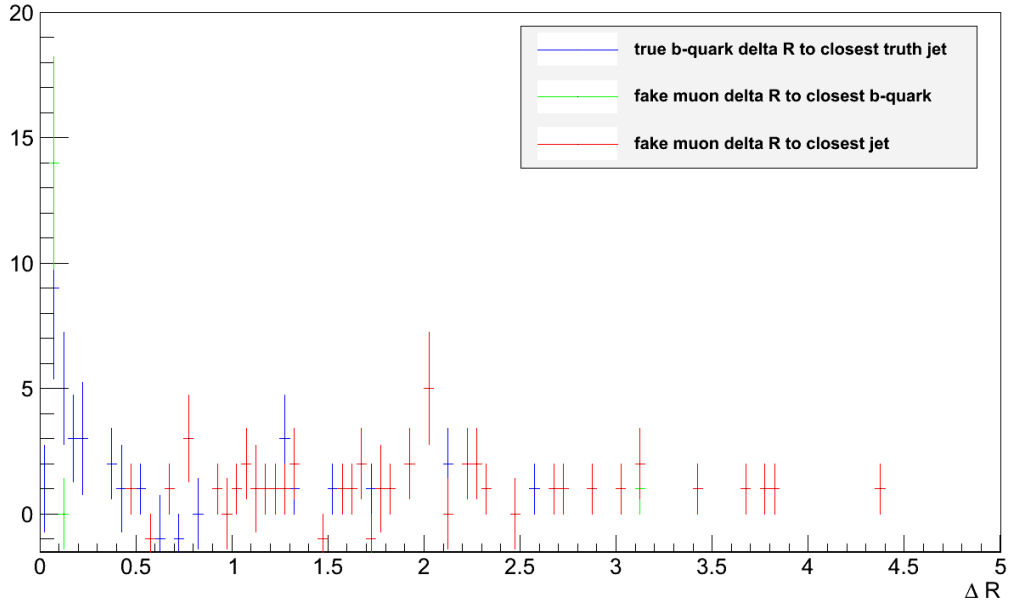

Figure B.4: ΔR between nonisolated muons and the closest reconstructed jet, true b-quark and true jet.

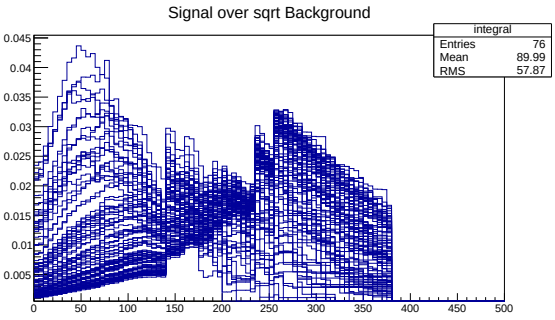

(a) E_T^{miss} , light lsp mode

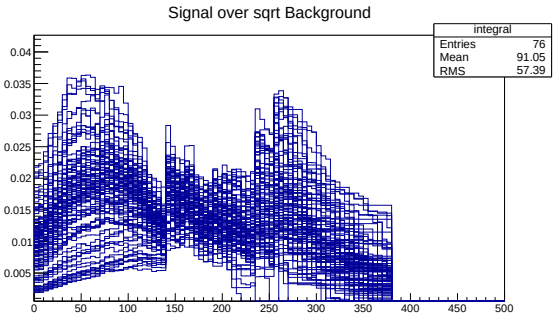

(b) E_T^{miss} , compressed mode

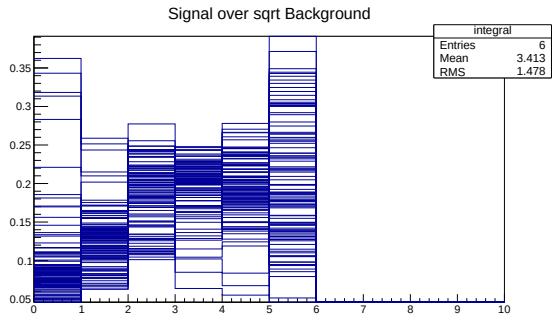

(c) # of jets, light lsp mode

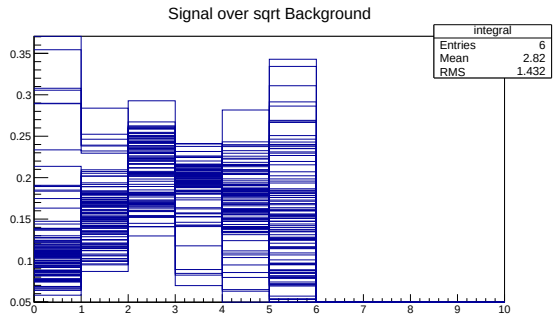

(d) # of jets, compressed mode

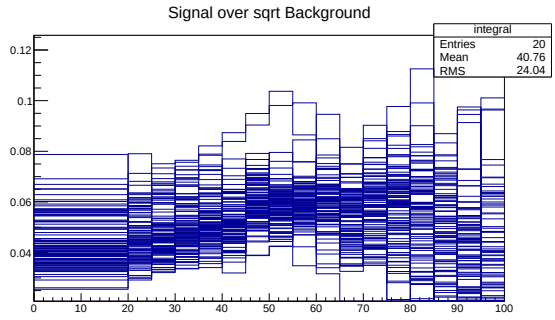

(e) first electron p_T, light lsp mode

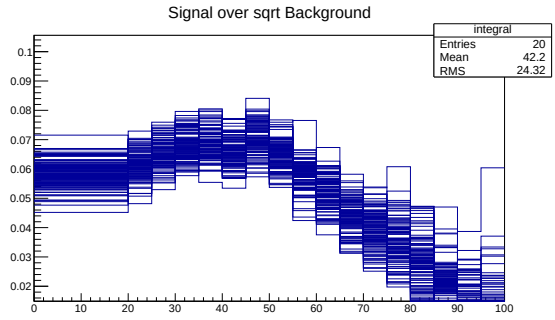

(f) first electron p_T, compressed mode

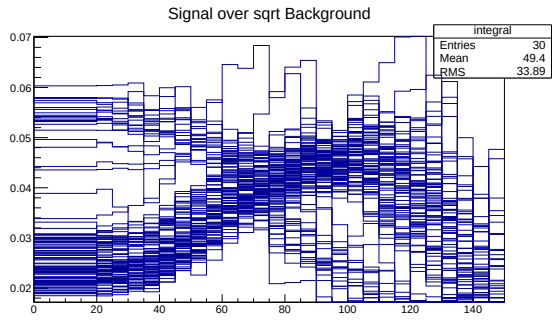

(g) first muon p_T, light lsp mode

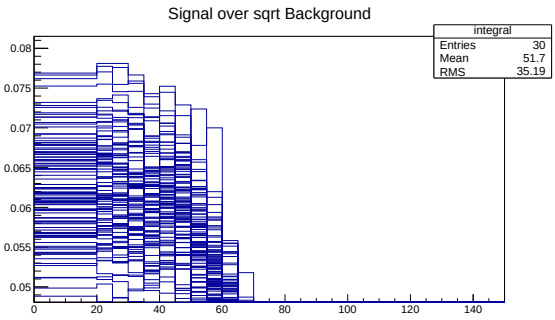

(h) first muon p_T, compressed mode

Figure B.5: Optimisation plots.

the signal, but also in control regions, the number of events for control regions defined by the number of jets, the E_T^{miss} and if an events lies in-/outside the Z cut window is compared to the only MC case and shown in the following figures. On the x axis, the number of leptons is shown. Only the three lepton bin is of course filled, because every event passed the leptonp_T cut. It is just used to get the number of events for each control region. After that, a comparison of some distributions between Monte Carlo and data at the leptonp_T cut stage is shown.

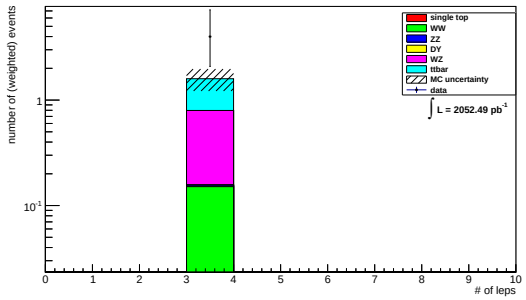

(a) MC, ≥ 2 jets, $E_T^{\text{miss}} > 50$ GeV, out Z (signal region)

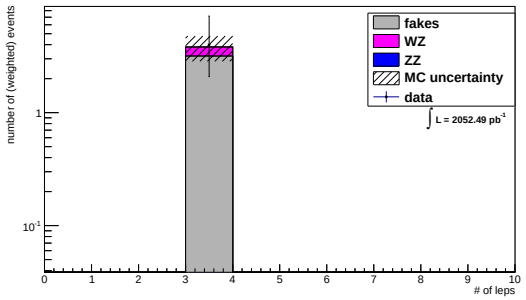

(b) fakes, ≥ 2 jets, $E_T^{\text{miss}} > 50$ GeV, out Z (signal region)

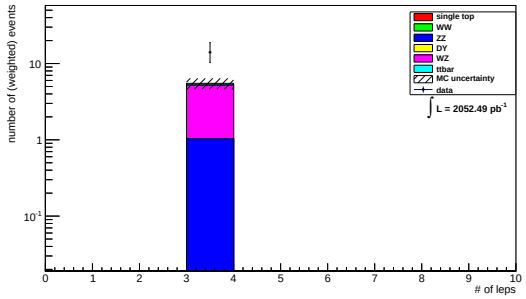

(c) MC, ≥ 2 jets, $E_T^{\text{miss}} > 50$ GeV, in Z

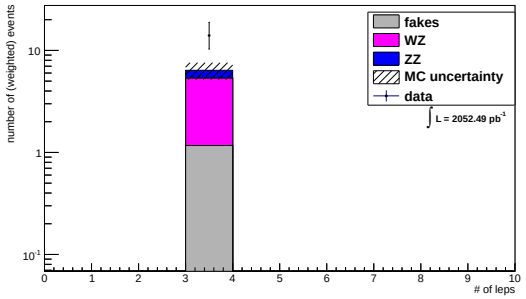

(d) fakes, ≥ 2 jets, $E_T^{\text{miss}} > 50$ GeV, in Z

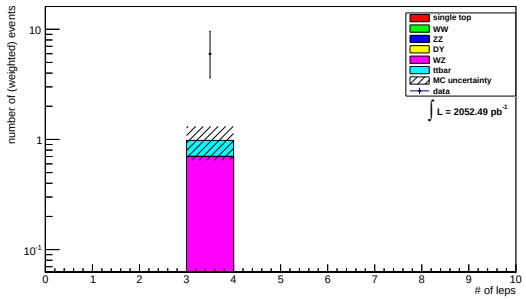

(e) MC, ≥ 2 jets, $E_T^{\text{miss}} < 50$ GeV, out Z

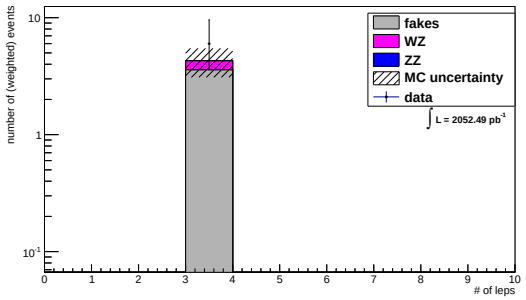

(f) fakes, ≥ 2 jets, $E_T^{\text{miss}} < 50$ GeV, out Z

Figure B.6: Comparison of the event yield by the matrix method + Monte Carlo and only Monte Carlo for different regions is shown.

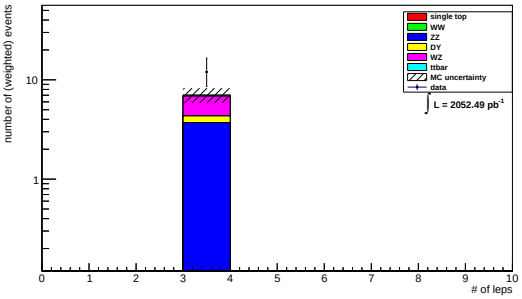

(a) MC, ≥ 2 jets, $E_T^{\text{miss}} < 50$ GeV, in Z

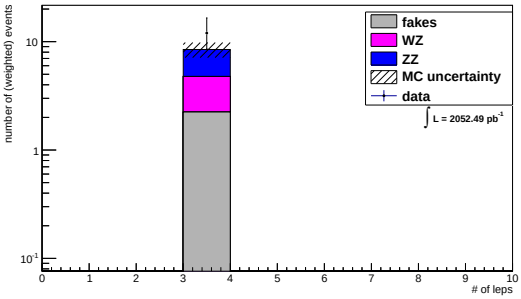

(b) fakes, ≥ 2 jets, $E_T^{\text{miss}} < 50$ GeV, in Z

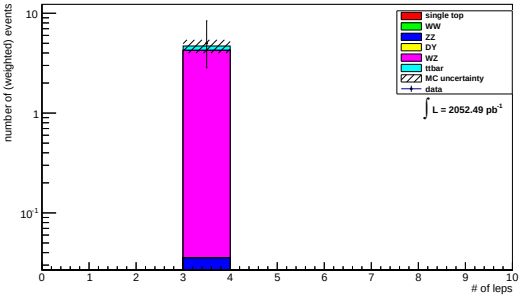

(c) MC, < 2 jets, $E_T^{\text{miss}} > 50$ GeV, out Z

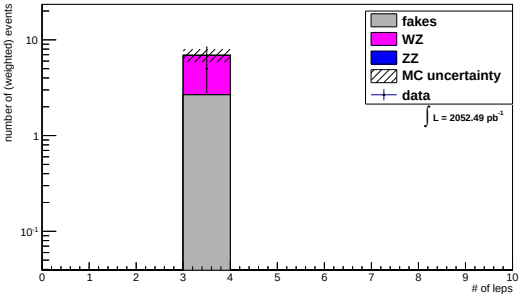

(d) fakes, < 2 jets, $E_T^{\text{miss}} > 50$ GeV, out Z

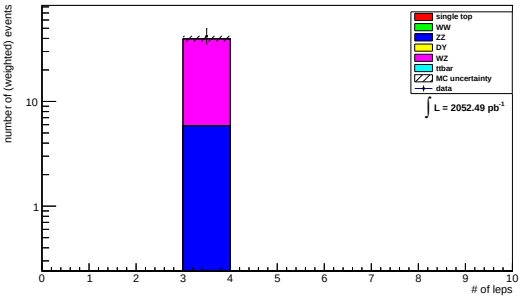

(e) MC, < 2 jets, $E_T^{\text{miss}} > 50$ GeV, in Z

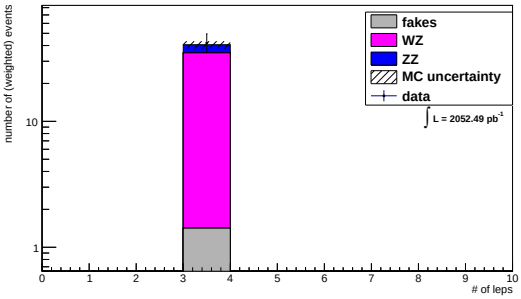

(f) fakes, < 2 jets, $E_T^{\text{miss}} > 50$ GeV, in Z

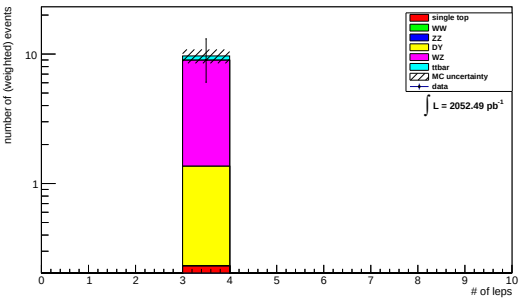

(g) MC, < 2 jets, $E_T^{\text{miss}} < 50$ GeV, out Z

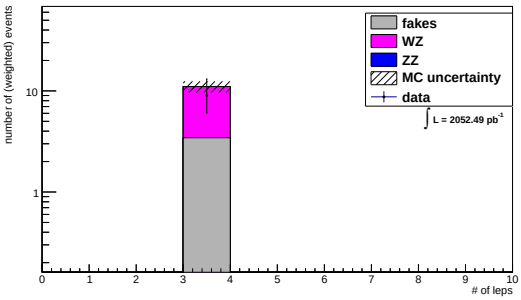

(h) fakes, < 2 jets, $E_T^{\text{miss}} < 50$ GeV, out Z

Figure B.7: Comparison of the event yield by the matrix method + Monte Carlo and only Monte Carlo for different regions is shown.

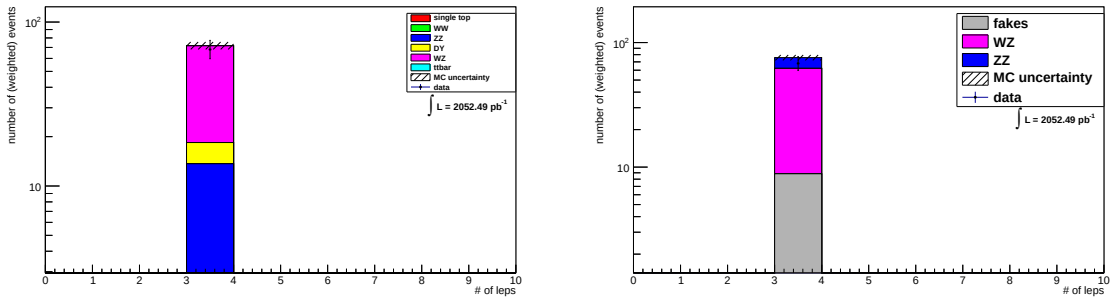

(a) MC, < 2 jets, $E_T^{\text{miss}} < 50$ GeV, in Z

(b) fakes, < 2 jets, $E_T^{\text{miss}} < 50$ GeV, in Z

Figure B.8: Comparison of the event yield by the matrix method + Monte Carlo and only Monte Carlo for different regions is shown.

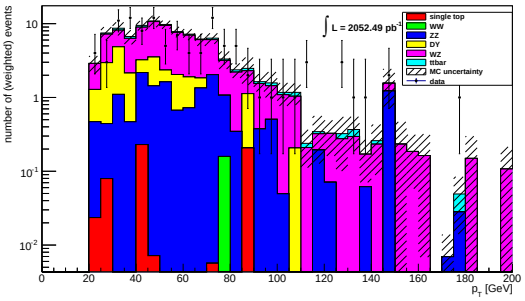

(a) First electron p_T

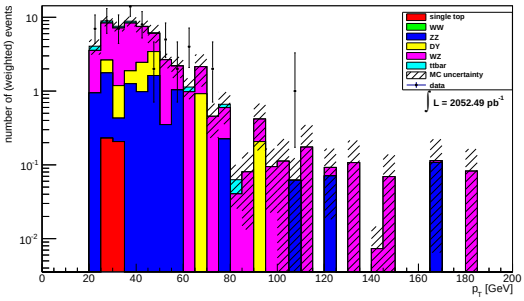

(b) Second electron p_T

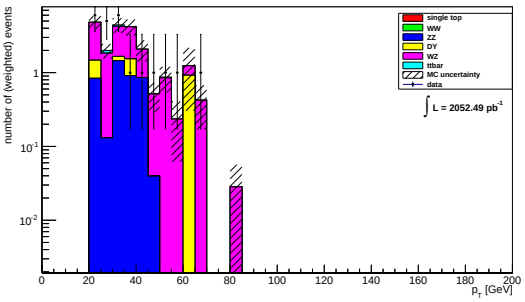

(c) Third electron p_T

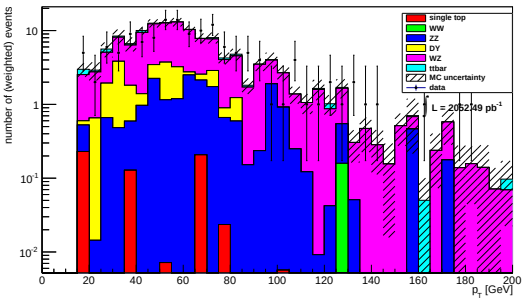

(d) First muon p_T

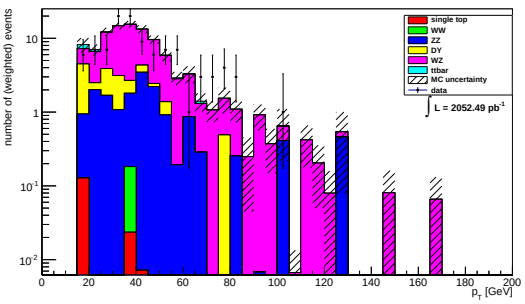

(e) Second muon p_T

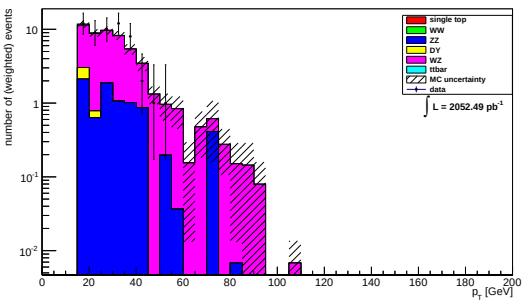

(f) Third muon p_T

Figure B.9: Comparison of data and MC background at the leptonp_T cut stage for an integrated luminosity of 2.05 fb^{-1}.

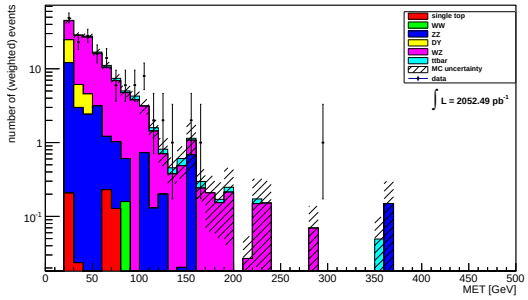

(a) E_T^{miss}

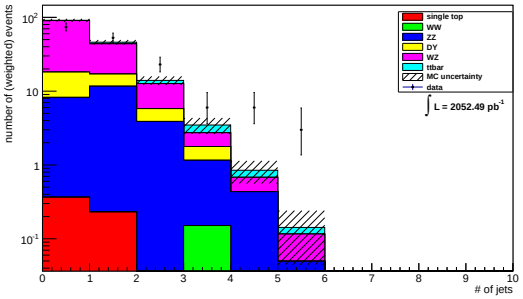

(b) Number of jets

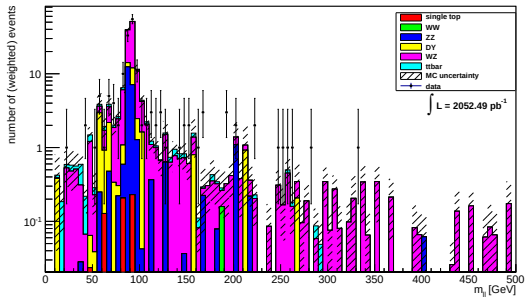

(c) Invariant mass of ossf pair

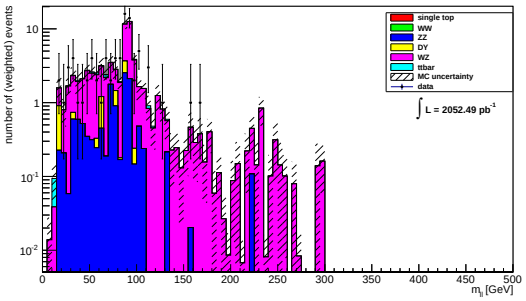

(d) Invariant mass, if there's a second ossf pair

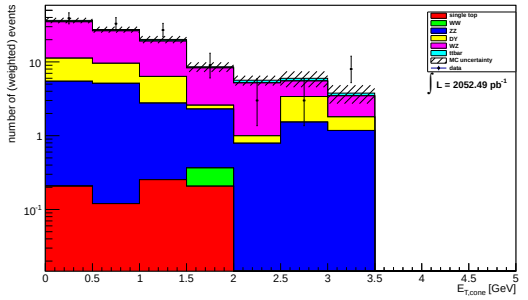

(e) Electron E_T^{cone}

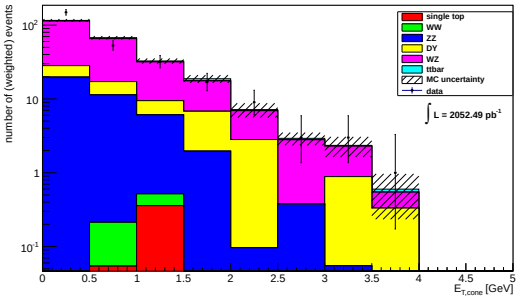

(f) Muon E_T^{cone}

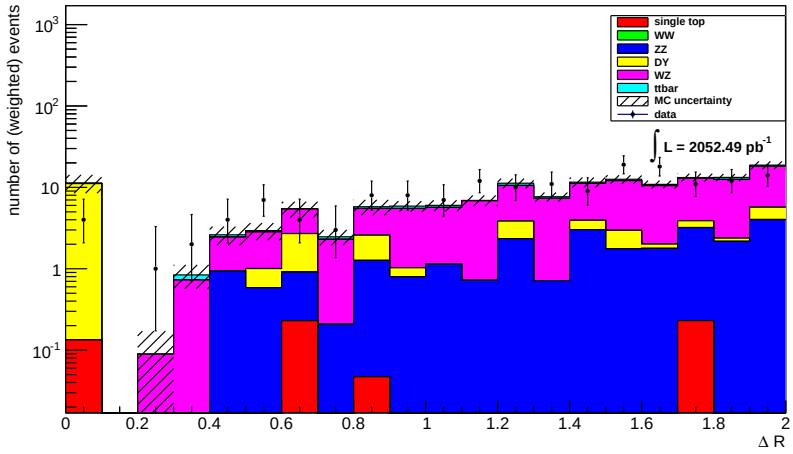

(g) ΔR of all lepton pairs

Figure B.10: Comparison of data and MC background at the leptonp_T cut stage for an integrated luminosity of 2.05 fb^{-1}.

Bibliography

[1] Sheldon Glashow. 'Partial Symmetries of Weak Interactions'. In: *Nucl. Phys.* 22 (1961), p. 579; Abdus Salam. 'Weak and Electromagnetic Interactions'. In: *Elementary particle theory. Relativistic groups and analyticity. Proceedings of the Eighth Nobel Symposium*. Ed. by Nils Svartholm. Stockholm: Almquist & Wiksell, 19th–25th May 1968, p. 367; Steven Weinberg. 'A Model of Leptons'. In: *Phys. Rev. Lett.* 19 (1967), p. 1264.

[2] UA2 collaboration. 'Evidence for $Z^0 \rightarrow e^+e^-$ at the CERN $\bar{p}p$ collider'. In: *Physics Letters* 129.1-2 (1983), pp. 130–140.

[3] Carlo Rubbia. 'Experimental observation of the intermediate vector bosons W^+, W^- and Z^0'. In: *Rev. Mod. Phys.* 57 (1985), pp. 699–722.

[4] CDF Collaboration. 'Observation of Top Quark Production in $\bar{p}p$ Collisions with the Collider Detector at Fermilab'. In: *Physical Review Letters* 74.14 (1995), pp. 2626–2631.

[5] D0 Collaboration. 'Search for High Mass Top Quark Production in $p\bar{p}$ Collisions at $\sqrt{s}$ = 1.8 TeV'. In: *Physical Review Letters* 74.13 (1995), pp. 2422–2426.

[6] DONUT Collaboration. *Observation of Tau Neutrino Interactions*. arXiv:hep-ex/0012035. 2000.

[7] CDF Collaboration. 'Search for Supersymmetry in $p\bar{p}$ Collisions at $\sqrt{s}$ = 1.96 TeV using the Trilepton Signature of Chargino-Neutralino Production'. In: *Physical Review Letters* 101 (2008).

[8] D0 Collaboration. 'Search for associated production of charginos and neutralinos in the trilepton final state using 2.3 fb-1 of data'. In: *Physics Letters B* 680.1 (2009), pp. 34–43.

[9] CERN. *LHC Design Report*. CERN-2004-003-V-1. 2004.

[10] LHC webpage. `http://lhc.web.cern.ch/lhc/`.

[11] ATLAS webpage. *http://atlas.web.cern.ch/Atlas/Collaboration/*.

[12] The ATLAS Collaboration. 'Expected Performance of the ATLAS Experiment'. In: *CERN-OPEN-2008-020* (2008).

[13] ATLAS Collaboration. 'The ATLAS Experiment at the CERN Large Hadron Collider'. In: *JINST* 3.S08003 (2008).

[14] Wikipedia. `http://en.wikipedia.org/wiki/Standard_Model`.

[15] Paul Langacker. *The Standard Model and Beyond*. Series in High Energy Physics, Cosmology and Gravitation. CRC Press, 2010.

[16] Stephen P. Martin. *A Supersymmetry Primer*. arXiv:hep-ph/9709356. 2008.

[17] ATLAS SUSY group. `https://zmarshal.web.cern.ch/zmarshal/models`.

[18] Oleg Brandt, Alan Barr and Pawel Bruckman de Rentstrom. *Search strategies for Supersymmetry in tri-lepton final states with the ATLAS detector at the Large Hadron Collider*. 2008.

[19] ATLAS SUSY Group. *Mis-identified lepton backgrounds in top quark pair production studies for EPS 2011 analyses*. ATL-COM-PHYS-2011-1268. 2011.

[20] ATLAS Top Monte Carlo Page. https://twiki.cern.ch/twiki/bin/viewauth/AtlasProtected/TopMC10for2011Data.

[21] ATLAS Top Reconstruction Group. https://twiki.cern.ch/twiki/bin/viewauth/AtlasProtected/TopCommonObjects2011rel16.

[22] ATLAS Egamma Group. https://twiki.cern.ch/twiki/bin/viewauth/AtlasProtected/IsEMIdentification.

[23] Nathalie Besson. https://twiki.cern.ch/twiki/pub/AtlasProtected/D3PDContent/D3PDNtuple.pdf.

[24] ATLAS Top Reconstruction Group. https://twiki.cern.ch/twiki/bin/viewauth/AtlasProtected/TopCommonScales.

[25] ATLAS MuidMuonCollection. https://twiki.cern.ch/twiki/bin/viewauth/AtlasProtected/MuidMuonCollection.

[26] ATLAS Top Reconstruction Group. https://twiki.cern.ch/twiki/bin/viewauth/AtlasProtected/TopJetLiaison.

[27] ATLAS Collaboration. https://twiki.cern.ch/twiki/bin/viewauth/AtlasProtected/PileupReweighting.

[28] ATLAS collaboration. *MCTruthClassifier*. https://twiki.cern.ch/twiki/bin/viewauth/AtlasProtected/MCTruthClassifier.

[29] ATLAS SUSY MC production group. https://twiki.cern.ch/twiki/bin/viewauth/AtlasProtected/PhenoGrid2.

[30] ATLAS SUSY Group. *A search for SUSY-like events in same-sign dilepton and interpretation using a simplified model*. ATL-COM-PHYS-2011-294. 2011.

[31] ATLAS Top Reconstruction Group. https://twiki.cern.ch/twiki/bin/viewauth/AtlasProtected/TopGRLs.

[32] ATLAS Data Quality Summary. https://atlas.web.cern.ch/Atlas/GROUPS/DATAPREPARATION/DQSUMMARY/.

[33] ATLAS Top Reconstruction Group. https://twiki.cern.ch/twiki/bin/viewauth/AtlasProtected/TopSystematicUncertainties2011rel16.

[34] ATLAS Top Reconstruction Group. https://twiki.cern.ch/twiki/bin/view/AtlasProtected/MultijetJESUncertaintyProviderTop.

[35] ATLAS Top Reconstruction Group. https://twiki.cern.ch/twiki/bin/view/AtlasProtected/TopJetReconstructionEfficiency.

[36] ATLAS Top Reconstruction Group. https://twiki.cern.ch/twiki/bin/viewauth/AtlasProtected/TopETmissLiaison_EPS.

[37] The ATLAS Collaboration. *Mis-identified lepton backgrounds in top quark pair production studies for EPS 2011 analyses*. ATL-COM-PHYS-2011-768. 2011.

[38] ATLAS Top Reconstruction Group. https://twiki.cern.ch/twiki/bin/viewauth/AtlasProtected/Analysis16.

[39] A. L. Read. 'Presentation of search reults: the CL(s) technique'. In: *J. Phys.* G28 (2002), pp. 2693–2704.

[40] Klaus Desch. *Statistical methods of data analysis*. SS10, University of Bonn.

[41] Jerzy Neyman and Egon Pearson. *On the Problem of the most Efficient Tests of Statistical Hypotheses*. Philosophical Transactions of the Royal Society of London. Series A, Containing Papers of a Mathematical or Physical Character. 1932.

[42] Email correspondence between Louise Skinnari and Tatevik Abajyan.

Acknowledgements

Ich danke Prof. Wermes, dass ich meine Masterarbeit in seiner Arbeitsgruppe schreiben durfte. Für die Betreuung meiner Arbeit bedanke ich mich bei Markus Cristinziani. Aus der Topgruppe danke ich außerdem besonders Tatevik und Kirika, die mir bei Problemen jederzeit zur Seite standen und bei den Lösungen sehr geholfen haben. Meinen Eltern danke ich insbesondere für die Finanzierung meines Studiums und dass sie mich in Krisenzeiten immer aufgefangen haben. Allgemein möchte ich meiner Familie danken, die mich immer unterstützt hat und meine Launen ertragen musste, wenn etwas nicht so lief, wie ich mir das vorgestellt habe.